DOCTOR OF PHILOSOPHY

Accelerated fibre microendoscopy techniques for in-vivo applications

Turtaev, Sergey

Award date:
2018

UNIVERSITY OF DUNDEE

DOCTORAL THESIS

Accelerated fibre microendoscopy techniques for in-vivo applications

Author:
Sergey TURTAEV

Supervisor:
Prof. Cornelis J.WEIJER
Prof. Tomáš ČIŽMÁR

A thesis submitted in fulfilment of the requirements for the degree of Doctor of Philosophy

in the

School of Life Sciences

November, 2018

Contents

List of Figures

List of Abbreviations

SLM	Spatial Light Modulator
DMD	Digital Micromirror Device
LC-SLM	Liquid-Crystal based Spatial Light Modulator
MEMS	MicroElectroMechanical Systems
GPU	Graphics Processing Unit
CCD	Charge-Coupled Device based Camera
TM	Transformation Matrix

List of Publication

Peer-reviewed articles

1. ***Turtaev, S.***, Leite, I. T., Altwegg-Boussac, T., Pakan, J. M., Rochefort, N. L., & Čižmár, T. "High-fidelity multimode fibre-based endoscopy for deep-brain in vivo imaging." arXiv preprint arXiv:1806.01654, **2018**.

2. Flaes, D., Boonzajer, E., Stopka J., ***S. Turtaev***, de Boer, J. F., Tyc, T., and Čižmár T. Robustness of Light-Transport Processes to Bending Deformations in Graded-Index Multimode Waveguides. *Physical Review Letters* **120**(23), 233901 **2018**.

3. Leite, I. T., ***Turtaev, S.***, Jiang, X., Šiler, M., Cuschieri, A., Russell, P. S. J., and Čižmár, T. Three-dimensional holographic optical manipulation through a high-numerical-aperture soft-glass multimode fibre. *Nature Photonics* **12**(1), 33 **2018**.

4. ***Turtaev, S.***, Leite, I. T., Mitchell, K. J., Padgett, M. J., Phillips, D. B., and Čižmár, T. Comparison of nematic liquid-crystal and DMD based spatial light modulation in complex photonics. *Optics Express* **25**(24), 29874-29884 **2017**.

5. Mitchell, K. J., ***Turtaev, S.***, Padgett, M. J., Čižmár, T., and Phillips, D. B. High-speed spatial control of the intensity, phase and polarisation of vector beams using a digital micro-mirror device. *Optics Express* **24**(25) 29269-29282 **2016**.

6. ***Turtaev, S.***, Leite, I. T., and Čižmár, T. Multimode fibres for micro-endoscopy. *Optofluidics, Microfluidics and Nanofluidics* **2**(1), 31-35 **2015**.

Publications in conference proceedings

1. Stellinga, D., Phillips, D. B., Edgar, M., ***Turtaev, S.***, Čižmár, T., and Padgett, M. J. Imaging Beyond a Multimode Fibre with Time of Flight Depth Information. *In CLEO: Science and Innovations* (Optical Society of America) **STh3K-3 2018**.

2. Flaes, D. E. B., Stopka, J., ***Turtaev, S.***, Witte, S., de Boer, J., Tyc, T., and Čižmár, T. Predicting the transmission matrix of graded index media. *In Adaptive Optics and Wavefront Control for Biological Systems IV* (International Society for Optics and Photonics) **10502**, 105021C **2018**.

3. Mitchell, K. J., ***Turtaev, S.***, Padgett, M.J., Čižmár, T., and Phillips, D.B. High-speed polarisation shaping of arbitrary vector beams using a digital micro-mirror device. *In CLEO: Science and Innovations*(Optical Society of America), **STu4O-2 2017**.

4. ***Turtaev, S.***, Leite, I. T., and Cizmár, T. High-speed wavefront modulation in complex media. *In Adaptive Optics and Wavefront Control for Biological Systems III* (International Society for Optics and Photonics) **10073**, 1007313 **2017**.

5. ***Turtaev, S. N.***, Chernysheva, M. A., Fedorova, K. A., Gorodetsky, A. A., and Rafailov, E. U. Dark soliton generation from semiconductor optical amplifier gain medium in ring fiber configuration. *In International Conference Laser Optics (LO)* (IEEE), **R3-40 2016**.

6. Fedorova, K. A., ***Turtaev, S. N.***, Bakshaev, I. O., Livshits, D. A., and Rafailov, E. U. Tunable visible dual-wavelength SHG from a diode-pumped PPKTP waveguide. *In The European Conference on Lasers and Electro-Optics* (Optical Society of America) **CD-P-28 2015**.

Acknowledgements

I would like to thank a number of great individuals, whose support and encouragement generously contributed to the work presented in this thesis.

I am extremely indebted to Tomas Cizmar, for sharing his expertise so willingly, and for being so dedicated to his role as my supervisor. My PhD has been an amazing experience and I thank Tomas wholeheartedly, for the guidence in research and general matters, friendly, motivational attitude and extreme patience. Similar, profound gratitude goes to Kees Weijer, who has also been a truly dedicated mentor.

I would like to thank my thesis monitoring committee of Jason Swedlow and David McGloin for their supportive and encouraging attitude throughout my PhD studies.

Completing this work would have been all the more difficult were it not for the support and friendship. I would like to thank my colleague and friend Ivo Leite for struggling and helping in whatever way he could during this challenging period. Thanks for numerous last minute favours.

Others at University of Dundee to whom I am grateful are Sam Swift, Keith Wilcox, members of technical staff at School of Science and Engineering and facilitators of Systems Biology at the School of Life Sciences.

I greatly appreciate the support received through the collaborative work undertaken with Kevin Mitchel, Miles Padget, and David Phillips for their support and sharing expertise, which allowed kick-starting of the project. I am particularly appreciative to our collaborators Nathalie Rochefort, Tristan Altwegg-Boussac and Janelle Pakan for their involvement into the project, sharing their expertise in neuroscience and willing for deep understanding of our technology and overall fostering enthusiasm in joint experiments. In a similar vein, I'd like to recognize Xin Jiang and Philip Russell for designing and manufacturing of the unique optical fibres to facilitate our experiments.

I would like to thank the ITN project "PHOQUS" for providing the financial support, which allowed undertaking this research, and for the opportunity to attend conferences and meet so many interesting people. Special mention goes to Edik Rafailov from Aston University for a push to get started. I would like to thank my fellow doctoral students within PHOQUS project for their support, feedback, and friendship.

I would like to thank members of Leibniz Institute of Photonics Technologies for helping me through the last year as I tried to juggle working and completing my dissertation. In particular, I am grateful to Beatriz Silveira for diligent proofrearing and valuable comments on the manuscript.

Finally, thanks go to my family for almost unbelievable support. They are the most important people in my world and I dedicate this thesis to them.

Declaration of Authorship

I, Sergey TURTAEV, declare that this thesis titled, "Accelerated fibre microendoscopy techniques for in-vivo applications" and the work presented in it are my own. I confirm that:

- This work was done wholly or mainly while in candidature for a research degree at this University.
- Where any part of this thesis has previously been submitted for a degree or any other qualification at this University or any other institution, this has been clearly stated.
- Where I have consulted the published work of others, this is always clearly attributed.
- Where I have quoted from the work of others, the source is always given. With the exception of such quotations, this thesis is entirely my own work.
- I have acknowledged all main sources of help.
- Where the thesis is based on work done by myself jointly with others, I have made clear exactly what was done by others and what I have contributed myself.

Signed:

Date: 16/11/2018

UNIVERSITY OF DUNDEE

Abstract

School of Science & Engineering

Doctor of Philosophy

Accelerated fibre microendoscopy techniques for in-vivo applications

by Sergey TURTAEV

Progress in modern biology and particularly in neuroscience constantly relies on the development of new techniques to investigate the structural and dynamical complexity of living matter at the cellular and sub-cellular size levels. An ongoing challenge is to achieve minimally-invasive and high-resolution observations of neuronal activity in vivo inside deep brain areas. A perspective strategy is to utilise holographic control of light propagation in complex media, which allows converting a hair-thin multimode optical fibre into an ultra-narrow imaging tool. Compared to current endoscopes based on GRIN lenses or fibre bundles, this concept offers a footprint reduction exceeding an order of magnitude, together with a significant enhancement in resolution.

This thesis represents one of the first attempts to move multimode fibre based systems from imaging of static targets and fixed samples, towards dynamic and challenging environments as a living animal.

High-performance holographic methods implemented on the fastest available nowadays spatial light modulator allowed to design compact and high-speed system for raster-scan fluorescent imaging at the tip of a fibre with micron-scale resolution, dictated only by the numerical aperture of the probe and the high purity/contrast of the focal points approaching the theoretical limits. These factors made the system capable of in-vivo observations of cell bodies and processes of inhibitory neurons within deep layers of the visual cortex and hippocampus of anesthetised mice.

Future advancements will strongly rely on the development of new fibre types directly optimised for the purposes of holographic endoscopy. Utilising such custom-made fibre with significantly enhanced numerical aperture, allowed demonstration of the focusing power of the best water-immersion physiology objectives, but also extend the applicability of holographic endoscopy towards minimally-invasive implementation of optical manipulation.

The results achieved pave the way to in-vivo implementation of numerous techniques of modern microscopy including multiphoton, super-resolution and light-sheet approaches, which will build further on the performance presented here.

Chapter 1

Introduction

1.1 Penetration depth of light-based microscopy

A number of the most exciting secrets in tissue, organ and even organism functioning are encrypted at the cellular and sub-cellular levels, deep inside the living matter. Deep functional connectivity between different levels of the biological organisation very often cannot be studied outside the natural unperturbed environment. Currently untenable for modern non-invasive imaging techniques, a combination of high resolution and extended depth of penetration required, raises a significant obstacle for the studies of biological processes located in deep tissues (see Fig. 1.1).

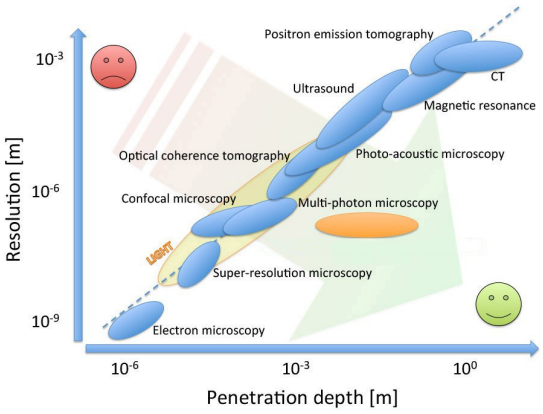

FIGURE 1.1: Trade-off between resolution and penetration depth for common methods of biomedical imaging. *Reprinted from [1]*

The optical microscopy as a key tool of modern biology to observe cellular properties struggles to penetrate deeper into the biological samples due to natural limitations. The penetration depth, as well as the axial resolution of light-based imaging systems, strongly depend on the optical properties of the sample itself. Living tissues of almost all organisms are highly scattering optical media with complex spatial variations in the refractive index [2, 3], which leads to significant aberrations in focusing through a thick sample and dramatically decreases imaging quality.

In general, the penetration depth of light-based microscopy is determined by the distance, which non-scattered (or ballistic) photons can travel in the tissue. A portion of photons remaining ballistic (B) as a function of distance along the optical axis (z) follows Lambert's law [4]:

$$B(z) = \exp^{-\mu_s z}. \tag{1.1}$$

Mean free path (MFP), defined as the reciprocal of the scattering coefficient (μ_s), describes the average distance, that a photon travels between two consecutive scattering events. Having values about 100 μm for biological tissues, MFP limits the penetration depth of basic imaging approaches (i.e. epi-fluorescent), although, in order to preserve diffraction-limited resolution and low noise operation caused by scattered photons, working distance usually only reaches 10-20 μm [5].

At longer distances, multiple scattering events efficiently deviate the photon propagation direction from the optical axis, resulting in light diffusion at the distance defined by transport mean free path (TMFP). The TMFP is expressed as $1/(1-g)\mu_s$, where the parameter g reflects the probability of scattering in the forward direction [6]. In real tissues, g is in the range of 0.8–1 and results in TMFT values about 1 mm [5, 7]. These distances could be covered by advanced imaging techniques such as confocal and multiphoton microscopy, whose efficient mechanisms of scattered light rejection allow for extending the penetration depth to the range of several tenths of micrometres up to one millimetre [5, 8] (see Sec. 1.5 for more details on advanced in-depth imaging).

Imaging with optical methods beyond the depth defined by TMPF is an ongoing challenge in modern microscopy, mostly driven by the urgent need to gain an access to deeply located tissues for further studies of biological processes in vivo.

1.2 Complex photonics: dealing with scaterring media

Advancement of spatial light modulators (SLM), allowing precise control of the wavefront through a computer, has opened the way to address a number of problems related to wave propagation in complex environments where the light undergoes multiple scattering [9]. Recently developed digital holography methods allow focusing and imaging through scattering media, which is particularly relevant for bioimaging applications, where, as was explained in the previous section, natural inhomogeneities in tissues significantly compromise penetration depth. The first experiments reveal the possibility to focus the light through and into the turbid medium by tailoring an input wavefront

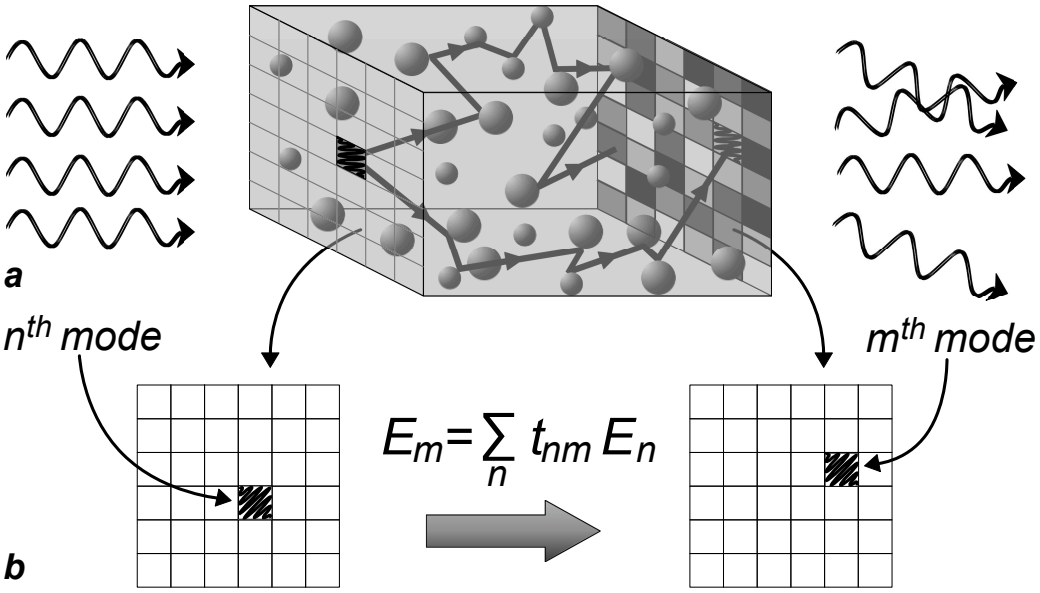

FIGURE 1.2: **Light propagation in a turbid medium.** **a** Wavefronts transmitted through a turbid medium are distorted due to multiple scattering events. **b** The output modes E_m are related to the input modes E_n through a transformation matrix which completely describes the optical propagation through the turbid medium.

[10, 11]. This idea gave birth to different wavefront shaping techniques including iterative algorithms [10, 12], time reversal or phase conjugation) [13–15], and the concept of transformation matrix (TM) [16, 17].

Probably one of the most established and influential approaches to deal with scattering is a measurement of the transformation matrix of a medium. Since scattering can be, in the majority of cases, considered as a linear process, the optical propagation within a scattering medium can be described in terms of a matrix of complex coefficients [17]. Arbitrarily complex incident and transmitted fields can be decomposed in sets of input and output orthogonal spatial modes, which are mutually related by the TM. This is schematically illustrated in Fig. 1.2. With the knowledge of a TM corresponding to a specific medium, one can simply calculate which phase and amplitude distributions have to be provided in order to synthesise a desired light output. Separately, images transmitted through a turbid medium are typically transformed into an unrecognisable speckled pattern, but the original image can be recovered by deploying the TM [16]. In other words once the matrix is measured it makes the medium predictable and opens huge perspectives for the applications.

Although observations behind a turbid medium can be of practical interest in some applications, it is naturally much more desirable to achieve observations directly within the turbid environment itself; here, however, one

does not have access to direct observations of the output field. Feedback from within the turbid medium is therefore provided using solid, typically fluorescent particles, sometimes referred to as guide stars (due to their analogy from astronomical applications of adaptive optics) [10, 18]. In practice, this leads to the requirement of having such particles in the area of interest. Moreover, this does not allow for a full measurement of the TM, since one only has access to a single output mode. In cases where one does not operate in completely diffusive regimes, the neighbouring components of the TM can be approximated, up to an extent, by the so-called memory effect. In case the medium is reduced to a thin turbid layer the memory effect can be very large which, in turn, allows imaging without any *a priori* feedback from the imaging plane [19, 20]. Powerful techniques to eliminate the need for solid particles have also been identified in the employment of ultrasonic encoding [21, 22].

Although complex photonics, with all the potential described above, still has a long way to find its own niche in practical biomedical imaging, it made the optical community to revise the conventional views on optics, and allowed to benefit from the turbid media, which for centuries were considered as inapplicable and adverse in optical systems.

1.3 Beam shaping through multimode fibres

Optical systems have traditionally been understood as series of components acting in a predefined and determinate manner. This notion is currently undergoing a steep transformation due to rapid advances in the technology and methods for spatial modulation of light. Reconfigurable elements, such as computer-controlled holograms, now facilitate the deployment of unusual and frequently very complex optical media with physical or functional properties that bring significant advantages to particular applications. A good example of this concept is the holographic control of light propagation through multimode fibres, which allows turning a single fibre into a small footprint endoscopic probe for minimally invasive access to deeply hidden tissues.

When light propagates within a multimode fibre, the incident optical field is projected onto numerous concurent waveguide modes. Each of these travels with different propagation constants (or equivalently, different phase velocities), a process known as mode dispersion. Additionally, modes can couple to one another by exchanging energy due to bending or looping of the fibre, as well as to the presence of impurities and inhomogeneities within the fibre; this is known as mode mixing. Both processes combine to distort the original

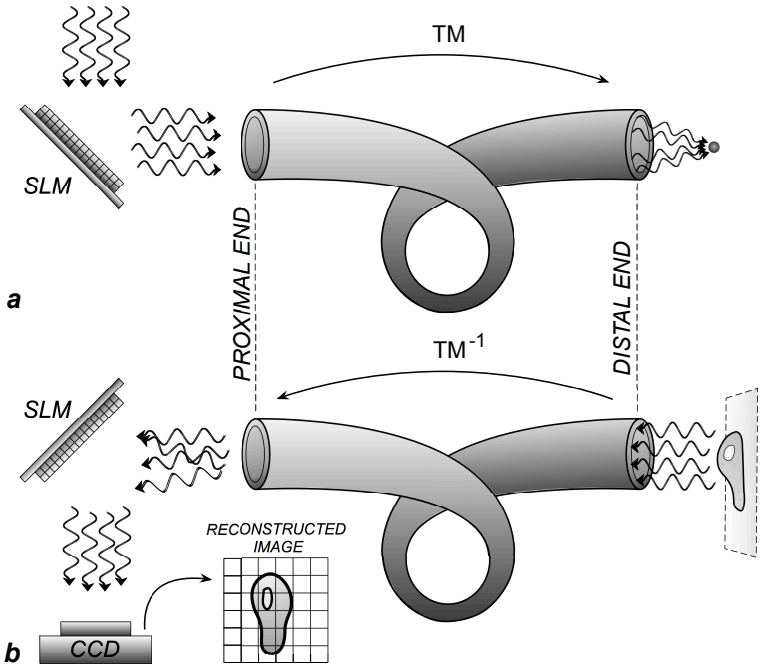

FIGURE 1.3: **The multimode fibre as a turbid medium.** **a** Focusing light through a MMF. With the knowledge of the transmission matrix (TM) of the fibre, one can spatially modulate the wavefront at the proximal end such that the optical field is tightly focused at a certain working distance from the distal fibre facet, producing an aberration-free diffraction limited spot. **b** Wide-field imaging through a MMF. Once the TM of the MMF has been determined, the optical field at a given distance from the distal end of the fibre can be retrieved from the speckled pattern originated at the proximal end.

wavefront, and upon propagation of just a few hundreds of micrometers, the resulting output field is a complex speckled pattern with little or no resemblance to the initial field distribution. Although relying on different physical mechanisms, the apparently randomising nature of light propagation in multimode fibres (MMFs) is thus somewhat analogous to transmission through turbid media. When it comes to bio-medical imaging applications, the TM of the optical fibre can be acquired prior to its application, with direct optical access to the distal end of the instrument. Once, past the calibration step (TM measurements), the fibre is ready be inserted arbitrary deep into the tissue, providing microscopy at the tip of a probe.

Analogies of the feedback algorithms mentioned above [23–25], the transformation matrix acquisition [26, 27], as well as the principles of digital phase conjugation [14, 28] have been successfully exploited to perform beam-shaping and imaging through MMFs. Fluorescent imaging [24, 26, 28] and micromanipulation [24, 26] can be performed by scanning a focused spot at the distal

end of the MMF, as schematically illustrated in Fig. 1.3 a. Scanner-free wide-field imaging has also been demonstrated. Here the acquired TM is used to retrieve the optical field at the distal fibre facet from the speckled pattern, either by physical inversion of the TM using a SLM [26] or by numerical post processing [27], as depicted in Fig. 1.3 b.

The recent past has witnessed a real acceleration of these possibilities. Most of the methods above have only been demonstrated using narrow-band laser light. This, unfortunately, stands in the way of introducing advanced methods of microscopy based on multi-photon excitation. In the pulsed regime, both the material and modal dispersions broaden the pulse in the time domain. A recent study, however, shows that purely spatial encoding can be used to optimise both the spatial and temporal domains. The authors were able to deliver focused sub-picosecond pulses through a 300 mm-long fibre, demonstrating two-photon absorption through the MMF [29].

Papadopoulos *et al.* demonstrated focusing beyond the diffraction limit of the MMF by placing a diffusive media in the distal end of the MMF, which increases the effective numerical aperture (NA) of the system [28]. Another approach to increase the imaging resolution in MMFs consists of illuminating the object with a sequence of random intensity patterns and reconstructing the image using a linear optimisation algorithm [30]. This technique demonstrated a two-fold increase in resolution compared to localised sampling. Due to growing interest in the field, researchers got access to custom-made fibres allowing to extend focusing and as a consequence, resolution ability of the probe up to effective NA of 0.6. Chapter 4 of this manuscript demonstrates implementation of a custom-made fibre probe with an ultra-high numerical aperture reaching 1 This allowed the more advanced biophotonic technique, of holographic optical tweezers, to be delivered through such a multimode fibre, providing three-dimensional micromanipulation in optically inaccessible complex environments.

For several years, the most significant criticism of these approaches has been seen in the necessity to perform imaging in rigid geometries. Any deformations of the fibre, such as those introduced by bending or looping, modify the TM of the fibre, which can severely deteriorate the image retrieved. Real-time measurement of the TM has been used to dynamically compensate for the fibre bending [31]. Another approach was based on a virtual coherent source serving as a beacon, by recording a permanent hologram in the distal tip of the fibre [32].

A radically new alternative in treating multimode waveguides, provides

a possible solution to the major issue of fibre bending, was introduced by Plöchner *et al.* [33]. Unlike other diffusive media consisting of highly disordered scatterers, optical fibres are actually homogeneous media featuring a remarkable cylindrical symmetry. Using an advanced theoretical description of light propagation and highly precise experimental methods, the authors have demonstrated that MMFs are in fact highly predictable systems. They could experimentally confirm the existence of propagation-invariant modes (PIMs) conserved upon propagation over distances as long as 300 mm. Furthermore, they have demonstrated the possibility to perform imaging with a TM predicted theoretically, thus completely eliminating the need for empirical acquisition of the TM. Such achievements also facilitated a detailed study of the influence of fibre bending, which introduced a major simplification of the problem and allowed the authors to perform imaging using the predicted TM in significantly deformed fibres with curvature reaching their long-term damage threshold.

The generation of the digital holograms is computationally demanding, and typically limits operation to pre-calculated holograms. Using the graphics processing unit (GPU) of a computer to perform the hologram calculation was also shown to improve the speed, by up to two orders of magnitude, allowing for real-time image control through MMFs at video rates [34, 35]. However, the main speed limitation, preventing the real microscopic application, is caused by the low refresh rates of light modulators, which defines imaging (scanning) rate for the vast majority of above-mentioned techniques. The next section presents an overview of the most established types of devices for spatial light modulation.

1.4 Liquid-crystal and Micro-Electro-Mechanical spatial light modulators

Nowdays, commercially available SLMs are based on either liquid crystal (LC) technology [36], or optical microelectromechanical system MEMS [37].

1.4.1 Liquid-crystal modulators

Originally developed for video projectors, LC-SLM promptly attracted scientific interest. Released in the late '90s, high-resolution full-phase modulators immediately found new applications in holographic optical tweezers, advanced microscopy, holographic displays, data storage and optical computing.

Over the last two decades, LC technology reached its maturity, now offering diversified set of devices. Using different LC material types, substrates and addressing methods, particular parameters can be optimised [38], making technology more flexible to cover a wide spectrum of applications.

For example, utilising the ferroelectric LC allows kHz level switching rates. Such devices only allow binary phase modulation and are usually used in off-axis configuration [39], which significantly reduces their efficiency.

Twisted nematic crystal based modulators can effectively modulate the polarisation of light and combined with polarisation film, it is now the gold standard of LC based screens and projectors [40, 41].

On the contrary, parallel-aligned (PAL) nematic crystals, since they have a linear arrangement of the molecules, allow precise control over phase having fixed polarisation state. Although most LC-SLMs are electronically driven / addressed, i.e. voltage applied to each pixel changes birefringence of LC material inside, there are optically addressed examples too [42]. Amplitude-modulated light, projected at the back plane of LC panel, steers the voltage across the LC layers, so having no physical pixel separation such devices can reach a fill factor close to 100%, yielding an ultra-high diffraction efficiency, which is particularly suitable for extremely low signal applications.

The closest competitor, in terms of efficiency, among electronically addressed devices uses liquid crystal on silicon technology (LCoS) [43]. While this only reaches a 90% fill factor, it brings substantial advantages, such as reduced cross-talk and smaller physical size.

1.4.2 Micro-Electro-Mechanical modulators

As well as liquid crystal technology, Micro-Electro-Mechanical or Micro-Opto-Electro-Mechanical Systems (MEMS/MOEMS) [44], began its rapid development in the '80s. MEMS devices have common major advantages when compared to LC. These are broad spectral range, high frame rate, possibility to operate with nonpolarised light and long lifetime.

At the end of the '90s it led to the entry of the first developed products for video projections based on two most successful technologies - Grating Light Valve (GLV) [45] and Digital Light Processing (DLP) [46]. The first one, based on reflective movable ribbons mounted on a silicon base, operates using a dynamically adjustable diffraction grating. Nowadays, it is mostly employed in

projectors for domes and planetariums, but the GLV also found its applications in computer-to-plate offset printing presses and dense wavelength division multiplexing components.

The second technology - DLP, uses a digital micromirror device (DMD). A DMD chip has on its surface several hundred thousand microscopic mirrors arranged in a rectangular array which correspond to the pixels in the image to be displayed. The mirrors can be individually tilted to an on or off state. Due to high switching rates of around 10s of kHz, colour channels can be displayed sequentially, and the greyscale (intensity modulation) is controlled using binary pulse-width modulation. Today, DMD based systems dominate the market of cinema and pico projectors and continue to oust LC-SLM in the sector of front projectors. Although such a great commercial success and mass production significantly reduced the price of DMD chips and made it affordable for lab usage, the lack of direct phase modulation limits its applications in photonics.

	DMD	LC-SLM
Refresh rate	23 kHz	200 Hz
Resolution	1024x768	512x512
Mode	1-bit amplitude	12-bit phase
Price	~ £5,000	~ £20,000

FIGURE 1.4: General parameters of DMD and LC-SLM.

Another notable member of the MEMS family is the deformable mirror, designed as a micromechanical analogue of light modulators, which is widely used in adaptive optics [47, 48]. Gathering all the advantages of MEMS together with the possibility of direct phase modulation, it has become one of the essential tools for wavefront correction in astronomy and microscopy as well as for pulse compression in ultrafast photonics. Designed specifically to work in the zeroth diffraction order, such devices have a very low resolution, but high speed of modulation (units of kHz).

Recent technological advances in lithography are another driver for the further development of MEMS-based phase SLMs. Most promising phase modulators based on pistonlike mirror arrays show high performance in both phase control and frame rate [49, 50]. Unfortunately, the availability of these devices on the market is limited, usually, they are ether designed internally in the company or custom made for the particular system. Growing industrial interest to holographic displays can dramatically change the situation in the next decade, making high-resolution and high-speed phase modulators available.

1.4.3 Choosing SLM for complex photonics

Due to high resolution and modulation depth, LC-SLM (LCoS PAL) is the most common solution so far for complex photonics applications. Providing high diffraction efficiency in the off-axis regime, the LC modulator is a perfect fit for high power demanding applications. A good example of such application is demonstrated in Chapter 5, where a LC-SLM was implemented for holographic optical tweezers through the MMF.

However, when considering imaging applications, and particularly those relying on the raster scanning of a laser focus inside or behind a complex medium [24, 26, 51], the SLM refresh-rate becomes a vitally important attribute. LC-SLMs have been employed in numerous pioneering experiments involving these forms of imaging, but with refresh rates at 10 - 200 Hz, acquisition of a single frame containing a few kilopixels of data typically takes several minutes [24]. Such low frame rate represents a severe obstacle for the majority of possible practical applications. The combination of LC-SLMs with a faster beam-steering technology has been demonstrated to accelerate acquisition rates by over two orders of magnitude, however, this solution significantly compromises maximum achievable pixel-resolution [26]. DMDs, which are based on micro-electro-mechanical systems (MEMS) technology, have therefore emerged as a powerful solution to this problem. Unlike LC-SLMs, which typically modulate the phase of the reflected wavefront with a depth of 8-12 bits, DMDs operate as purely binary amplitude modulators, posing a limit to the precision and efficiency with which each degree of freedom can be controlled [52, 53]. Nevertheless, it has been already shown that using a DMD in the off-axis regime [54, 55] makes it possible to measure the TM and to perform beam shaping through both a diffuser [56] and an MMF [27, 31] at very high speeds.

Chapter 3 presents a side-by-side performance assessment of LC-SLMs and DMDs as diffractive elements when applied across a wide spectrum of complex media, revealing series of non-obvious practical differences between the devices.

1.5 State of the art in light microscopy for deep-brain imaging

Throughout the whole of its history, neuroscience constantly relies on light microscopy techniques for brain observations at a cellular and sub-cellular level.

Evolving side-by-side, these fields walked a long way from first histological-only observations of cellular morphology by Golgi and Cajal, towards modern experiments, involving routine monitoring of cellular and circuit dynamics on timescales ranging from milliseconds to months. Recent tremendous progress towards advanced imaging techniques, functional dyes, and labelling methods, allowed to significantly extend the spectrum of applications across multiple spatial levels, ranging from sub-diffraction-limited microscopy of an individual cell to monitoring of thousands of cells distributed across a large volume. An ongoing challenge is to achieve high-resolution observations of neuronal activity in vivo inside deep brain areas. The typical scattering lengths, in other words, the distance over which scattering will reduce light intensities by a factor of $1/e$, in the brain are in order of 100 μm [57] for visible and around 200 μm for near-infrared spectral regions [58, 59].

1.5.1 Two-photon microscopy

Currently, two-photon microscopy is a golden standard for brain imaging [60], which allows using NIR light (less affected by scattering) to excite dyes with absorption lines located in the visible region of the spectrum, via a two-photon process. Applied in a raster-scan regime, this method implies harvesting a whole fluorescent response leaving the tissue, despite its route from exited volume towards a collection objective. These two factors allow reaching up to 750 μm of penetration depth [4]. Moreover, being a nonlinear process with a quadratic dependence of excitation rate on intensity, this technique allows for significant suppression of an out-of-focal signal as well as photobleaching. With all these advantages multiphoton imaging has greatly improved the understanding of the cellular and local circuit organisation involved in a variety of brain functions such as sensation, perception, cognition, and movement via visualisation of structures and functions of neurons in the living brain, particularly the cerebral cortex. Modern trends aim to broaden the detection area for studying neuron subpopulations and interlayer connectivity at the subcellular level [61–63]. A significant attempt was aslo made over the last decade in order to extend operation depth of two-photon microscopy, including:

- implementation of adaptive optics for active aberration correction [64–67];
- developing lasers and regenerative amplifiers with lower repetition rate to obtain higher energy pulses shows the potential for two-photon excitation at depths up to 1000 μm [68, 69];

- shifting towards even longer wavelengths around 1250 μm, using Cr: Forsterite lasers [70–72];
- switching to a three-photon regime, using laser systems with a wavelength around 1700nm for excitation of red fluorescent dies provides the means for imaging at the depths exceeding 1100 μm [8].

In conclusion, multiphoton microscopy, being already a clear leader among non-invasive deep-brain imaging techniques, has a potential to extend the applicability to the whole neocortex region of the animal model (up to 1000 μm depth for mice). Access to deeper located regions usually implies surgical removal of overlying tissue and implantation of an imaging window or microendoscope.

1.5.2 Microendoscopy

The microendoscope is a thin, usually rigid, optical probe, typically 350–1000 μm in diameter, which guides light to and from deep tissue locations, allowing in-vivo imaging of previously inaccessible brain regions [73–79].

Despite differences in fundamental principals of operation and design, microendoscopes usually act as an optical relay, allowing introduction of various microscopic techniques, including epifluorescence [74, 77, 78, 80], confocal [81], two-photon [73–75], second-harmonic generation [79, 82], light sheet microscopy [83] and even super-resolution imaging [84] deep inside the brain.

GRIN lens based endoscopes

Nowadays the most established techniques of microendoscopy are based on the gradient-index (GRIN) lenses/rods with parabolic-like lateral profile of refractive index, mimicking Hopkins' concept of conjugated lenses, which relay image from one facet of the rod to another.

Single rod designs, as well as composite probes, totally dominate among all other endoscopic concepts used in neuroscience, for example, 5 out of the 6 above-mentioned imaging techniques, which were successfully applied for deep-brain imaging, were implemented through GRIN rod based probes.

Commercially available probes, with diameters starting from 350 μm and numerical apertures reaching 0.5, show a good fit to tough constraints for brain imaging, providing up to $\sim$1 μm lateral and $\sim$10 μm axial resolutions [74, 75, 85]. Despite the advances in the development of index profiles optimised for imaging, the resolution of such systems is not limited by diffraction, but rather

by optical aberrations within the endoscopic probes. Due to the shape of index-profile, effective NA is not uniform across the facet, so the highest achievable resolution is restricted to the central region of the lens and fades out towards its edge, which could lead to excessive tissue damage caused by outer parts non-proficient for imaging.

The small size of GRIN lenses inspired the development of miniaturised head-fixed microscopes for imaging in freely behaving animals [85–89]. Although scaling down the optical schemes led to increased aberrations and, as consequence, a drop in resolution, this concept is still the most established and even commercially available way of observation of neuronal activity in motile animal models by the means of light microscopy.

Fibre bundle

Traditional endoscopes based on fibre bundles allow transferring the image from distal to proximal end, by probing an intensity in each core independently. Such probes usually suffer from low spatial resolution, because they required significant inter-core spacing to prevent cross-talk. Although miniature fibre bundles are commercially available with diameters down to 160 μm (contains only about 1600 cores), they cannot offer sufficient resolution for imaging of neuronal structures, which was proven by early in-vivo studies [90, 91].

In order to increase the resolution (at cost of field of view), magnifying optics could be placed on the distal end of the bundle. This consists of a set of microlenses [92, 93] or a grin lens [83, 94] attached to the tip of the fibre. Although a series of different high-resolution imaging techniques were successfully implemented through fibre bundles, including confocal, structured illumination and light sheet microscopy, there are only two reported attempts of their application for brain imaging. In both cases, bulky optical components on the distal end of the fibre led to the removal of significant volumes of the brain during the implantation process. However, recent works on holographic beam shaping through the lensless probes [95], reaching diffraction (NA) limited performance, as well as miniature micro objectives 3D printed directly on the fibre tip [96], can in the near future make bundles more appealing for neuroscience, especially taking into account their inherent bending insensitivity.

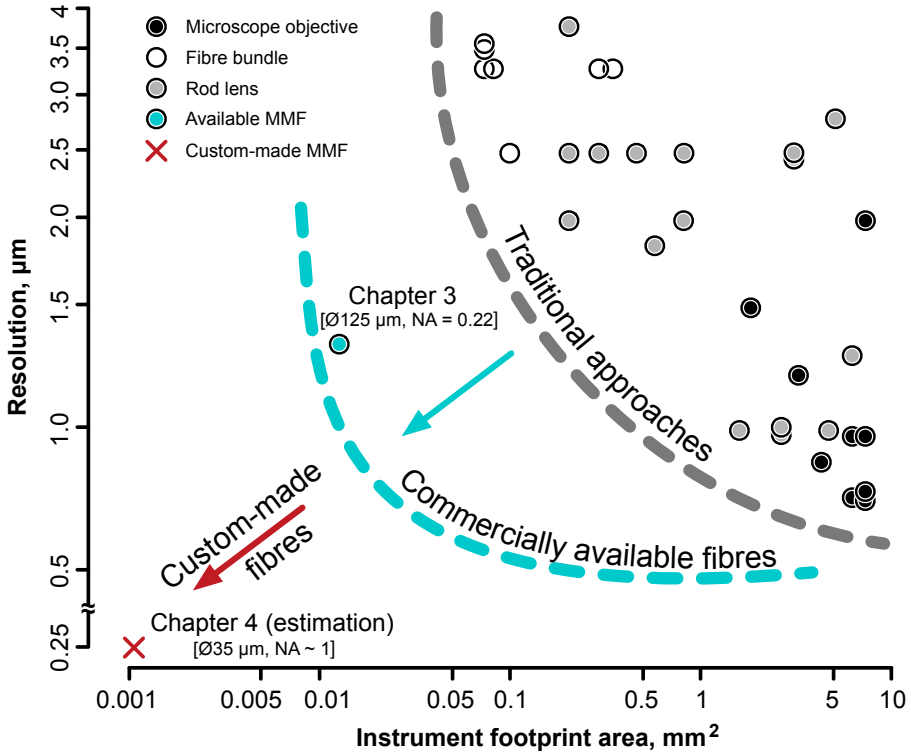

FIGURE 1.5: Trade-off between resolution and instrument's foot print for light-microscopy approaches implemented in vivo. The blue circle represents a result demonstrated in Chapter 4. The red cross shows estimated performans of custom-made fibre probe used in Chapter 5. *Remastered from [97].*

1.5.3 Holographic microendoscopy through multimode fibres

Rapid progress in neuroscience research, particularly relies on access to living brain tissue with minimal affect on its functions, which dictates further miniaturisation to overcome existing constraints. For example, the network of blood vessels in the cortical region can have spacings as small as 200 μm [98], as well as works on micro-electrophysiology claim significantly increased detrimental effects on the rodent brain (compression and damage to the surrounding neuronal processes) caused for probes wider than 60 micrometres [99].

Multimode optical fibres are thin glass waveguides, which typically have much smaller diameters than currently avaliable endoscopic probes. Exploiting MMFs as ultra-narrow, minimally invasive endoscopes is a promising example of the active, or reconfigurable optics, conception since it allows overcoming the trade-off between the size of the optical element and the attainable resolution, inherent to any lens-based systems. Note that such a compromise does not exist in GRIN rods. However, holographic approaches shaping

light propagating through MMFs into beams applicable for microscopy, naturally take into account aberrations in the whole optical system, including those caused by components and alignment imperfections. As a result, such active methods allow utilision of the whole NA of the probe, reaching diffraction limited performance (in contrast with rod lenses). Moreover, fibres with a step index profile can provide a uniform resolution across the whole region restricted by the core.

Figure 1.5 summarises the relation between image resolution and instrument's footprint for the most successful (to date) microendoscopic implementations in vivo. The point marked with blue stands for the result demonstrated in Chapter 3 of this thesis. Utilising commercially available 50 μm core fibre with NA of only 0.22, allowed significant miniaturisation of the probe, but at the same time resolution comparable with best results achieved via rod lens based microendoscopes.

One of the barriers for the further development of the technology is the fact that the market for optical fibres is mostly driven by applications in communication, which limits the selection of available options especially in terms of the NA. A whole new class of optical fibres should be developed to suit novel applications in biophotonics. One of the first steps in this direction, covered in Chapter 4, demonstrates holographic focusing through the custom-made fibre, with the core diameter of 20 μm and NA reaching 1. Although the novel probe has not been applied for imaging in vivo yet, it shows the potential for significant improvements in imaging resolution, reaching the performance of the best imaging objectives (depicted in Fig. 1.5 by red arrow).

Holographic endoscopy is a young but hot topic. Over less than a decade of its history, a number advanced microscopic techniques were successfully implemented through fibre probes, demonstrating epifluorescent [26, 51], multiphoton [29], computational analogous to confocal [100] and light-sheet [101] imaging. Recent studies also pave the way for active bending compensation [33] and development of the probes with sufficient bending resilience [102], which can potentially allow flexible operation of holographic microendoscopes and extend the spectrum of MMF applications in deep-brain imaging to studies in motile animals.

Chapter 2

DMD based spatial modulation of intensity, phase and polarisation.

An urgent need for high modulation rates, essential for any practical application of MMF-based imaging concept, left us with only one option available on the market, the DMD, which is inherently limited to binary amplitude modulation. This chapter briefly covers the off-axis holographic method of complex modulation, capable of spatial shaping of phase, amplitude and polarisation of light via a single DMD chip. As proof of this ability, the following experimental results demonstrate the generation of vector beams and their switching at the maximum refresh rate of DMD module.
The experiment presented in this chapter was initiated and conducted in collaboration with the Optics group of the University of Glasgow. The candidate took part in the building of the experimental setup and independently realised the synchronisation scheme for a fast camera with a DMD module.
The detailed examples presented by the collaborators allowed the candidate to quickly accumulate a basic set of skills in programming the FPGA-based DMD module. Moreover, this work allowed testing of the synchronisation scheme in the conditions of a real experiment. These aspects served as a springboard for future work in which the development of specific control procedures and highly synchronised work of the DMD are vital.

Related paper:
*Mitchell, K. J.,***Turtaev, S.**, *Padgett, M. J., Čižmár, T., & Phillips, D. B. "High-speed spatial control of the intensity, phase and polarisation of vector beams using a digital micro-mirror device."* ***Optics express****, 24(25), 29269-29282,* ***2016****.*

2.1 Lee hologram method for complex modulation

The modern market of DMDs offers various models with resolution reaching 4k format, which provides the user with millions of degrees of freedom (pixels) for light control. This allows keeping spatial resolution high enough, even while employing complex modulation approaches, which are usually based on diffraction from groups of pixels/mirrors to modulate the phase, therefore significantly reducing effective resolution.
The approach implemented in this work, known as the Lee hologram, was introduced more than 50 years ago and allows for tailoring a desired complex field in the first order of diffraction formed by binary amplitude gratings [52, 103]. The simplest case of a single grating displayed on a DMD chip is depicted in the Fig. 2.1. Here, a pitch of the grating defines the angle of the first order of diffraction and, as a result, position of the beam focus on the CCD camera. The lateral shifting of the grating allows modulating the phase of the diffracted light, while a duty cycle controls the amount of light redirected towards a first order, in other words, intensity.

Extending this approach to a general case, multiple gratings with individual parameters, locally applied to the DMD, enables generation of beams with elaborate amplitude and phase profiles. The amplitude hologram $H(x,y)$, resulting in formation of desired complex modulation $\mathbb{A}(x,y) = A(x,y)\exp^{i\phi_A}$ in the first diffraction order, could be calculated via:

$$H(x,y) = \frac{1}{2} + \frac{1}{2}\,sgn[\,cos(p(x,y)) + cos(q(x,y))\,], \tag{2.1}$$

where:

$$p(x,y) = \phi_A(x,y) + \phi_{grat}(x,y), \tag{2.2}$$

$$q(x,y) = \arcsin(A(x,y)/A_{max}). \tag{2.3}$$

Here (x,y) is Cartesian coordinates, sgn - sign function, phase term $p(x,y)$ consist of target field's phase ϕ_A and linear phase ramp $\phi_{grat} = 2(u_0x + v_0y)$, which defines carrier grating and results in angle of the first diffration order,u_0 and v_0 are constants determining the gradient of the phase ramp; $q(x,y)$ depends on normalised amplitude of the target field $A(x,y)/A_{max}$.

Applied to the DMD and illuminated with a coherent light source, such pattern (Eqn 2.1) forms the desired spatial mode, which is carried by the diffraction orders. One of the diffraction orders, usually the first (due to the highest power), could be isolated in the Fourier plane of the DMD by an iris and aligned with the optical axis of the system. In order to prevent overlapping

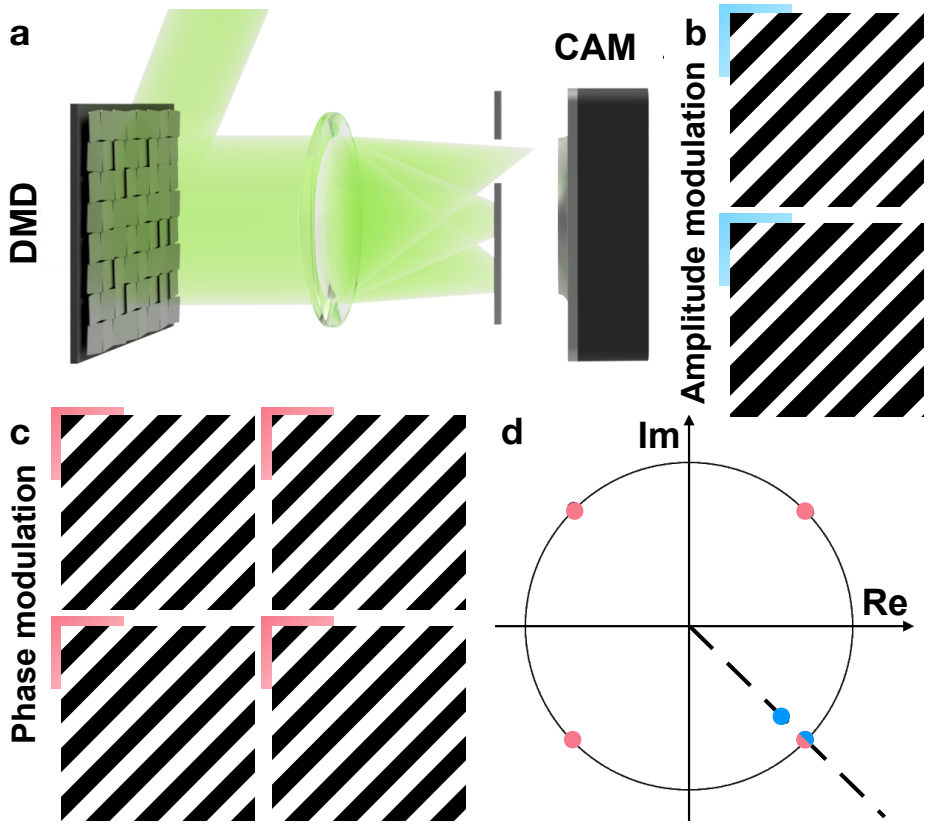

FIGURE 2.1: Illustration of the Lee hologram method utilising binary amplitude gratings for off-axis amplitude and phase (complex) modulation. **a.** Hypothetical demonstration setup operating in the first diffraction order. **b.** Example of amplitude modulation via variation of duty cycle of the grating. **c.** Example of phase modulation via a lateral shift of the grating. **d.** Gaussian (complex) plane depicts the modulations caused by the gratings illustrated in cases **b** (blue) and **c** (red).

with other orders of diffraction in the far field, spatial frequencies of the target field should not exceed $\sqrt{u_0^2 + v_0^2}$.

2.2 Experimental setup

Figure 2.2 shows a schematic of the experimental setup. It is based on the LC-SLM driven scheme described in the supplementary material of [33], which was previously used to measure the complex transmission matrix of a multimode fibre and to generate the full basis of vector fibre modes. In the present work this scheme was chosen, since it offers a high level of stability, due to the common pathway taken by both beams through the optical system, which minimises the effects of drift in the relative path lengths. A horizontally linearly polarised Helium-Neon laser beam is expanded (using lenses F1 and F2)

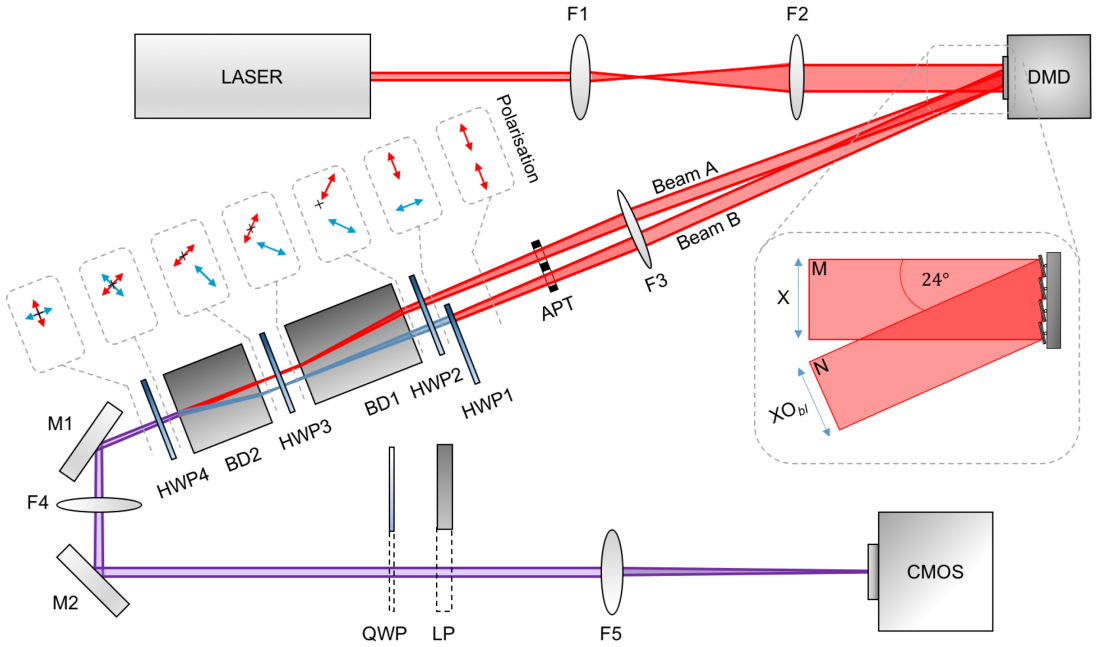

FIGURE 2.2: Experimental setup. Laser: Zeeman stabilised HeNe laser Neoark Neo-262; DMD: Texas Instruments DLP LightCrafter evaluation model with a 0.3 WVGA chipset; BD1, BD2: calcite beam displacers ThorLabs BD40 and ThorLabs BD27; CMOS: camera Prosilica GC660 / Mikrotron EoSens CL MC1362; Lenses: F1 = 40 mm, F2 = 160 mm, F3 = 300 mm, F4 = 200 mm, F5 = 150 mm; M1, M2: silver mirrors; HWP1-HWP4: multi-order half-wave plates; APT: custom made aperture with two openings; Quarter-wave plate (QWP) and linear polariser LP, can be inserted for spatially resolved polarisation measurments.

and collimated to overfill the active area of the DMD chip. It is helpful to ensure that the orientation of the linearly polarised light incident on the DMD is parallel or perpendicular to the axis of rotation of the micro-mirrors. This prevents undesired path length changes due to any differences in the polarisation dependent Fresnel coeffcients of the mirrors introducing ellipticity into the beam polarisation after reflection from the DMD. The pattern displayed on the DMD is designed to diffract light into two independent orders, transmitted at different angles from the DMD, denoted here as beams A and B. The DMD pattern also enables independent spatial control of the local intensity and phase of light diffracted into each order. Lens F3 collects the transmitted beams, and after this an aperture blocks unwanted diffracted orders. The polarisation of beam B is then rotated by 90° using half-wave plate HWP1. Two beam displacers (BD1 and BD2) are then used to overlap the beams, which are now of orthogonal polarisations, back onto a common axis. Half-wave plates HWP2 and HWP3 are used to rotate the polarisation of both beams A and B by a fixed amount. This enables control of the combined displacement of the beams with respect to one another as they pass through the beam displacers.

HWP3 is used to rotate the polarisations of both overlapped beams so that they are once again either parallel or perpendicular to the tilt axis of mirrors M1 and M2. This means that any difference in path length between the vertical and horizontally polarised components due to reflection from these mirrors can be accommodated in the DMD pattern design (more detail below in Sec. 2.3). The relative polarisations of beams A and B as they pass through the beam displacers is also shown in Fig. 2.2. Lenses F4 and F5 re-image the vector beam onto a CMOS camera. The quarter-wave plate (QWP) and the linear polariser (LP) can be translated in and out of the beam and are used to make spatially resolved Stokes measurements (more details are given below in Sec. 2.4).

2.3 Spatial polarisation modulation

In our experiment, we aim to create a target vector beam of arbitrary intensity, phase and polarisation ($\vec{\mathbf{E}}(x,y)$), with the general form given by:

$$\vec{\mathbf{E}}(x,y) = \begin{bmatrix} E_A(x,y)e^{i\phi_A} \\ E_B(x,y)e^{i\phi_B} \end{bmatrix}, \tag{2.4}$$

where $E_A(x,y)e^{i\phi_A}$ and $E_B(x,y)e^{i\phi_B}$ are two scalar fields of orthogonal linear polarisation and independently spatially controllable intensity (e.g. E_A^2 for field A) and phase (e.g. ϕ_A for field A). We therefore require a binary transmittance function which generates these two scalar beams diffracting at different angles.We note that, upon transmission from the DMD, these beams are both initially horizontally linearly polarised as described above, and one beam then undergoes a 90° rotation of its linear polarisation, rendering them orthogonally polarised before they are overlaid onto a common optical axis. Therefore, in the general case, the two independent scalar fields (of common polarisation) transmitted by the DMD are given by: $\mathbb{A}(x,y) = A(x,y)\exp^{i(\phi_A+\phi_{A,ramp})}$ and $\mathbb{B}(x,y) = B(x,y)\exp^{i(\phi_B+\phi_{B,ramp})}$, where $\phi_{A,ramp}$ and $\phi_{B,ramp}$ are the phase ramps which specify the direction of each diffraction order. The amplitude hologram $H(x,y)$ is then calculated from a combined field $\mathbb{C}$, given by the weighted complex interferometric sum of $\mathbb{A}$ and $\mathbb{B}$:

$$\mathbb{C} = C(x,y)\exp^{i(\phi_C)} = W_{rel}\exp^{i(\phi_{global})}\mathbb{A} + (1-W_{rel})\mathbb{B}, \tag{2.5}$$

where W_{rel} is a real number between 0 and 1 which specifies the relative power sent into beams A and B (for example the power is nominally the same when W_{rel} is set to 0.5), ϕ_{global} controls the relative global phase between the two

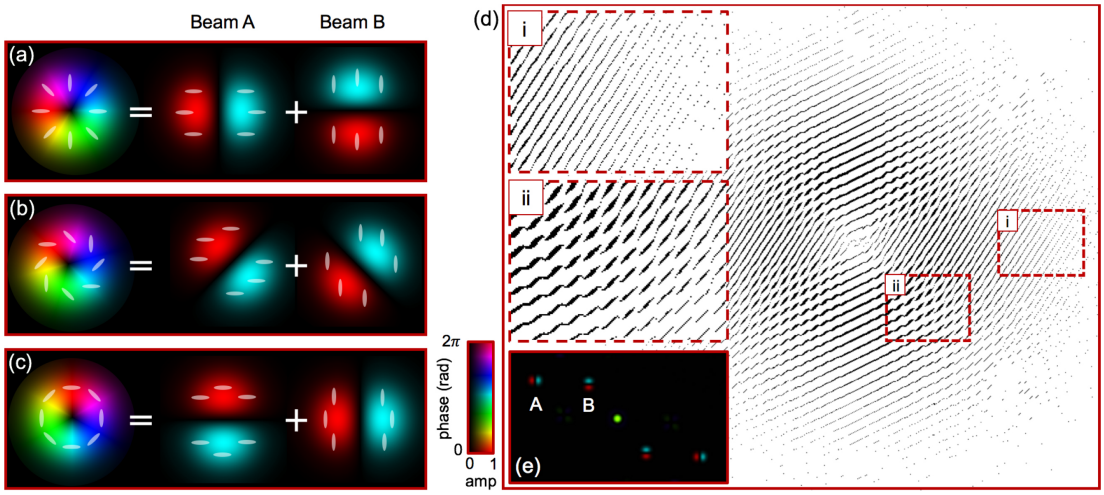

FIGURE 2.3: DMD hologram design: (a) A radially polarised vector vortex beam with a Laguerre-Gaussian ($LG_{l=1,p=0}$) intensity profile can be formed from the addition of a horizontally polarised Hermite-Gaussian ($HG_{n=1,m=0}$) spatial mode, and a vertically polarised $HG_{0,1}$ spatial mode. Here l and p are the LG vortex and radial spatial mode indices respectively, and n and m are the HG spatial mode indices. (b) A chirally polarised vector vortex beam (i.e. the polarisation structure is chiral in nature) is formed from the addition of two rotated HG beams of orthogonal linear polarisations. (c) An azimuthally polarised vector vortex beam is formed from the addition of a horizontally polarised $HG_{0,1}$ spatial mode and a vertically polarised $HG_{1,0}$ spatial mode. (d) A binary transmittance function displayed on the DMD to generate the radially polarised beam shown in (a). This was designed using Eqns. 2.1-2.5, where A and B are the appropriate HG modes shown in (a) each incorporating a different phase tilt to transmit them in different directions. Here, we show the negative of the transmission function (i.e. white represents regions where incident light is blocked, and black where it is transmitted). The insets show regions of the pattern in more detail: (i) a region that diffracts light predominantly into beam A, (ii) a region that diffracts a similar intensity of light into beams A and B. (e) A simulation of the field at the Fourier plane of the DMD when displaying the binary transmittance function shown in (d), showing beams A and B spatially separated and with independent intensity and phase profiles. The central beam is the zero diffraction order, and the beams are copied in the lower right quadrant due to the binary nature of the diffraction grating.

orders. Therefore, to design a binary amplitude hologram for the the combined beam using Eqn 2.1, we now have $p(x,y) = \phi_A(x,y)$, and $q(x,y) = \arcsin(C(x,y)/C_{max})$. The functions A and B depend upon the target vector beam, and can be calculated by decomposing it into two orthogonal linearly polarised components. This process is similar to that described in [104] for the generation of vector beams using an LC-SLM. In general, the local polarisation state may be defined by a polarisation ellipse, and the relative local phase difference of the electric field of the two orthogonal linearly polarised components determines the ellipticity of the local polarisation state of the vector beam. For example, a phase difference of zero (or π, or 2π) radians specifies

a linear polarisation state, a phase difference of $\pi/2$ radians specifies circular polarisation, and other phase values specify elliptical polarisation. The orientation of the major axis of the polarisation ellipse is specified by both the local relative phase and the local relative amplitude of the two orthogonal linearly polarised components. Therefore, the intensity, phase and polarisation of the vector beams are necessarily coupled. However, similar to [104], our method enables full control of both phase and polarisation as we have arbitrary control of both (i) the relative phase of the electric field of each polarisation, and (ii) the relative phase of the oscillating electric field of adjacent spatial locations within the beam. Figure 2.3 shows an example of the binary transmittance function calculated to generate a radially polarised vector beam [105]. As can be seen in Fig. 2.3 a, the vector beam has a helical Pancharatnam-Berry phase, indicating that the beam carries orbital angular momentum with a vortex charge of l= 1 [106]. This is a geometric phase arising from the rotation of the local polarisation state as the beam axis is orbited [107, 108]. The radially polarised beam can be decomposed into two orthogonal linearly polarised beams, each consisting of two lobes that are out of phase by π (and depending on the exact radial intensity profiles these orthogonally polarised beams may be described by Hermite-Gaussian HG_{10} and HG_{10} spatial modes [109]). The intensity and phase of these two fields therefore define the functions $\mathbb{A}$ and $\mathbb{B}$ used to design the DMD pattern. In addition, A and B can also incorporate aberration correction phase functions if necessary. These functions are the phase conjugate of any phase distortions imparted to the beam anywhere along either of the two beam paths. If necessary, these functions can be measured in-situ along each beam path independently, using the methods described in [18]. We found that the phase flatness of our DMD model (described in the caption of Fig. 2.2) was extremely good, and so this was unnecessary in our experiment. Finally, the relative amplitude (W_{rel}) and global phase (ϕ_{global}) terms enable a simple way of empirically fine-tuning the hologram pattern to ensure accurate generation of the required polarisation states. W_{rel} is used to cancel any differences in diffraction effciency with diffraction angle from the DMD (due to the envelope function of the diffraction grating). ϕ_{global} is used to accommodate any path length differences taken by beams A and B through the set-up.

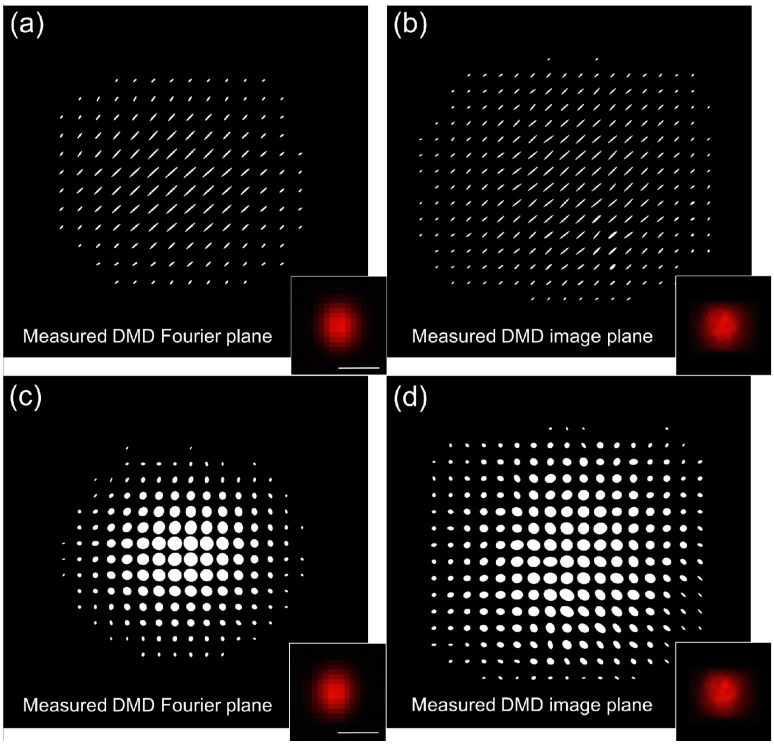

FIGURE 2.4: Experimentally generated vector beams with uniform polarisation. Upper row: (a) Generation of a diffraction limited beam (i.e. generated by diffracting light from over the entire face of the DMD) of diagonal linear polarisation in the Fourier plane of the DMD. This is formed from beams A and B of equal power with a zero radian phase shift between their electric fields. Inset shows the intensity of the beam. Scale bar = 50μm. (b) The same beam as in (a) now viewed in the image plane of the DMD. (c) Generation of a diffraction limited beam of circular polarisation in the Fourier plane of the DMD. This is formed from beams A and B of equal power with a $\pi/2$ rad phase shift between their electric fields. (d) The same beam as (c) now viewed in the image plane of the DMD.

2.4 Vector beam generation and measurement

We first demonstrate the generation of uniformly polarised beams which combine light from both beams A and B with a controlled phase offset, and investigate their propagation stability by measuring the polarisation state in both the Fourier plane of the DMD (camera positioned as shown in Fig. 2.2) and image plane of the DMD. The polarisation state across the beams was measured by performing spatially resolved Stokes measurements. This was achieved by measuring the intensity of light that was transmitted through the following

six polariser configurations: vertical (a measure of $|E_v|^2$, where E_v is the vertical component of the electric field), horizontal ($|E_h|^2$), diagonal ($|E_d|^2$), anti-diagonal ($|E_a|^2$), left-handed circular ($|E_-|^2$), and right-handed circular ($|E_+|^2$). The final two measurements were achieved with the combination of a quarter-wave plate followed by a linear polariser as shown in Fig. 2.2. To transform these measurements into polarisation ellipses, we follow the analysis detailed in [110] to calculate the magnitudes of the major (P_{major}) and minor (P_{minor}) ellipse axes, the orientation of the major axis (θ) and the handedness (h). Therefore:

$$P_{major} = \sqrt{\frac{1}{2}(I_p + |L|)},\ P_{minor} = \sqrt{\frac{1}{2}(I_p - |L|)},\ \theta = \frac{1}{2}arg(L),\ h = sgn(V), \tag{2.6}$$

where:

$$I_p = \sqrt{(|E_v|^2 - |E_h|^2)^2 + (|E_a|^2 - |E_d|^2)^2 + (|E_-|^2 - |E_+|^2)^2}, \tag{2.7}$$

$$L = (|E_v|^2 - |E_h|^2)^2 + i(|E_a|^2 - |E_d|^2)^2. \tag{2.8}$$

In all of our results, the relative length of the major axis has been scaled in proportion to the local intensity of light in that region of the beam. Figure 2.4 demonstrates the generation of vector beams with diagonal linear polarisation, and circular polarisation when utilising the full aperture of the DMD. Therefore, a diffraction limited spot is created in the Fourier plane (Fig. 2.4 a,c). The measurements in the image plane of the DMD (Fig. 2.4 b,d) reveal the Gaussian illumination intensity clipped by the rectangular aperture of the DMD. The key point here is that we see that the target polarisation is produced in both the Fourier and image plane of the DMD, because in this experiment, the scalar components of our modes are propagation invariant and therefore have the same profile in the image plane or Fourier plane save for a magnification and a phase term [111].

2.5 Validation of high-speed complex modulation

We now demonstrate the high speed switching capability of the DMD. Figure 2.5 shows a series of images of the beam once it had passed through a linear polariser, recorded with a high-speed camera (see caption of Fig. 2.2), as the pattern on the DMD is switched at a rate of 4kHz. We preloaded 10 patterns designed to switch the vector beam gradually from a radially polarised to azimuthally polarised state, by locally rotating the polarisation through a

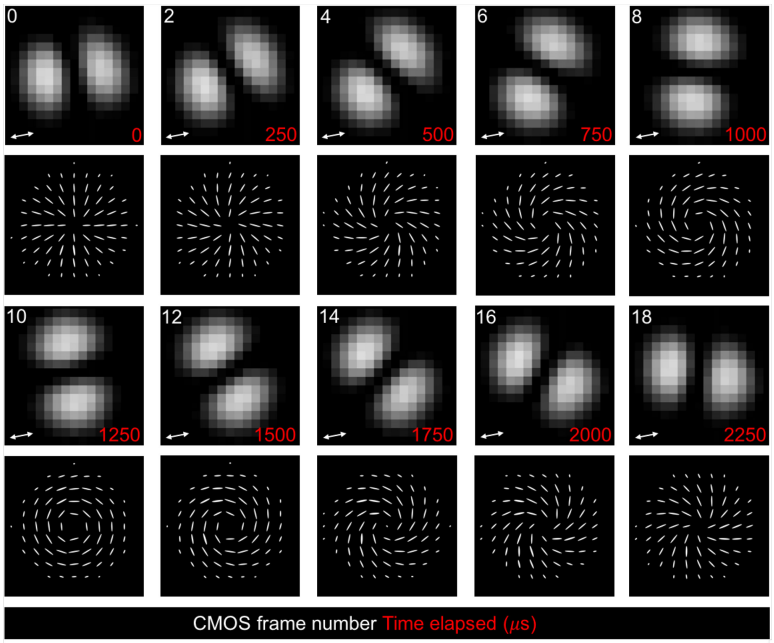

FIGURE 2.5: High-speed beam switching using a DMD. Upper panels (spinning lobe images): images of the generated beam captured through a static linear polariser at 7 kHz with a high-speed camera, as the DMD cycles through a series of 10 preloaded patterns at a rate of 4 kHz. The orientation of the transmitted polarisation is shown as a white arrow in the lower left hand corner of each panel. We show every second camera frame, and the elapsed time of each frame is also shown in red. The high-speed rotation of the lobes indicates the rotation of the local polarisation within the beam from one DMD pattern to the next. Lower panels (polarisation maps): Experimentally reconstructed polarisation maps of the beam for each DMD pattern. The polarisation map data was not collected at high speed, as it required the recording of multiple images of the beam transmitted through different polariser positions as described in Section 2.4.

series of chirally polarised states. For each of these 10 preloaded patterns a full measurement of the polarisation state of the generated beams was made separately. Figure 2.5 shows these 10 polarisation maps adjacent to the high-speed camera images.

2.6 Conclusions

The present work demonstrates the use of a DMD for the generation of beams with spatially varying intensity, phase and polarisation. The employed technique creates two beams of orthogonal polarisation, which are then overlaid back onto the same optical axis with locally controllable relative intensity and

phase. A key advantage of the demonstrated setup is its high stability, due to the common pathway taken by both beams through the optical system, which minimises the effects of drift in the relative path lengths. We have analysed the polarisation of the resulting beams using spatially resolved Stokes measurements, which show good agreement with theory. A beam switching rate of up to 4 kHz was reached, limited only by our DMD model (Texas Instruments DLP LightCrafter). This model of DMD also has the advantage of being relatively inexpensive (approximately an order of magnitude less than a typical LC-SLM), and so represents a low cost beam shaping device. More expensive and faster DMDs have switching rates in excess of 22 kHz, which is almost 2 orders of magnitude higher than the fastest currently commercially available models of LC-SLM, which operate at up to 500 Hz.

The relatively high switching rates offered by DMDs are achieved at the expense of a reduction in diffractive beam shaping efficiency, which in the presented experiments reached 2-5%. However, with the growing availability of relatively high power lasers and sensitive detectors, many applications are suited to the prioritisation of high switching speed over generation efficiency. Demonstrated high-speed complex modulation capabilitiy is required for the control of light propagation through multimode fibres, where high-speed is essential for any practical implementation in endoscopy.

Chapter 3

Liquid-Crystal and MEMS based modulators for complex photonics

Most of the pioneering studies in complex photonics were initially conducted using liquid-crystal spatial light modulators, due to their high dynamic range and depth of phase modulation. Nowadays, however, their relatively low refresh rates remain an obstacle in the translation from the proof-of-concept stage to practical applications, necessitating an effort from the scientific community to search for alternatives. As mentioned in the introduction, and shown in the previous chapter, DMDs allow complex light modulation at refresh rates significantly higher than those of the currently most established liquid-crystal (LC) based modulators. This fact, together, with their relatively low price, makes DMDs promising candidates for implementation of multimode fibre based imaging concept.

Being visually similar, LC and DMD modulators are based on fundamentally different technologies, which leads to a set of unique features in the operation of the devices, beyond the obvious difference in high-speed operation and diffraction efficiency. Additionally, taking into account the variety of application scenarios in complex photonics, it is almost impossible to predict which modulator is more suitable for which case, and what is the price to pay in terms of performance when switching from one to the other.

To the best of our knowledge, this chapter presents the first comparitive study on the capabilities of both technologies, when applied to light control in complex media. The demonstrated quantitative assessment of the performance for techniques commonly used in this field covers three regimes of media complexity: first, we study light control in a ballistic regime, eliminating aberrations of an optical system; second, we explore the performance in a diffusive regime, forming diffraction-limited foci through a ground-glass diffuser; finally, we analyse the quality of foci, formed by controlling the light propagation through a multimode optical fibre.

Surprisingly, the obtained results reveal that the light-modulation fidelity achieved by a MEMS-based device is not compromised by its inherent limitation of binary amplitude modulation, if applied in the off-axis regime. Moreover, additional features, such as scattering- and flicker-free operation, are shown to provide further quality enhancement of wavefront shaping in all considered regimes.
This seemingly routine study gave a chance to, not only to expand the candidate's understanding in dealing with main archetypes of complex media, but to implement and test holographic beam-shaping methods on a DMD, which will be later applied in proving the concept of multimode fibre based imaging in vivo.

Related paper:
Turtaev, S., *Leite, I. T., Mitchell, K. J., Padgett, M. J., Phillips, D. B., & Čižmár, T. "Comparison of nematic liquid-crystal and DMD based spatial light modulation in complex photonics."* ***Optics Express****, 25(24), 29874-29884,* ***2017****.*

The contributions from the author of this thesis, to the work presented in this chapter, consisted of: (i) designing the experiment and assembling the setups, (ii) implementation of the holographic methods using the DMD, (iii) measurements performed with DMD based wavefront shaping, (iv) data analysis, and (v) contribution to the interpretation of results.

3.1 Experimental setup

To test the performance of LC-based SLMs and DMDs in the ballistic, diffusive, and intermediate (fibre) regimes, we designed a modular experiment, as shown in Fig. 3.1. The SLM (DMD/LC-SLM) is illuminated with a highly coherent linearly polarised laser beam at the 532 nm wavelength, operating in the off-axis regime so that modulated light is transmitted into the first order of the resulting diffraction pattern. In all presented experiments, for both the LC-SLM and the DMD, the active region of the modulator was limited to 512×512 pixels. Lens F1 together with aperture (APT) isolates the first diffraction order, which is then aligned with the subsequent optical components. In module 1, the CCD camera placed at the focal plane of lens F1 is employed for the aberration correction experiment in the ballistic regime. Module 2 is used to study focusing performance in the diffusive regime. Collimating lens F2, as part of the demagnifying telescope F1-F2, decreases the beam diameter on the surface

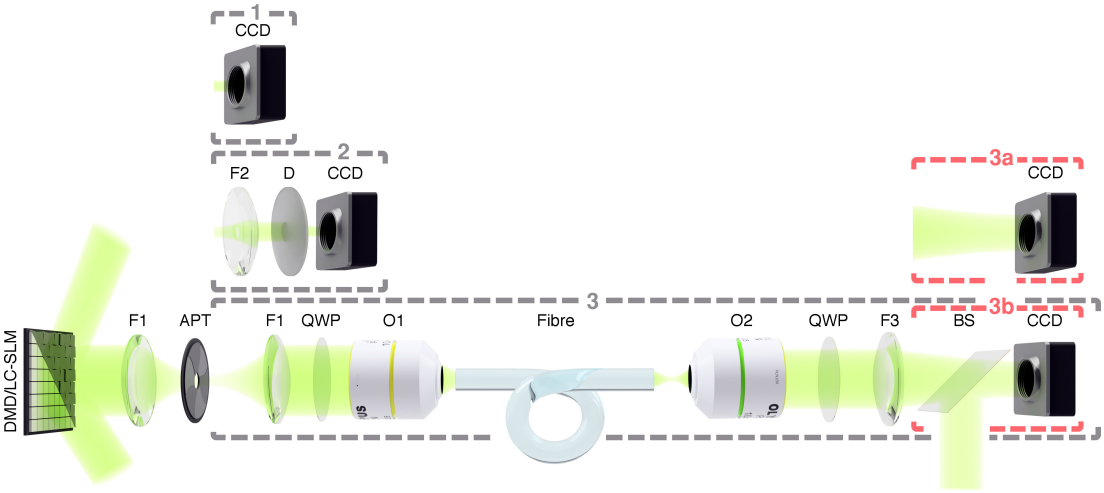

FIGURE 3.1: **Modular experimental setup. 1.** Ballistic regime. **2.** Diffusive regime. **3.** MMF with internal (**a**) or external (**b**) phase reference. **Laser**: Single-frequency DPSS laser at 532nm (Crystal laser CL532-075-S); **LC-SLM**: BNS HSPDM512; **DMD**: VIALUX V-7001; **CCD**: Basler pia640-210gm; Thorlabs Lenses: **F1**(AC254-200-A-ML), **F2**(AC254-25-A-ML), **F3**(AC254-200-A-ML); **APT**: Iris diaphragm (SM1D12D); **QWP**: Quarter-wave plate (Thorlabs WPQ05M-532); **D**: Ground glass diffuser (DG10-1500-MD); **Fibre**: 30cm long 0.22 NA multimode fibre (Thorlabs FG050UGA); **O1**, **O2**: Microscope objectives (Olympus RMS10X, RMS20X); **BS**: 50:50 non-polarising beamsplitter (Thorlabs BS004).

of ground glass diffuser D, in order to increase the amount of power reaching the CCD camera. In module 3, the SLM face is re-imaged to the back aperture of microscope objective O1. The MMF facet is at the focal plane of O1. Objective O2, together with tube lens F3, projects the desired focal plane of the fibre onto the CCD camera. Two quarter-wave plates (QWP) enable the coupling of circularly polarised light into and out of the MMF, which has been shown to be better conserved throughout propagation owing to the cylindrical symmetry of the waveguide [33]. Modalities 3a and 3b allow the MMF transmission matrix to be characterised either with an internal phase reference (3a) that has itself been transmitted through the MMF, or with an external reference (3b) provided directly from the laser source via beam splitter BS.

3.2 Holographic methods for beam shaping through complex media

3.2.1 Subdomain based wavefront shaping

As explained elsewhere [18], the wavefront correction technique used here is based on a decomposition of the initial laser field at the SLM plane into a series

of orthogonal modes, each corresponding to a different square region (subdomain) of the SLM. In our experiments, the size of the subdomains was varied from 32×32 down to 4×4 pixels (see Fig. 3.2 a), yielding a number of input modes in the system ranging from 256 to 16386. By modulating a particular subdomain with a grating, one can transfer part of the reflected optical power from the zeroth diffraction order into the first diffraction order at the Fourier plane. In the case of the LC-SLM, this is achieved using a blazed phase grating, which for the chosen periodicity of 4 pixels per period allowed 42% of the whole optical power to be redirected to the first order. A binary amplitude grating, applied in the case of the DMD [103], resulted in an efficiency of only 8% under the same conditions (see Fig. 3.2 b). In both cases, applying the grating over a subdomain is equivalent to turning the associated mode 'on' or 'off', as only light directed into the first order is allowed to propagate through the aperture (APT in Fig. 3.1) into the destination plane. As depicted in Fig. 3.2 b, if an internal reference is used, one such mode is selected as the reference, and all the remaining modes are examined one by one as follows: a mode under 'test', together with the reference mode, propagates through the optical system and interferes in the destination plane, giving an intensity signal that is monitored by a single CCD pixel. Altering the phase of the tested mode is achieved by laterally translating the grating applied to the corresponding SLM subdomain. Sweeping the phase of the tested mode at a uniform rate, results in a sinusoidal time-dependence of the recorded intensity. The phase of this sinusoid reveals the optimal phase at which the tested mode interferes constructively with the reference. Repeating this procedure for all the input modes and then turning all of them 'on' simultaneously with the optimal phase applied, results in optimal focusing as all modes interfere constructively at the same time.

The interferometric measurements of each subdomain were performed with phase-steps of $\pi/2$, and we separately studied the results obtained for a phase sweep of one and two full cycles (i.e. 2π or 4π). Changing the number of cycles in this way allowed us to assess the influence of temporal fluctuations in the efficiency of the modulator during the optimisation procedure. Known sources of temporal fluctuations in LC-SLMs include transfer delay, response time, and flicker [112]. Such fluctuations can affect the accuracy of the interferometric measurements and, consequently, the quality of the resulting wavefront correction. In our experiments, the issues with transfer delay and response time were mitigated by implementing a waiting time of 25 ms between uploading the phase hologram and triggering the camera; additionally, we used a Meadowlark / BNS XY-series LC-SLM, a model which

is well known to exhibit low levels of phase flicker – however, not eliminating it completely. Extending the measurements from one to two periods can improve the accuracy by averaging these influences out, but consequently also doubles the optimisation time.

The algorithm was implemented on both devices for all three aforementioned regimes of media complexity, the results of which are detailed in the following sections 3.3–3.5.

3.2.2 Plane waves based wavefront shaping

The final experiment was performed exclusively for the case of the MMF, featuring the advantages of the modified fast algorithm presented in [33] and schematically shown in Fig. 3.3. As an alternative to aberration measurement based on the division of the SLM into a grid of subdomains as described above, we investigate the performance of aberration measurement in the Fourier basis. Here, the tested modes are formed by plane waves truncated by the SLM chip, each being transmitted at a different angle from the chip corresponding to a specific $\vec{k}$-vector (see Fig. 3.3 a). Each such truncated plane wave forms a focused spot at a different transverse location on the input facet of the MMF (see Fig. 3.3 b). This orthogonal grid of foci forms a new basis of the modes. The distal end of the MMF is imaged on the CCD camera, where the output optical field interferes with an external phase reference. Analogously to the subdomain-based optimisation, for each such input mode, we search for the optimal phase, giving the highest signal at a chosen CCD pixel while interfering with a reference beam (see Fig. 3.3 c). In this case, the reference was external to the multimode fibre. This technique is slightly more demanding in the post-processing stage than the subdomain method as the reconstruction of the desired wavefront needs to be made in Fourier domain [33, 113]. However it has the advantage of making a more efficient use of the light transmitted from the SLM during TM measurement: firstly, each measurement involves light reflected from the entire face of the SLM, improving the signal-to-noise ratio of the measurements, and secondly, we only include truncated plane waves which result in focused spots incident within (and therefore coupled into) the fibre core. Ignoring modes that enter the cladding in this way, minimises the required number of measurements, therefore significantly decreasing the calibration time. In order to identify the location of the fibre core, the technique therefore requires a preliminary step: the raster scanning of the fibre facet with

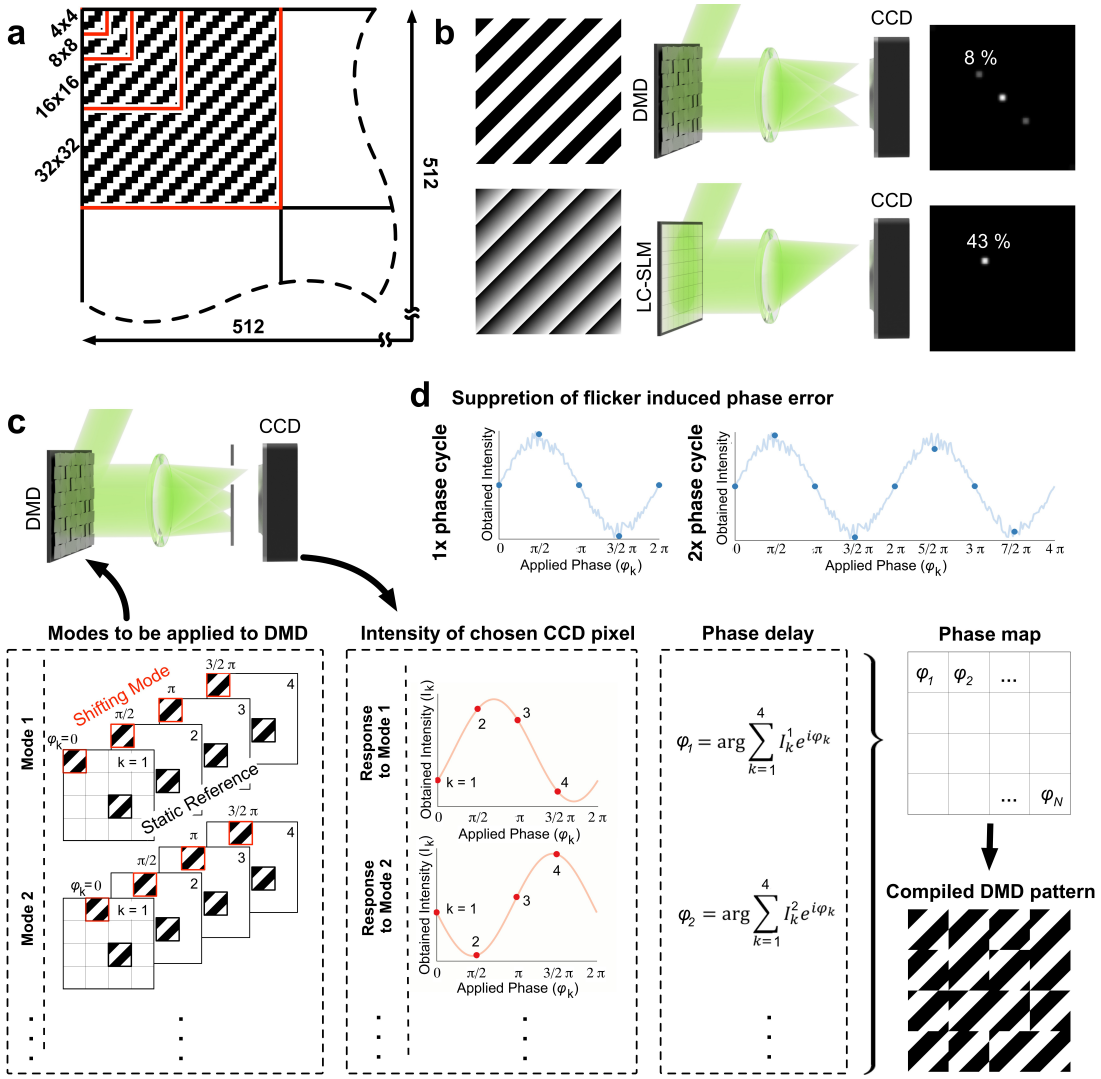

FIGURE 3.2: **Subdomain based wavefront shaping. a.** Sizes of subdomains used for the study. **b.** Off-axis phase modulation implementation on both DMD and LC-SLM. **c.** Division of the SLM into subdomains: one static subdomain serves as a reference, while all other subdomains are examined one at a time by applying and shifting the grating in four steps of period/4 (corresponding to a phase shift of $\pi/2$). The interferometric response recorded by the chosen pixel on the CCD camera allows measuring the phase delay between the active subdomain and the static reference. Repeating this procedure for each subdomain, allows reconstructing the phase map of aberrations in the system. Combined with the carrier grating (binary amplitude for DMD or sawtooth phase for LC-SLM), this map allows compensating the measured aberrations, and produces a focal spot at the initially chosen pixel of the CCD camera. **d.** Two periods of a phase shift could be used for averaging out phase noise (e.g. induced by a flicker of LC-SLM).

focal points, and the measurement of the integrated (total) output power (intensity) at the distal end of the fibre for each input scan position. This enables identification of those spatial modes which can be efficiently coupled

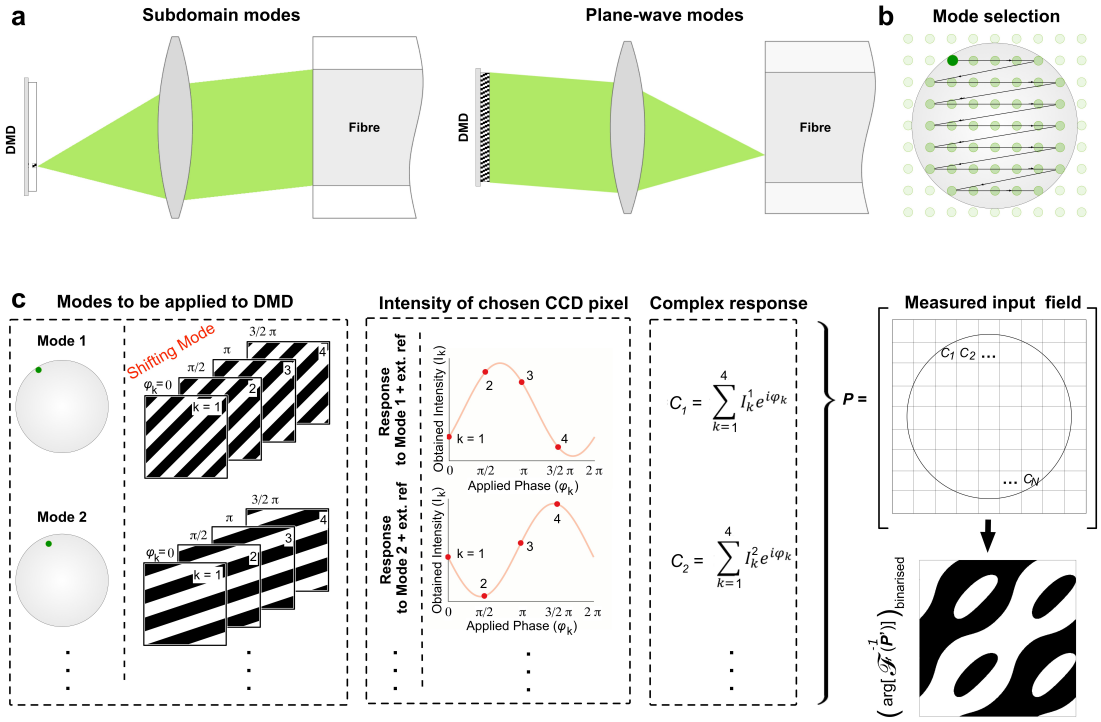

FIGURE 3.3: **Plane waves based wavefront shaping.** Truncated plane waves in the image plane of the modulator, generated by gratings applied to a whole surface of the SLM, are used as an alternative basis of input modes for TM measurements (**a**). Resulting in focal points in the far field, such modes could be employed for preliminary scanning of the fibre facet, selecting only the modes which are coupled into the core for further measurements (**b**). Following the same algorithm as for the subdomains-based procedure, the response for each of the selected modes could be obtained by analysing the response from the selected pixel of the CCD camera (**c**). Complex responses should be arranged in the Fourier domain (**P'**) around the first order, where the position of every response (complex value) defined by pitch (frequency) and direction of the grating applied to the corresponding mode. The Fourier transform of the arranged array (its phase) should be quantised to be applied to the SLM (e.g. binarised in the case of DMD).

through the fibre, defining the size of the basis of input modes for further calibration (see Fig. 3.3 b). Finally, the employment of the uniformly distributed external reference signal eliminates the effect of 'blind spots', resulting from the speckled nature of internal references [25]. We implemented this Fourier-based optimisation technique with both modulator types, and then compare their performance in the most relevant scheme for real applications in fibre-based endoscopy.

3.3 Ballistic regime: aberration correction in optical system

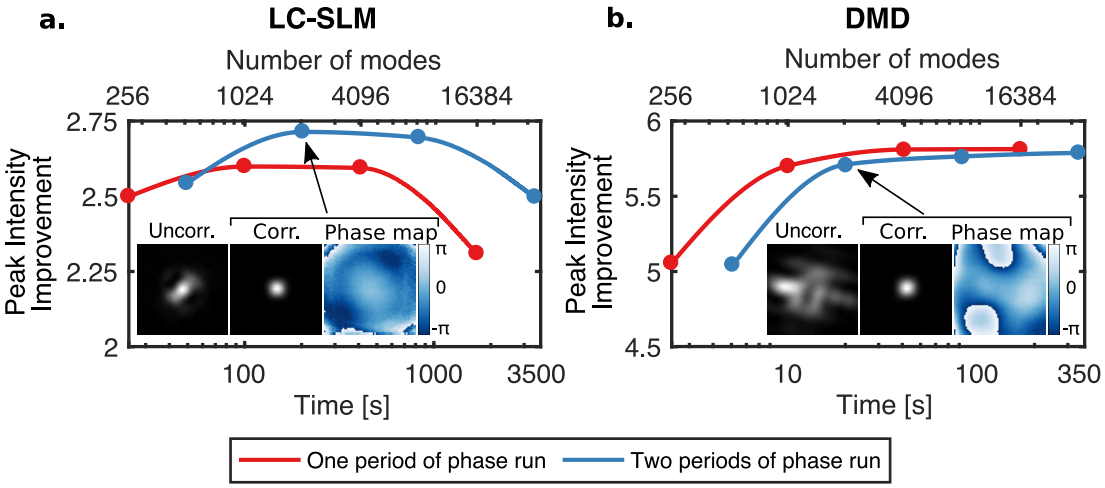

FIGURE 3.4: **Ballistic regime.** Peak intensity improvement in the focal spot as a function of optimisation time / number of spatial modes (subdomains) tested, using either an LC-SLM (a) or a DMD (b). Insets show a comparison of uncorrected and corrected focused spots, and the map of the measured phase aberrations in each case. Note that in this specific case the higher values reached using the DMD do not indicate its better performance, rather than much more severe starting conditions – significantly higher curvature of the modulator's surface. The spline interpolations are merely used as the guide for the eye. The relative standard deviations of the measurements have not exceeded 2%. As they are smaller than the markers, the error bars are not depicted.

SLMs offer a finite number of spatial degrees of freedom (equal to the number of independently controllable pixels), which dictates the extent to which the complexity of a given medium can be handled, and how efficiently the power of a propagating signal can be utilised. In the so-called ballistic regime, light signals do not deviate significantly from free-space propagation, with changes to propagating wavefronts being commonly described as single-plane phase aberrations. Such light transport can be described by very few propagating modes which can be fully controlled by SLM technology [18] and, in principle, all available optical power can be utilised.

Aberrations in optical systems corrupt a propagating wavefront and, in the focal plane, smear out the focus, decreasing its peak intensity. To assess the performance of the wavefront correction implemented with the use of both modulator types, we choose the improvement in peak intensity (ratio of peak intensities in the case of corrected and uncorrected wavefronts) as the relative figure of merit to indicate the quality of the focal spot. Figure 3.4 shows that varying the size of the subdomain in the wavefront correction algorithm (and

consequently altering the duration of the TM measurement procedure) results in a variation in the peak intensity improvement, when the measured correction is applied to create a single focal spot.

In the case of the LC-SLM (Fig. 3.4 a), the bottleneck limiting the time taken to sequentially optimise the phase of all subdomains is the modulator's refresh-rate of 40 Hz. Employing the DMD in place of the LC-SLM decreases the calibration time by a factor of 10. In our experiment, the bottleneck is now no longer the modulator itself (as the DMD can operate at up to 22 kHz), but is instead the camera, which can only operate at up to 400 Hz. In the case of either modulator, the main cause of the measured aberrations is the curvature of their surfaces. The insets of Fig. 3.4 a and 3.4 b show that, in this case, the surface of the DMD chip is significantly more curved than that of the LC-SLM. Nonetheless, the wavefront correction technique measures and corrects for these and any other aberrations present in the optical system.

Figure 3.4 shows that when using the LC-SLM, the peak intensity in the focal spot reaches a maximum value when using a correction based upon the measurement of 1024 spatial modes (i.e. a 32×32 grid of subdomains). Therefore, in our experiment, this resolution is high enough to accurately capture the majority of the aberrations in the system. However, when the number of spatial modes is increased to 16386 (i.e. a 128×128 grid, with each subdomain consisting of 4×4 LC-SLM pixels), the peak intensity found in the focus begins to fall below the maximum value. This can be understood by considering the strong scattering in liquid crystals: the portion of light diffracted from such a small subdomain is comparable to the amount of light that is scattered from the rest of the LC-SLM. This relatively strong background signal reduces the accuracy of the measurement of the optimum phase delay for each subdomain, and therefore begins to corrupt the overall wavefront correction.

In the case of the DMD, the peak intensity found in the focal spot also reaches a maximum after the measurement of 1024 spatial modes, at which point the performance of the system plateaus. As there is less randomly scattered light from the MEMS-based DMD in comparison with the LC-SLM case, further increasing the number of spatial modes does not improve or degrade the performance significantly.

We also tested another aspect of the wavefront correction technique - the effect of increasing the number of phase sweeps from one to two full cycles for each spatial mode measurement. In Fig. 3.4 these measurements are shown in red (one cycle phase sweep) and blue (two cycle phase sweep). In the case of the LC-SLM, increasing the number of phase sweep cycles from one to two

leads to an improvement in focal point peak intensity, although of course it also doubles the time taken to perform the measurements. The improvement in peak intensity is more pronounced for larger numbers of spatial modes (i.e. smaller subdomain regions). This behaviour implies that there is a random error in the measurements that is more significant for smaller sized subdomain regions and is reduced by averaging over a larger number of measurements. This random error may be due to the 'flicker' associated with LC-SLM operation: LC-SLM devices typically operate by cycling the polarity of the electric field across the liquid crystal layer. Therefore, even when the required pattern is not changed, a flicker effect can occur due to this continuous polarity switching, which periodically cycles the phase of each pixel by a small amount. Potentially, measurements with larger subdomains are less adversely affected by LC-SLM flicker, as they have more pixels over which the effect of flicker is averaged out. As expected, the lack of the flicker effect in the MEMS-based modulator results in no significant difference in peak intensity for one and two phase sweep cycles.

3.4 Highly-scattering regime: focusing through a ground glass diffuser

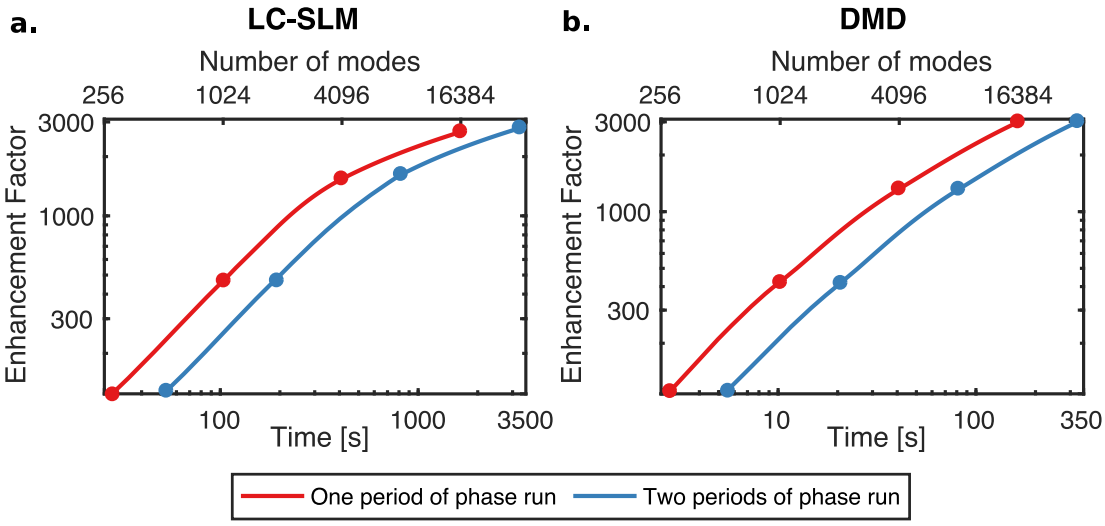

FIGURE 3.5: **Highly-scattering regime.** Enhancement factor (EF) as a function of optimisation time / number of spatial modes (subdomains) measured for either an LC-SLM (a) or a DMD (b). The relative standard deviations of the measurements have not exceeded 2%. As they are smaller than the markers, the error bars are not depicted.

In contrast to the balistic regime, highly-scattering (e.g. diffusive) media feature much larger number of allowed spatial modes than the number it is

possible to control with SLMs. In this case, only a small fraction of the propagating optical power can be controlled to generate diffraction-limited foci or other optical fields of interest [114].

For the diffusive regime, where the highly-scattering media transforms a coherent beam into a speckle pattern, applying the wavefront correction technique enables redistribution of light towards a chosen target point behind the diffuser. In order to investigate this scenario, the system is set up using module 2 (as shown in Fig. 3.1) which includes a ground glass diffuser at the Fourier plane of the SLM. In such a complex scattering media, the number of channels (i.e. possible separate routes of light propagation) is many times higher than the number of input spatial modes (i.e. subdomains) we can control via an SLM. Therefore, in addition to the chosen target focal spot, this situation also unavoidably leads to the formation of a diffuse background caused by the light we are unable to control. In this case, we use the ratio between the peak intensity at the target point and the average background level, referred to here as the enhancement factor (EF) as a comparison metric for this experiment.

Figure 3.5 shows the EF as a function of the number of sampled spatial modes for both the LC-SLM and the DMD modulator. Here, the values and trends are similar for both. As in the previous case, a measurement using two phase sweep cycles improves the performance for the LC-SLM as it suppresses the adverse effect of phase flicker.

For the demonstration of imaging through the complex media, the TM was obtained for 10,000 output points arranged in a square grid of 100x100 focal points. In Fig. 3.6, a negative USAF 1951 resolution target was imaged in a transmissive geometry, using a fast bucket photodetector placed behind the target. The detector triggered by DMD reference TTL pulses (one pulse for each switching between individual DMD modulations) allows obtaining the signal for each scanned position, which being rearranged into a 2D array form an image.

3.5 Intermediate regime: focusing through a multimode fibre

Light transmission through a multimode optical fibre could be considered as a boundary case between the two above mentioned extremes of ballistic and highly-scattering regimes. Here, the number of allowed propagating modes

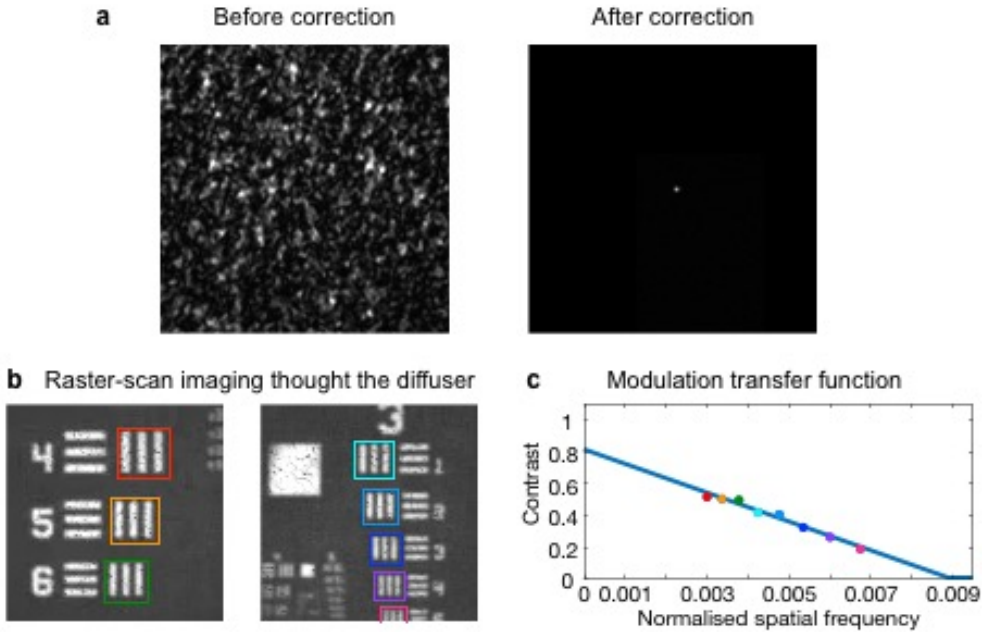

FIGURE 3.6: Focusing (a) and imaging (b) trought the ground-glass diffuser. Imaging contrast as a function of the normalised spatial frequency for the target elements in (b), and the fit of the modulation transfer function (MTF) corresponding to an aberration-free imaging system with a square aperture. The fit allows for the estimation of the effective numerical aperture (NA) as 0.0089 ± 0.0006, and the corresponding resolution limit (Abbe criterion) as $29.9 \pm 2.1\ \mu$m.

in the system is of the same order as the number of degrees of freedom controllable by SLMs. The capability of MMFs to deliver almost all of the coupled light to the distal facet is one of the reasons that makes them a very promising technology for micro-endoscopy, in particular because the same MMF can then collect the reflected or fluorescently excited light.

In order to compare the performance of the modulators in this case, we use the ratio between the power in the focal spot compared to the full output power emitted from the fibre as a performance metric. Using this power ratio (PR) allows us to roughly estimate a percentage of power contributing to a signal and the one forming the background in the intended application.

3.5.1 Subdomain-based optimisation

The optical setup was as shown in module 3 of Fig. 3.1 and, in this experiment, we probed the TM in the subdomain basis. Figure 3.7 a shows that, in the case of both modulators, the PR starts to reach saturation after the measurement of about 4000 spatial modes. However, the PR in the case of the DMD-based system is 10-15% higher for each point on the plot. We believe this is once

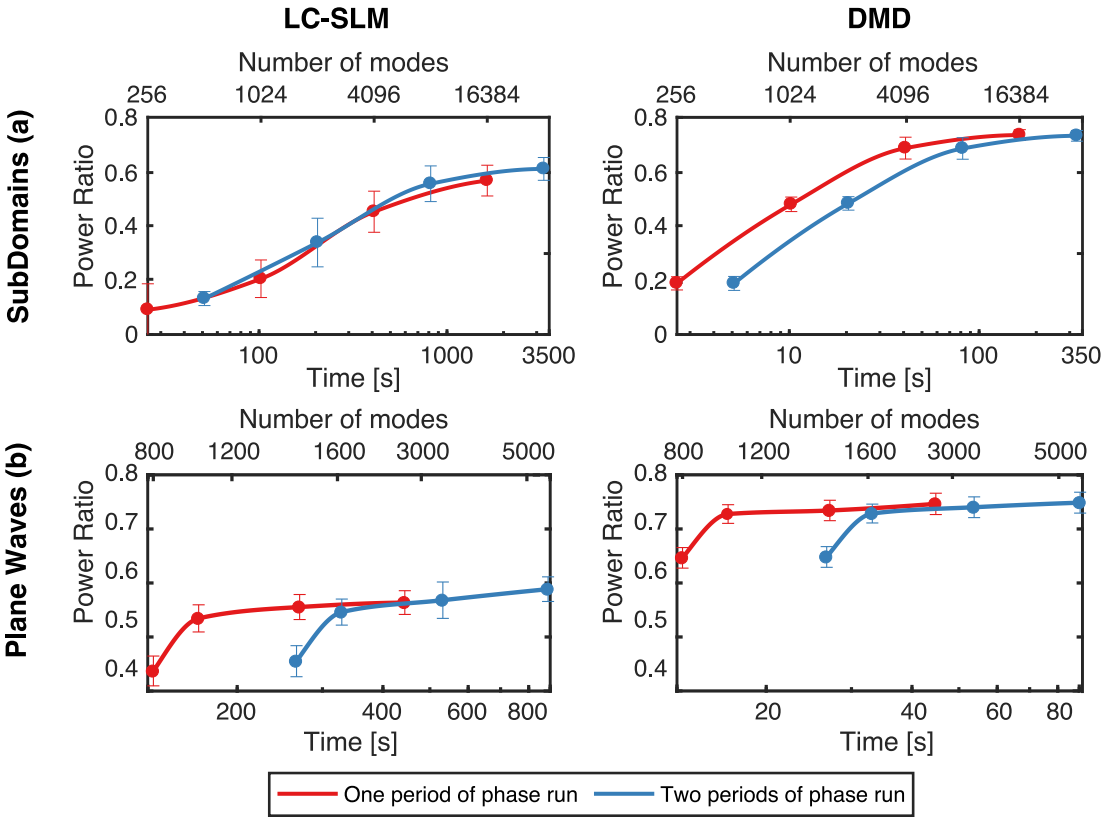

FIGURE 3.7: **Intermediate regime: Multimode fibre.** Power ratio as a function of optimisation time for both subdomain (a) and Fourier-domain (b) approaches, for either an LC-SLM of a DMD. The error bars have been calculated from three sequential runs of the experimental procedure (measurements of TM) and 7×7 diffraction-limited foci generated across an orthogonal grid at the output facet of the MMF.

again due to the detrimental effects of the strong scattering from liquid crystals in the case of the LC-based modulator, which are not present when using a DMD. During every measurement, and when applying a pre-shaped correction wavefront, a portion of this uncontrollably scattered light within the acceptance angle of the fibre propagates towards the distal end and creates an uncontrollable background. We note that it was impossible to directly observe this effect, dealing with normalised values in the first experiment or in the second experiment, where only a small portion of light reflected off the SLM reaches the sensor of the camera. As an additional test on raster-scan imaging, and demonstration of DMD high-speed operation, we chose a negative USAF 1951 resolution target as the imaging object, which was placed in proximity to the distal end of the fibre. The transmitted light is detected by a fast avalanche photodetector placed behind the resolution target. Figure 3.8 presents an exemplary 10 seconds long imaging session performed with a DMD running at a 20 kHz refresh rate. The same 10 seconds session performed on LC-SLM based system is depicted for comparison.

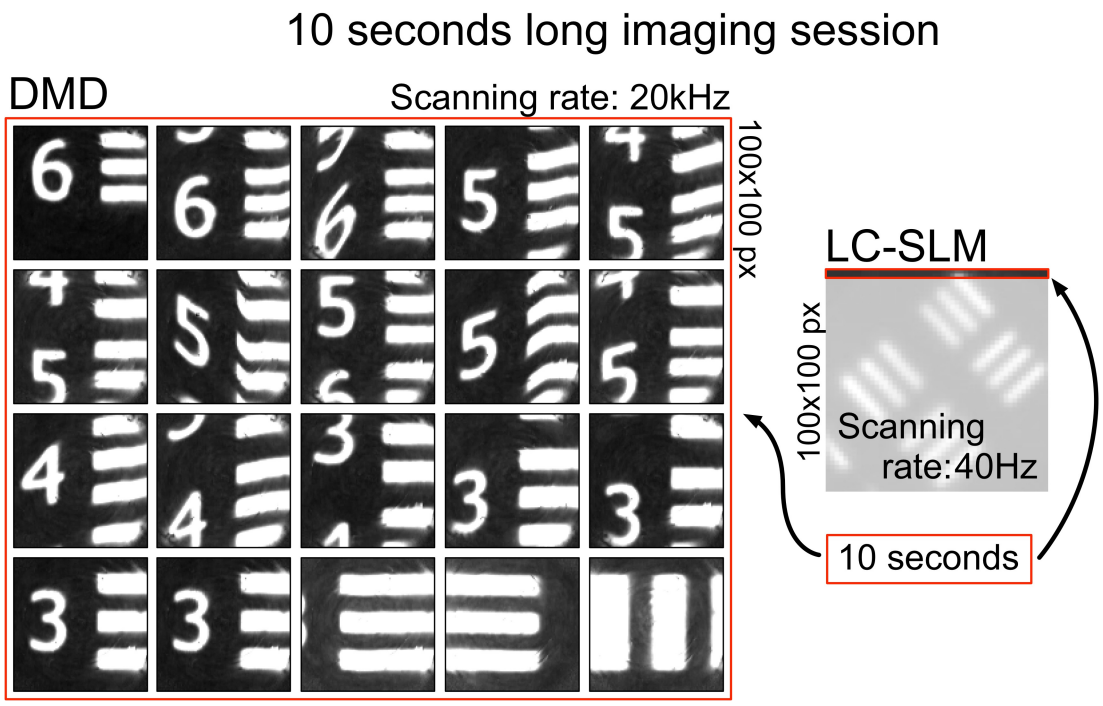

FIGURE 3.8: **Imaging speed comparison.** Imaging of USAF test target performed on both DMD and LC-SLM based fibre imaging systems. During at 10s session, the DMD based system allowed for the acquisition of 20 full images (100×100 pixels each) of the dynamic scene(moving test target). The session of the same length was performed on an SLM based system and resulted in the acquisition of only 4% of a single frame (static scene).

3.5.2 Fourier-domain based optimisation

Figure 3.7 b shows the performance of the Fourier domain-based optimisation for the two modulators. For our fibre with 0.22 NA and the core diameter of 50 µm, the PR trend plateaus upon the measurement of about 1000 input modes, which coincides with the number of waveguide modes in the fibre per one polarisation state for the given wavelength (≈1000 according to a large V-number approximation). This plateau in PR is reached in approximately one tenth of the time required for the subdomain-based optimisation procedure. Moreover, this improvement in calibration speed does not compromise the performance: maximum PR values are equivalent using either probe basis.

As observed with subdomain-based optimisation, using the Fourier-based optimisation the DMD produces foci at the distal end of the MMF with PR values of up to 15% higher than those generated using an LC-SLM. This is because, despite higher SNR at the measurement stage, the LC-SLM still suffers from a portion of uncontrolled scattered light propagating through the fibre, thus reducing the PR level.

3.6 Conclusions

While LC-SLMs have been the standard choice in wavefront-shaping applications for over a decade, and are currently the most frequent choice in complex photonics applications, MEMS-based DMD alternatives have started to gain popularity in the last few years. DMDs are usually chosen because of their faster modulation rates, at the cost of their overall optical efficiency.

Our work shows that, despite this reduced efficiency, DMDs may outperform LC-SLMs, not only in modulation rate, but importantly, also in beam shaping fidelity. We have shown that when optimising light transport through complex media, DMD displays have higher beam shaping fidelity regardless of the complexity of the scattering medium. The apparent reason for this superior fidelity is that DMDs do not suffer from the strong scattering present in LC-SLMs, which corrupts the optimisation procedure and contributes to an uncontrollable background signal. This is especially crucial when focusing light through MMFs, where we have observed that an LC-SLM based system can achieve a power ratio of 60% at the target focal point, while a DMD based system operating in an identical regime reached a power ratio of 75%. In potential applications of this technology to imaging, this translates directly to improvements in image contrast. Another inherent drawback of LC-SLMs is their

phase flicker, which decreases the precision of phase measurements in optimisation procedures. Although this effect can be averaged out by increasing the number of obtained samples for each mode, it results in a longer calibration time.

We note that in our experiments, although the DMD has a refresh rate of 22 kHz, we were unable to reach such values due to the limited frame rate of our camera. In this work, we also demonstrated that when characterising a multimode fibre, using the Fourier-domain based optimisation procedure in place of the subdomain-based approach can decrease the characterisation time by one order of magnitude.

Finally, we emphasise that the diffraction efficiency in the case of the DMD was only 8%, in contrast to 42% for the case of LC-SLM. In many applications this can be compensated for by increasing the power of the laser source; there are, however, cases where the photon budget cannot be compromised and the advantages of DMDs would not trade-off well. One of the examples of power demanding application - optical tweezer is shown in the Chapter 5.

This work, therefore, highlights the importance of careful consideration of parameters in order to reach the optimal balance between speed and performance in wavefront shaping experiments, including several less-recognised differences between LC and MEMS based spatial light modulators.

Chapter 4

Multimode fibre based endoscopy for deep-brain imaging

The previous chapters walked the reader through the ways of amplitude grating based complex modulation, implementation of the best practices of beam-shaping through multimode fibres on DMD, and evaluation of its performance in comparison with LC-SLMs. All these works, step-by-step, were bringing the group closer to the main goal of proving the relevance of the multimode fibre based imaging for biomedical applications.

The present chapter shows a compact and high-speed imaging system capable of resolving micro-sized neural cells in an anaesthetised animal model through, to my knowledge, the most minimally-invasive endoscopic probe. Built upon the high-performance holographic methods fitted to a DMD, as well as carefully optimised design, the system is capable of artefact-free imaging of both neuronal somata and dendritic processes deep inside brain tissues, with diffraction limited resolution. The resolution limits are dictated only by the numerical aperture (NA) of the fibre probe, and the speckle background level is reduced to the theoretical limit.

This work is one of the first steps in moving multimode fibre based systems from imaging of static targets and fixed samples, towards dynamic and challenging environments of living animal tissues.

Related paper:
Turtaev, S., *Leite, I. T., Altwegg-Boussac, T., Pakan, J. M., Rochefort, N. L., & Čižmár, T. "High-fidelity multimode fibre-based endoscopy for deep-brain in vivo imaging." arXiv preprint arXiv:1806.01654,* ***2018****.*

The contributions from the author of this thesis to the work presented in this chapter consisted of: (i) implementation of compact system design, (ii)

implementation of the holographic methods for MMF based imaging, (iii) fibre probe preparation and post-processing, (iv) assistance in *in-vivo* experiments.

Despite the experience in holographic beam-shaping through fibres acquired by the group over a long period, and almost two years of own research, this work would never be possible without the involvement of skilled specialists with research activities in the discipline of in vivo imaging. Our collaborators, the group of Dr Nathalie Rochefort of the University of Edinburgh, not only conducted the experiments with animals, but also helped to optimise our experimental design for the in vivo implementation.

4.1 Experimental setup

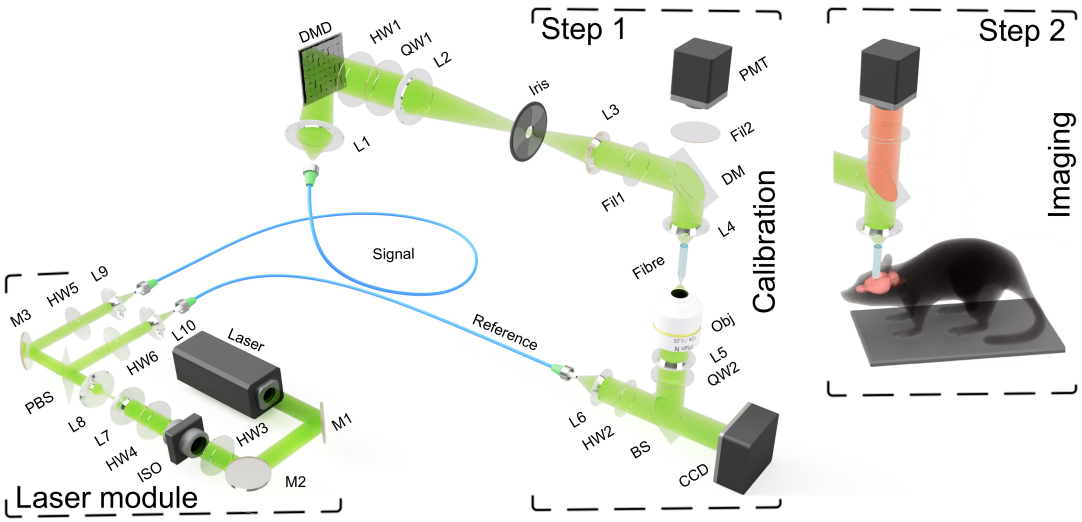

FIGURE 4.1: Scheme of multimode fibre based imaging system. The calibration (step 1) consist of obtaining the TM using the calibration module, computing approximately 7000 phase modulation patterns for all desired foci across a 50 μm-wide circular region of the focal plane, and finally uploading the patterns to the memory of the DMD device.

As illustrated in Fig. 4.1, the system is designed in a modular manner, consisting of a laser, calibration, beam-shaping and sample modules. In the laser module, the beam is divided into a signal and a reference beam, which are coupled to single-mode polarisation-maintaining fibres. The calibration module is used for measuring the transmission matrix of the multimode fibre, and is subsequently replaced by a sample module for the anaesthetised animal.

Laser module. A single-frequency, diode-pumped solid-state laser source emitting at the 532 nm wavelength provides a continuous-wave and linearly polarised beam. Achromatic doublets L7 and L8 form a telescope to demagnify the beam, and aspheric lenses L9 and L10 couple the signal and

reference beams into the polarisation-maintaining fibres. Half-wave plate HW3, in combination with the input linear polariser of the Faraday optical isolator ISO, controls the combined power coupled to the signal and reference beams, whereas a half-wave plate HW4, in combination with polarising beam splitter PBS, controls the power ratio between the signal and reference beams. Half-wave plates HW5 and HW6 are used to finely align the polarisation of the coupled beams with one of the birefringent axis of the polarisation-maintaining fibres (Fig. 4.1).

Beam-shaping module. Achromatic doublet L1 collimates and expands the signal beam to overfill the DMD at an incidence angle of 24° with respect to the DMD chip. In this way, each micro-mirror in the 'on' state (+12°) reflects light in the direction of the optical system, whereas micro-mirrors in the 'off' state (-12°) redirect light towards a beam dump. Lenses L2, L3, and L4 relay the far-field of the first diffraction order of the holograms generated at the DMD to the proximal facet of the multimode fibre. An iris diaphragm is used in the Fourier plane of L2 to isolate the first diffraction order of the holograms, while blocking the remaining orders. The combination of lenses L2 and L3 is chosen to underfill the aperture of aspheric lens L4 in order to reduce its effective numerical aperture down to 0.23, matching that from the multimode fibre. The multimode fibre used has a core diameter of 50 μm and a 0.22 NA, and at the 532 nm wavelength sustains approximately 2100 propagation-invariant modes (i.e. 1050 for each orthogonal polarisation state). Circular polarisation is well preserved after propagation through a straight fibre segment. The transmission matrix is measured between 3000 input modes and 7000 output modes (corresponding to the desired foci). Oversampling is essential to reach the highest fraction of the optical power contained in a focused spot. Dichroic mirror DM, together with excitation filter Fil1, and emission filter Fil2, separate and spectrally purify the fluorescence signal. A photomultiplier tube PMT measures the overall intensity of the fluorescence signal. A half-wave plate HW1 and a quarter-wave plate QW1 provide the two degrees of freedom necessary to reach the purest circular polarisation state of the spatially-modulated signal at the input facet of the fibre.

Calibration module. A movable, size-compact calibration module is used to acquire the TM of the fibre prior to the image acquisition. The TM is measured interferometrically using an external phase reference. Being uniformly distributed, the external reference prevents the formation of 'blind spots'

originating from the speckled nature of internal references. A microscope objective Obj in combination with a tube lens L5 image the selected focal plane (spatially offset away from the fibre facet) onto the CCD camera with 27.7× demagnification. The reference beam is collimated by aspheric lens L6 and combined with the signal beam using non-polarising beamsplitter cube BS. A quarter-wave plate QW2 converts the polarisation state of the output speckle patterns to linear, and a half-wave plate HW2 aligns the polarisation axis of the reference signal in order to maximise the signal-to-noise ratio of the interference patterns at the camera. The microscope objective is mounted on a single-axis translation stage for precise focusing and displacement of the calibration plane with respect to the output fibre endface.

Sample stage. The in vivo imaging stage was placed below the fibre and consisted of a custom made frame with ear-bars, to keep the animal's head position fixed during the imaging procedure, and a fitted face mask for delivery of isoflurane anaesthesia. Suitable body temperature was maintained via thermal bandage. The sample stage was mounted on a three-axis motorised translation stage with servo-driven actuators (ThorLabs, USA), allowing precise positioning of the animal both laterally, for targeting the craniotomy, and axially, for the control of the fibre penetration process.

As shown on the photograph (Fig. 4.2), the beam-shaping part of the system was detached from the laser module, using polarisation maintaining fibres, and all its components were embedded in a robust single-cage based construction, resulting in a stable operation, spanning several hours without the need for recalibration.

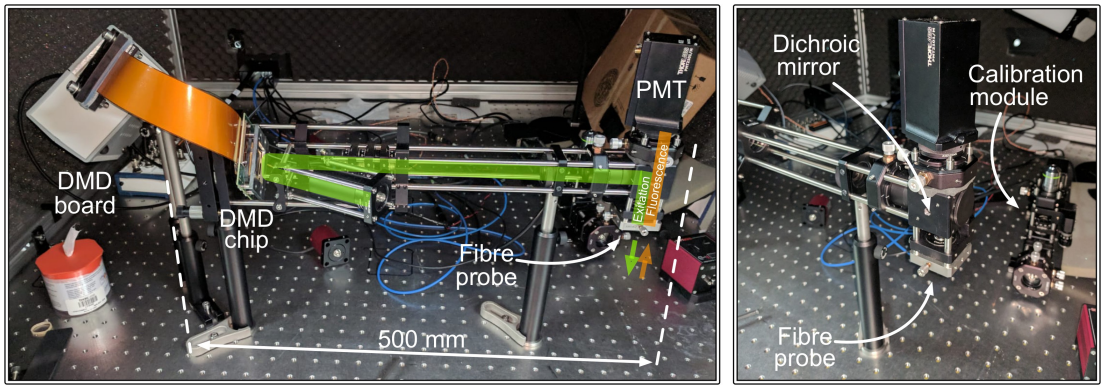

FIGURE 4.2: Photo of the beam-shaping and calibration modules.

4.2 Fibre probe

A standard commercially available MMF (Thorlabs FG050UGA) with a core of 50 μm in diameter and a NA of 0.22 was chosen as the endoscopic probe. It is important to note that this particular fibre model was used in the previous experiment.

In order to minimise the tissue damage caused by the compression during the penetration process [115, 116] the fibre probe was post-processed into a flat-cone termination by polishing out the excess of cladding from 125 μm down to 60 μm external diameter, as depicted in Fig. 4.3 a. In order to shape the tip in the desired way, the fibres were held by a fibre clamp (Thorlabs SM1F1-250), fixed onto a stepper motor allowing for rotation ($\sim$5 rpm) around their axis. An xy translation mount (Thorlabs CXY1) was used for the fine adjustment to correct for eccentricity in the rotation. A fibre polishing sheet (Thorlabs LF3D) has been cut into the shape of a circle with a diameter of 4 cm and fixed onto a fast-rotating stage ($\sim$500 rpm). The sheet is then brought into contact with the fibre at a grazing angle ($\sim 5^\circ$) to polish out the cladding. A low-magnification microscope objective, together with a tube lens and a CCD camera, was used to monitor the progress.

Figure 4.3 c shows the photograph of a typical fibre probe, which was used for in vivo experiments. It consisted of a flat-top terminated 2 cm long fibre piece, glued inside the ceramic ferrule, allowing the probe to be stably held in the system as well as swiftly replaced with the new one between the experiments. The fibre length, as well as its position inside the ferrule, were kept constant with <1 mm precision across the whole batch of probes prepared for in vivo experiments. This allowed for a significant reduction in time for replacement of the probes (down to 2-5 min, indicated in Fig. 4.5), mainly due to minimising required corrections in the alignment. At the output side of the ferrule the fibre is embedded in a big drop of index-matched UV-curable glue covered with black absorbing paint. This simple solution allows for a sufficient suppression of the cladding modes, preventing them from reaching a distal end of the fibre and contributing to the output field.

The working distance of the fibre as an imaging element is another important parameter, which is defined by the optical properties of the fibre. Focusing ability, as well as collection efficiency of fluorescent signal, depends on the NA of the probe as well as on the distance between the fibre facet and the focal plane. As depicted the Fig. 4.3 b, maximum effective NA can be reached only in a limited volume behind the fibre facet, forming an emittance/acceptance

cone, whose height is limited by the NA of the fibre and the radius of the core (r), being defined to the distance of $r\cot(\arcsin(NA)) \approx r\,NA \approx 110\mu$m. In all experiments of this study, we offset the focal plane 5-15 μm away from the distal end of the fibre, to guarantee reaching the full NA of the fibre uniformly across the field of view and minimise sample-induced aberrations.

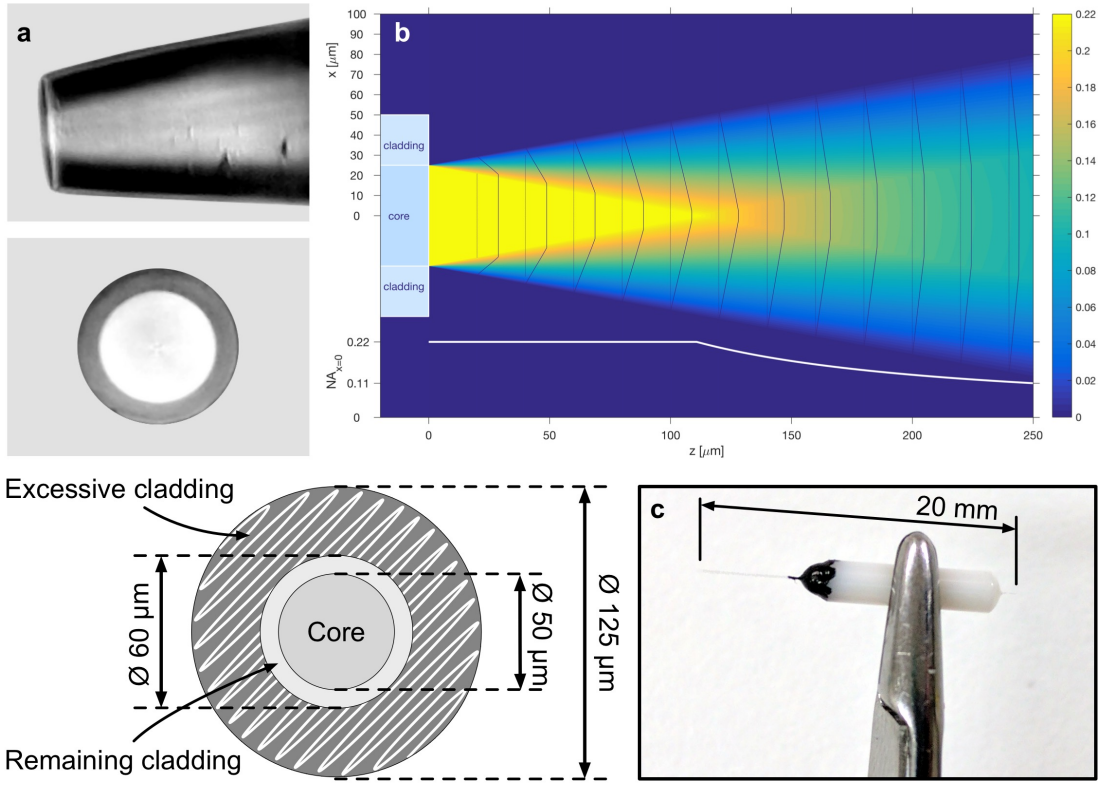

FIGURE 4.3: **a**. Flat-top termination of the MMF probe with a 50 μm core diameter and a 60 μm external diameter. **b**. Map of numerical aperture vs distances from the output fibre facet. The lower plot shows the evolution of the NA along the optical axis, and the series of transverse dark lines illustrate the NA profiles across different axial planes in front of the fibre. **c**. Photo of typical fibre probe, prepared for in vivo experiments.

4.3 Calibration methods

The digital micromirror device in the heart of our system is employed in the off-axis regime, as explained in the Chapter 2, allowing to control the phase of the optical fields coupled into the fibre. Detailed in Chapter 3, principals help analysing the system response at the distal end of the fibre to a set of predefined optical fields (input modes) generated by the DMD. The basis of input modes consists of truncated plane-waves of varying k-vectors. At the Fourier plane (focal plane of lens L2, iris in Fig. 4.1), as well as at the input

fibre facet, this basis corresponds to a square grid of 65×65 focused spots. A preliminary step measures the transmitted intensity by integrating the output speckle imaged by the CCD detector, for each input mode. This allows reducing the number of input modes to $\sim$3000, since only those which are incident on the fibre core are effectively coupled. The basis of output modes consists of a square grid of 100×100 points spaced by approximately $0.5\,\mu$m across the focal plane (i.e. at a certain working distance from the output fibre facet), which are conjugated to pixels of the CCD detector. Only $\sim$7000 of these output modes fall within the $50\,\mu$m diameter circular area. The interferometric response to each input mode, recorded at every output mode, allows characterising the light propagation through the whole optical path and forming the TM. The TM natively accounts for all the aberrations in the optical system and allows calculating phase modulations which, when applied to the DMD, results in the formation of a diffraction limited foci at any desired location across the focal plane.

Due to the high refreshing rate, the USB-3 data interface of DMD, and parallel computing, the whole calibration procedure (including obtaining the TM, computing the output modes, and uploading corresponding patterns to the memory of DMD module) takes about 2 minutes (indicated in Fig. 4.5). Once this (calibration) procedure is finished, the calibration module is removed, and the system is ready for imaging.

4.4 Performance evaluation

The fidelity of the synthetised foci is a crucially important attribute to reach the highest possible quality of imaging. In MMFs, as well as in all cases when light propagation through a randomising medium is controlled, only a fraction of the optical power leaving the medium can be directed into the diffraction-limited focus. The remaining optical power forms a background signal in the form of a speckle, observable in Fig. 4.4 a. The speckled background does not affect the resulting image significantly when observing very sparse and high-contrast scenes (e.g. a few fluorescent particles in the field of view), however, it manifests itself as a glare background reducing image contrast in the case of dense, volumetric samples.

Introduced previously, the ratio between the power in the focal spot and the total output power emitted from the fibre is commonly used as a figure-of-merit when assessing the performance of a given optimisation approach. Working in the off-axis regime and utilising circularly polarised light has been

shown in the section 3.5 to reach 75% of optical power stored in the desired focus, which is very close to the theoretical limit for the phase-only modulation based approaches [53]. Although more suited for turbid media where, in contrast to MMFs, the total transmitted power is not accessible, the enhancement previously mentioned in section 3.4 is frequently employed as a quality metric. This parameter, defined as the ratio of the peak intensity on the focal point to the average level of speckled background, exceeded 3100 in our experiments.

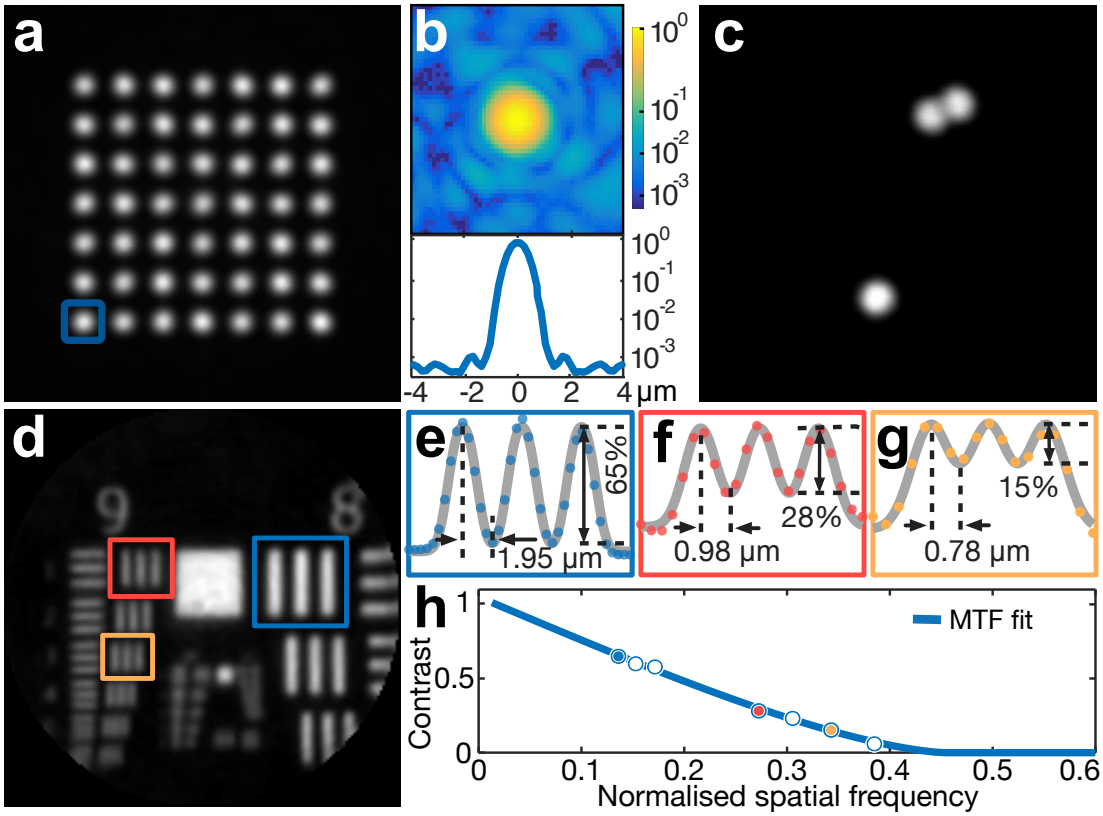

FIGURE 4.4: **Performance evaluation MMF based system for in vivo experiments. a**. Combined foci (sum projection) at the distal MMF facet demonstrating the power uniformity of focusing at different locations. **b**. Intensity distribution and its azimuthally-averaged profile of the chosen focal point (indicated by a blue square on panel a) in logarithmic scale. **c**. Validation of fluorescent imaging using 4 μm fluorescent particles. **d-h**. Assessment of spatial resolution using a negative USAF-1951 test target. Image of the test target **d** and contrast measurements of the selected target elements of 265 line pairs per millimetre (lp/mm) **e**, 512 lp/mm **f**, and 645.1 lp/mm **g**. (h) Imaging contrast as a function of the normalised spatial frequency for the target elements in **d**, and the fit of the modulation transfer function (MTF) corresponding to an aberration-free imaging system with a circular aperture. The fit allows for the estimation of the effective numerical aperture (NA) as 0.225 ± 0.008, and the corresponding resolution limit (Abbe criterion) as 1.18 ± 0.04 μm.

A fast bucket intensity detector being triggered by DMD reference TTL pulses (in a synchronous manner with switching between individual DMD modulations) allows operating the system with a refresh rate of almost 23 kHz,

which results in an imaging rate of 3.5 frames per second. The system has been devised with a robust cage based construction, resulting in a stable operation spanning several hours without the need for recalibration. The optical path was designed to achieve the maximum resolving power of the MMF. The resolution of the demonstrated fibre based system has been assessed via a negative USAF 1951 test target placed in proximity to the distal end of the fibre. As shown in Fig. 4.4 b, the separation of 4 μm and 1.9 μm between the lines could be imaged with contrasts of 85% and 30%, respectively, which is in good agreement with the resolution limit (Rayleigh criterion) for the NA of the fibre and the wavelength used.

For validation of operation in the fluorescent regime (Fig. 4.4 f), we used 4.0 μm, red fluorescent beads that have been placed on a microscope slide. Emitted fluorescent light from the sample is collected and delivered back to the imaging system by the same fibre, where it is spectrally isolated from the excitation signal by a dichroic mirror and directed towards a photomultiplier tube.

4.5 Deep-brain imaging in vivo

4.5.1 In vivo implementation of an MMF based system.

Figure 4.5 outlines the experiment of in vivo implementation of an MMF based imaging system. During preparations for in vivo experiments, significant attention was brought to practical applicability and operational simplicity of the system, avoiding any delays and allowing collaborators to perform the experiment with minimal guidance. A special calibration procedure, which is not required for conventional Fourier optics based imaging systems, was extensively optimised. The set of constructional solutions for fast replacement of the probe, special procedures for probes preparation, keeping the geometry almost identical to minimise alignment time, and parallelised computing of the patterns for output modes, allowed reaching reasonable delay times (of about 10 minutes) between experiments.

For the demonstration of in vivo imaging capability deep within the brain of an anaesthetised animal, we used transgenic mice with a subpopulation of inhibitory interneurons labelled with a red fluorescent marker (tdTomato; see Materials and methods). The insertion of the fibre endoscopic probe into the primary visual cortex (V1) and deeper into the hippocampus of the mouse brain was made through a small craniotomy. The images presented

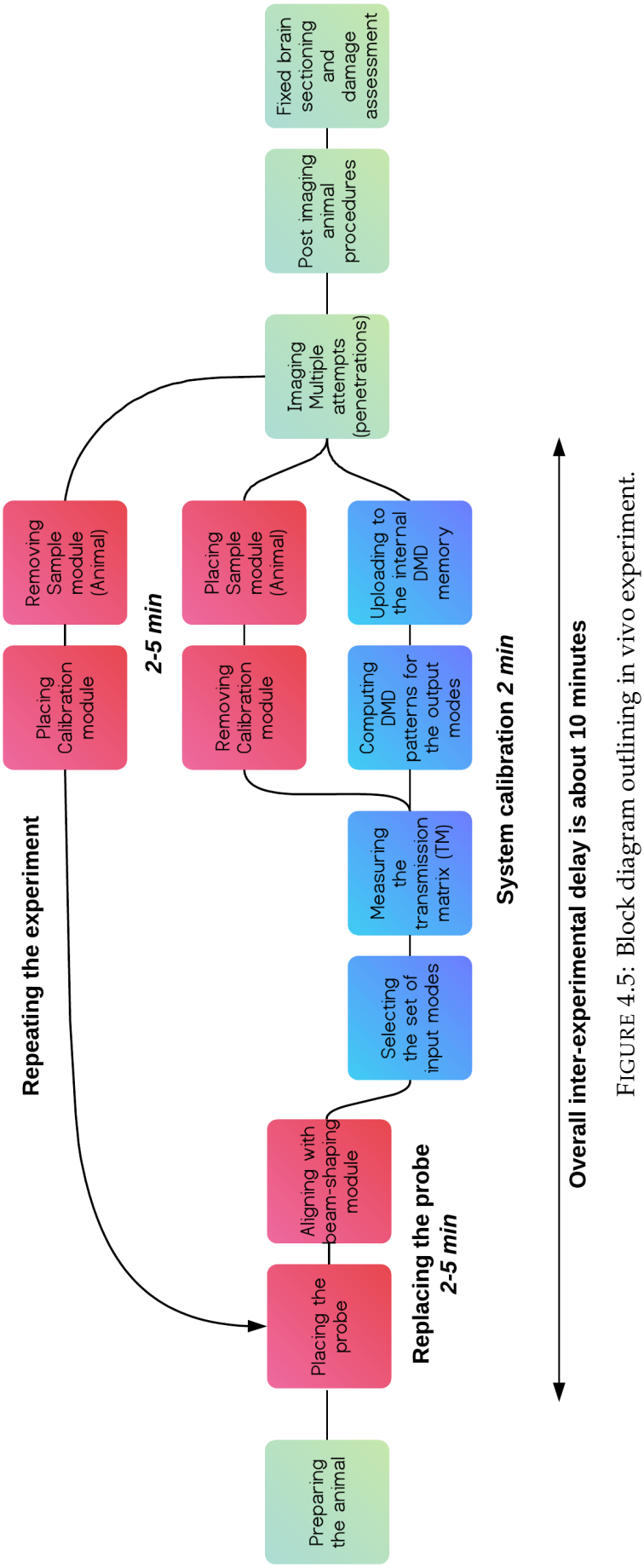

FIGURE 4.5: Block diagram outlining in vivo experiment.

in Fig. 4.6 a,b were recorded at different depths within V1 (0.5-0.8 mm), and in the CA1 region and dentate gyrus of the hippocampus (approximately 1.5 and 2 mm). In order to visually assess the damage caused by insertion of the probe, post-mortem section of the perfused brain after fibre imaging was performed. As demonstrated in Fig. 4.6 d the fibre tract width does not exceed 50 μm. However, taking into account the size of the fibre probe (125 um), it means that the surrounding tissue was compressed during the penetration process. Induced fractional volume displacement may cause a damage of neuronal processes, rupture of small vessels and associated disruption of neuronal activity [99, 117–119]. An assessment of the tissue damage was not the main aim of the current study, but will be addressed in the future works. The resolution and contrast achieved in vivo allow for the visual identification of both relatively large objects, such as cell soma (diameter around 10-20 μm, see Fig. 4.6 a), and thin processes (usually 1-2 μm wide) with fine structures, corresponding to synaptic boutons (see Fig. 4.6 b). It is important to notice that the achieved frame rate, which is higher than breathing rate of the animal,

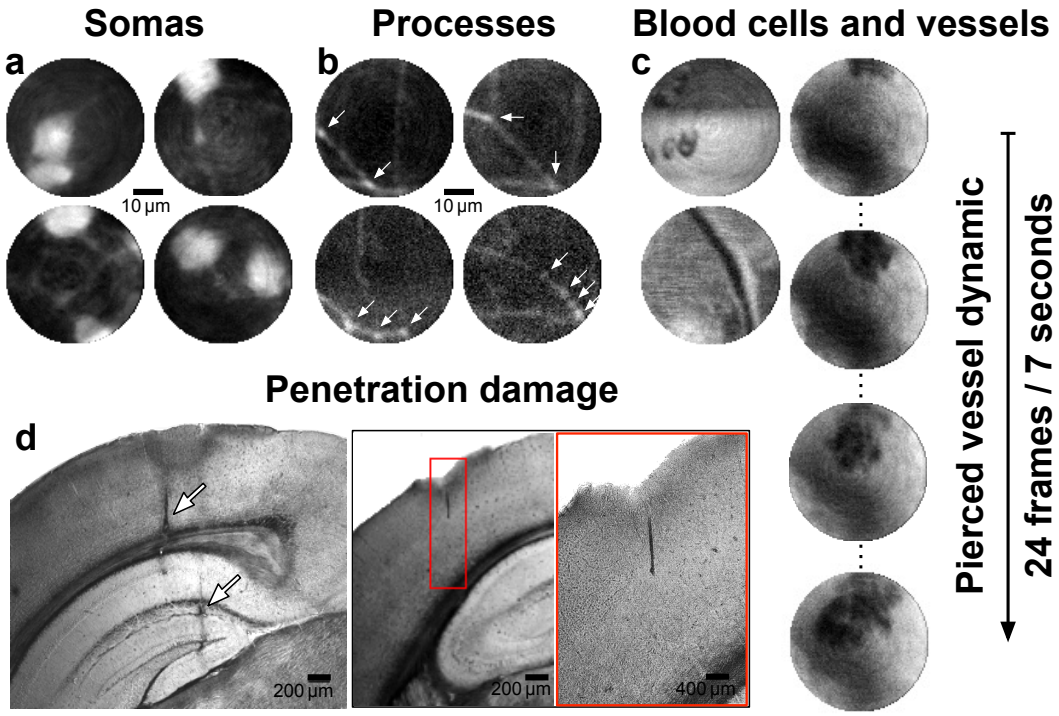

FIGURE 4.6: **In vivo implementation of MMF based system.** Images of somata (**a**) and processes (**b**) of inhibitory neurons observed via direct insertion of the MMF probe up to 2 mm deep into a mouse brain. Arrows indicate branching points and synaptic boutons. **c.** Imaged via out-of-focus light non-labelled objects as blood vessels and blood cells, as well as record bleeding caused by penetration of fibre probe. **d.** Post-mortem coronal brain section showing fibre tracts of the MMF probe in the visual cortex and in the hippocampus. The width of each tract is less than 50 μm.

allows avoiding distortion of the images as well as any related post-imaging corrections.

In contrast to the above-presented experiments with beads, in vivo images are affected by fluorescent background, which is usual for low-NA epifluorescent imaging and could be reduced by utilising higher NA fibre probes, implementing advanced techniques (e.g. multiphoton imaging) or optimising labelling density. Moreover, relatively strong out-of-focus signal in close proximity to labeled cells led to the capture of images of non-labelled objects such as blood vessels and blood cells, as well as record insignificant, but unavoidable bleeding caused by penetration of the fibre probe (see Fig. 4.6 c).

Another important feature of holographic imaging is the ability to scan across different focal planes while retaining the position of the fibre probe. This can be done by repeating the calibration procedure for different axial positions of the objective in the calibration module. Such technique allows to observe the dynamic of axially displaced objects, which otherwise would require constant moving of the probe from plane to plane and cause further tissue damage. In this work, such ability was demonstrated (see Fig. 4.7), however not fully utilised, mostly because of the relatively low labelling density ($\sim$1 labeled cell per $50 \times 50 \times 50\,\mu$m volume), which was chosen in order to avoid image contamination by strong out-of-focus light.

4.5.2 Materials and methods

Animals

Data were acquired from 5 adult mice (5-6 months old). In 4 mice, a subpopulation of inhibitory neurons, Somatostatin-expressing (SST) neurons, was labelled with a red fluorescent marker (tdTomato) using a Cre-driver transgenic mouse line: Sst<tm2.1(cre)Zjh> (SST-Cre) [RRID: IMSR_JAX: 013044] (Jackson Laboratory, ME, USA) cross-bred with Rosa-CAG-LSL-tdTomato [RRID: IMSR_JAX: 007914] mice. In one mouse, another subpopulation of inhibitory neurons, (VIP) neurons, was labelled with the same red fluorescent marker (tdTomato) using a Cre-driver transgenic mouse line: Vip<tm1(cre)Zjh> (VIP-Cre) [RRID: IMSR_JAX: 010908] (Jackson Laboratory, ME, USA) cross-bred with Rosa-CAG-LSL-tdTomato [RRID: IMSR_JAX: 007914] mice. The animals were group housed (typically 2-4 mice), and both male and female mice were used for the experiments. All procedures were approved by the University of Edinburgh animal welfare committee and were performed under a UK Home Office project license.

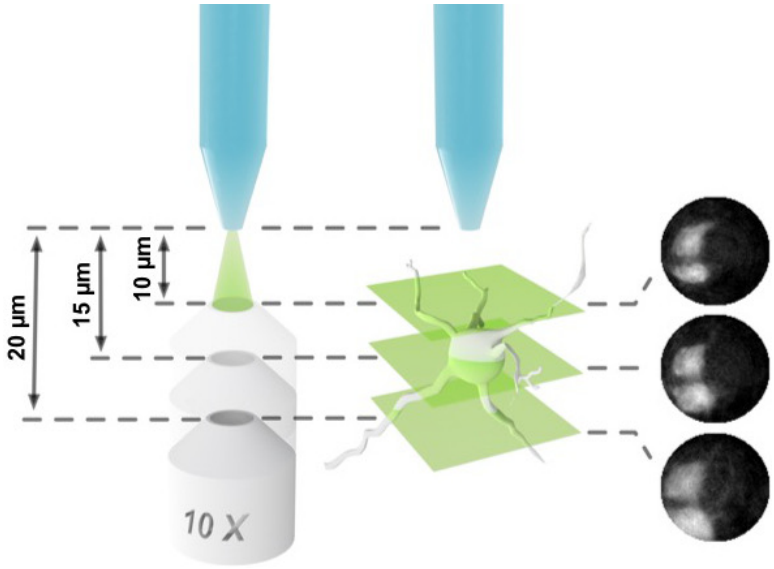

FIGURE 4.7: Fluorescence imaging can be performed at multiple depths from the front facet of the fibre, by calibrating the system to different focal planes. The generated patterns were displayed on DMD consecnitly, resulting in an aquisition rate of a full stack (3 images) in less than a second. The chosen focal planes were ofset by 10, 15 and 20 μm from the distal fibre facet, to guarantee that the full NA of the fibre was reached uniformly across the field of view (see Fig. 4.3) and to minimise sample-induced aberrations.

Surgical procedures

For craniotomy, mice were anaesthetised with isoflurane (4% for induction and 1-2% maintenance during surgery and throughout imaging) and mounted on a stereotaxic frame (David Kopf Instruments, CA, USA). Eye cream was applied to protect the eyes (Bepanthen, Bayer, Germany), analgesics and anti-inflammatory drugs were injected subcutaneously (Vetergesic, buprenorphine, 0.1 mg/kg of body weight, carprofen, 0.15 mg, and dexamethasone, 2 μg). A section of scalp was removed, and the underlying bone was cleaned before a craniotomy (around 2×2 mm) was made over the left primary visual cortex (V1, 2.5 mm lateral and 0.5 mm anterior to lambda). Cyanoacrylate glue (Locktite, UK) was applied to the surrounding skull, muscle, and wound margins to prevent further bleeding.

Imaging procedure

The animal was fixed on a sample module using ear-bars and wore a face mask for the delivery of isoflurane anaesthesia (1-2%). Suitable body temperature was maintained via thermal bandage. The automotised translation stages of

imaging sample stage were used for targeting the craniotomy and for the controlling of the fibre penetration process. The endoscopic fibre probe was gradually lowered into the craniotomy, up to 1-4 mm into the brain tissue targeting deep cortical layers in V1 and ventrally through the hippocampus to the base of the brain. Images were collected at $\sim$3.5 frames per second at multiple regions throughout the tissue. At the end of the imaging session, animals were given an overdose of sodium pentobarbital (240 mg/kg) prior to transcardial perfusion with phosphate buffered saline (PBS), and then 4% paraformaldehyde. The fixed brains were then extracted, and 50 μm thick coronal sections were made with a vibratome (Leica, Germany) to confirm the location of the fibre tract.

4.6 Conclusions

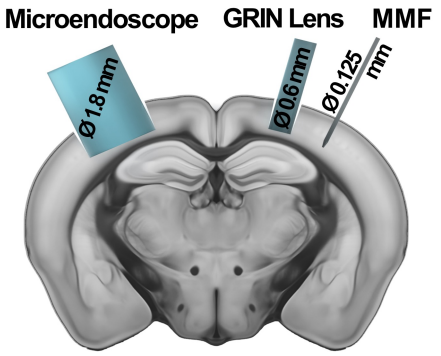

FIGURE 4.8: Scale-preserved comparison of the most typical endoscopic probes and a MMF.

In this work, we have designed a highly optimised optical pathway for fluorescence imaging of deep-brain structures with micrometric spatial resolution and causing minimal damage to the tissue surrounding the fibre penetration area. Deploying the most efficient wavefront-shaping algorithms and, currently, the fastest possible hardware for light modulation, our system is capable of taking 7-kilopixel images with micro-sized spatial resolution and imaging speeds of 3.5 frames per second, allowing adequate spatial and temporal resolution for fluorescent imaging in living tissues.

As a proof of concept, we were able to image fluorescent signal in vivo, deep within a mouse brain through a single MMF based probe. In anaesthetised transgenic mice with tdTomato fluorescent protein expression in a sparse subpopulation of inhibitory interneurons, we obtained visually identifiable images of neuronal somas and processes both in the visual cortex and in the hippocampus, more than 2 mm from the surface of the brain. While in our experiments the imaging was restricted to the cortex and hippocampus, with this technique the entire dorsal-ventral extent of the mouse brain (4-6 mm) can be covered, allowing imaging of even the most ventrally located nuclei in the brain.

The achieved resolution is limited only by the numerical aperture of the fibre, being comparable with a standard 10$\times$ microscope objective. Imaging

immediately after insertion of the endoscopic probe, which is only possible due to its minuscule footprint, eliminates the need for a long postoperative recovery period, as well as the necessity of surgical removal of overlying tissue and implantation of an imaging element, such as a GRIN lens [120, 121] (see Fig. 4.8). However, due to extremely high density and branched structure of neuronal cells ($\sim 10^5$ nuclei/mm^3) and blood vessels (normalised vascular length $\sim$ 0.9 m/mm^3) in the mouse brain [122], even microscale probes are unavoidably accompanied with tissue damage [99, 117–119], such as mechanical disrupture of neuronal processes and vessels and associated changes in neuronal structures and activity. For example, penetration can cause irregularities in spike activity [123], disruption of the blood-brain barrier [124–126], loss of blood perfusion to the surrounding neuronal cells [127]. Moreover, these factors affects tissue differently on acute and chronic timescales [117]. Therefore, I believe that studies on tissue damage and most importantly on its minimisation are inextricably linked to a particular application. Due to the micronscale size of the probes, a lot of practical knowledge on probe design [118], penetration or implantation strategies [117] and methods of damage assessment [128–130] can be translated from highly-developed (with successful implementation in humans) field of electrophysiology and human-machine interface, which strongly rely on arrays of micron-scale electrodes. This demonstration paves the way to in vivo implementation of numerous techniques of modern microscopy including multiphoton [29], super-resolution, and light-sheet approaches [101], which will further increase the performance presented here.

Chapter 5

High numerical aperture probes for microendoscopy

Although the work presented in the previous chapter proved holographic endoscopy to be a promising technology for neuroimaging, at the same moment, the growth of the speed to the applicable level immediately emphasised other issues to be prioritised in order to convert this concept into a versatile tool for brain studies.

Commercially available MMFs are currently mostly designed along telecommunication standards, with a low NA and a limited set of core diameters. Utilising such fibres with a NA equivalent to a 10x microscope objective for the in vivo demonstration, led to barely resolved neuronal processes and strong out-of-focus background. It became clear that future advancements will strongly rely on the development of new fibre types directly optimised for the needs of holographic endoscopy.

The following chapter presents one of the first works on implementation of the custom-made fibre probe with ultra-high numerical aperture reaching 1. Application of the novel fibres in holographic geometries came with new challenges, which required significant adaptation of the beam-shaping methods and experimental setup for full utilisation of the available focusing power.

Probably the most demanding in terms of sharpness and quality of the foci the biophotonics technique, holographic optical trapping has been chosen as an experiment for validating the high-resolution focusing ability of holographic systems based on the novel fibres. Recent works on in-vivo implementation of optical tweezers for studying mechanical properties of cells and tissues show growing need in precise measurements of forces in realistic environments [131–133]. However, all these works were performed in relatively optically transparent samples, such as embryos of drosophila and zebrafish or capillary vessels of mouse ears, due to previously explained limitations

for applications of optical methods in deep tissues. The successfully demonstrated here three-dimensional optical confinement and manipulation with arrays of micro-particles broaden the possibility for in-vivo applications of optical tweezers in previously inaccessible conditions.

Note that the potential of the obtained results is not limited to optical trapping, but it opens new exciting perspectives for in vivo deep-tissue implementations of advanced techniques relying on tightly focused laser beams, such as super-resolution imaging and targeted ablation.

Related paper:
Leite, I. T., **Turtaev, S.**, *Jiang, X., Šiler, M., Cuschieri, A., Russell, P. S. J., & Čižmár, T. "Three-dimensional holographic optical manipulation through a high-numerical-aperture soft-glass multimode fibre." Nature Photonics, 12(1), 33,* ***2018****.*

The contributions from the author of this thesis to the work presented in this chapter consisted of: (i) fibre probe preparation and post-processing for trapping experiments, (ii) performing the experimental evaluation of the temperature-induced effect on transformation matrix, (iii) performing the experimental demonstration of system resilience to fibre bending.

5.1 Fibre probe

The optical fibres utilised in this work represent a new class of step-index multimode fibres made from soft-glass materials, specially developed for very-high-NA applications. Two lead silicate glasses having very different refractive indices are used as the core and inner cladding materials – respectively Schott SF57 (a dense flint) and Schott LLF1 (a very-light flint) – whereas an outer cladding of fused silica increases the mechanical resilience of the fibre. Such high refractive index contrast yields an NA of 0.98 in the middle of the visible spectrum and 0.96 at the near-infrared wavelength of 1.064 μm, values previously accessible only with microstructured optical fibres [134]. However, these two glasses are also characterised by very distinct melting temperatures, posing natural difficulties in the fibre drawing process, which required designing a customised heating element. Analogous to the in vivo probe characterisation in Sec. 4.2, Figure 5.1 shows the available NA in front of the output fibre endface, estimated in the ray-optics approximation, and using the parameters $\mathrm{NA}_{\mathrm{fibre}} = 0.96$ and core diameter $d = 20\,\mu\mathrm{m}$ for the fibre, and $n = 1.333$ (water) for the refractive index of the surrounding medium. The lower plot shows

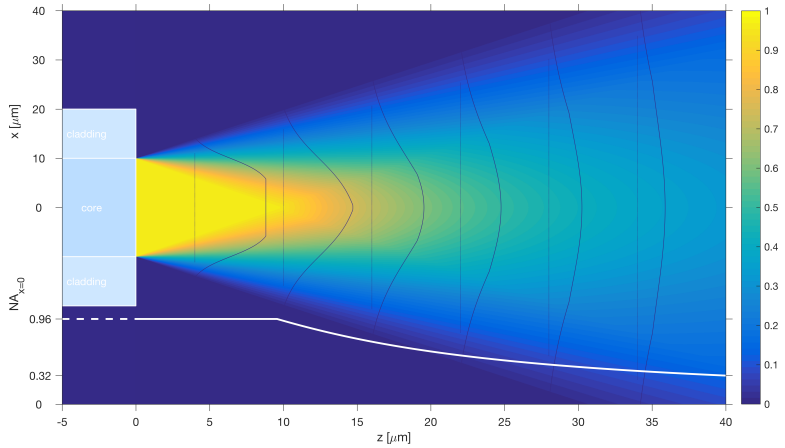

FIGURE 5.1: **Evolution of numerical aperture with distance from the output fibre facet.** The lower plot shows the evolution of the NA along the optical axis, and the series of dark subplots illustrate the NA profiles across different axial planes in front of the fibre.

the evolution of the on-axis NA with increasing distance z from the fibre, given by:

$$NA = \min\left\{ NA_{fibre}\, n \sin\left[\tan^{-1}\left(\frac{\frac{d}{2}}{z} \right) \right] \right\}. \tag{5.1}$$

The maximum available NA of the fibre is in a conical region in front of the fibre endface whose apex is at a distance of approximately 10 µm from the fibre. Accordingly, the volume in front of the fibre facet where the NA is maximum is approximately 1000 µm^3. The trapping experiments were performed with the calibration plane located at a distance $z \simeq 4$ µm from the fibre facet (represented in Fig. 5.1 as the left-most NA axial profile) to allow for access of the particles as well as manipulation depth in the axial direction. At this distance, the region in which the NA is maximum is about 12 µm in diameter.

The core size is 20 μm in diameter and at 1.064 μm the fibres sustain approximately 1600 guided modes. To demonstrate their potential as minimally-invasive probes, the fibres are post-processed into a flat-cone termination as shown in the figure 5.2. The approach, detailed in Sec. 4.3, involves mechanically polishing the cladding of one end of the fibres at a grazing angle of around 5°, reducing the overall fibre diameter from the initial 125 μm down to just 35 μm.

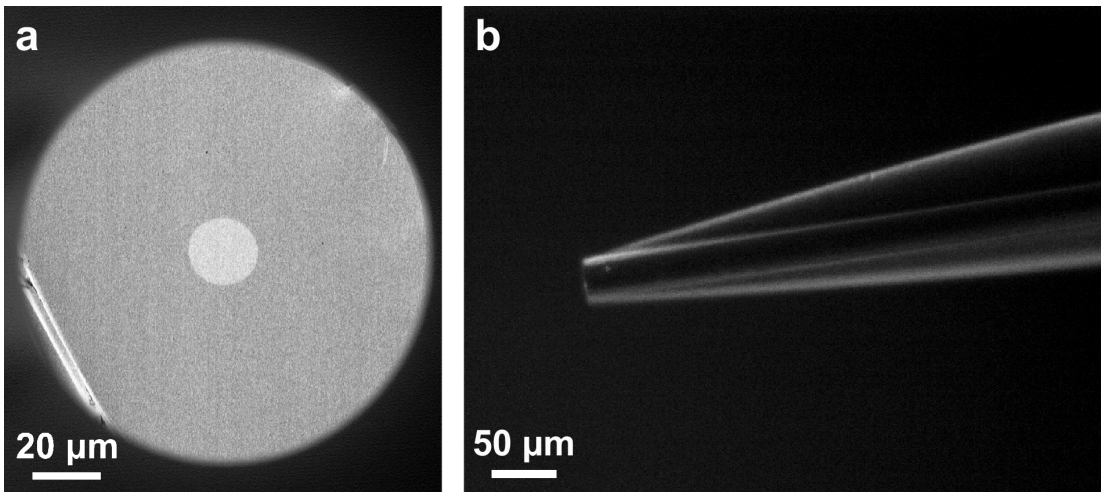

FIGURE 5.2: **High-NA step-index multimode fibre probe. a**. SEM image of the fibre endface. The diameters of the core and of the cladding are 20 µm and 125 µm, respectively. **b**. Micrograph of a post-processed fibre probe where the cladding thickness has been reduced to 35 μm (at the tip) by side-polishing.

5.2 Mode dependent losses

In MMFs, not all guided modes experience the same degree of attenuation. Instead, the higher order modes, those carrying the larger spatial frequencies, suffer from higher losses than the lower order modes [135, 136]. Such mode dependent losses (MDL) manifest itself as an angular-dependent intensity distribution in the far-field output, as depicted in Fig. 5.3 a. Importantly, this imbalance on the output spatial frequency spectrum poses a limit to our ability of producing sharp foci at the distal facet of the fibre. In the low-NA fibres utilised in the previous chapters this effect is negligible, but when employing high-NA fibres with lengths exceeding a few centimetres, we have observed a substantial difference. To overcome this limitation, it is therefore necessary to significantly intensify the higher-order mode-groups so to achieve the uniform distal far-field distribution, as depicted in Fig. 5.3 b.

In order to measure the MDL, we coupled into the fibre a set of input plane-wave modes as explained in Sec. 3.5.2. Coupled to the fibre, truncated plane waves excite a group of fibre modes with similar propagation constants (transverse spatial frequencies), defined by the $\vec{k}$-vector of the the corresponding plane wave. Therefore, integrating the output power at the CCD for each of the coupled plane waves allows measuring the intensity map shown in Fig. 5.4, containing the information of the optical transmittance of the different mode groups, which will be later used for MDL compensation. Figure 5.4 shows the azimuthally-averaged intensity distribution for different fibre lengths, as a function of the normalised spatial frequency $n \sin\theta = k_t/k_0$, where $k_t =$

$\sqrt{k_x^2 + k_y^2}$ is the transverse component of the wave vector and $k_0 = 2\pi/\lambda$ its magnitude in vacuum. The insets in Fig. 5.4 display the mode-dependent transmission measured for the longest and shortest fibres (150 mm and 50 mm long), as a function of the normalised spatial frequencies $q_{x,y} = k_{x,y}/k_0$.

5.3 Experimental setup

The experiment on optical trapping, chosen for the demonstration of high-NA probes' potential, does not benefit from high-speed operation. Furthermore, the stiffness of the traps depends on the optical power of the trapping beam. Following conclusions from Chapter 3, this work takes advantage of a liquid-crystal based modulator, providing high optical efficiency at a cost of scanning speed.

The experimental setup used in this work is depicted schematically in Fig. 5.5. It consists of two decoupled parts, the first dividing the laser beam into a signal and a reference beams and coupling them into single-mode polarisation-maintaining fibres (PMF1 and PMF2, respectively). Besides carrying the signal and reference beams to the main subset of the system, PMF1 and PMF2 serve also as Gaussian spatial filters. Lenses L1 and L2 form a telescope to demagnify the size of the beam originated at the laser source (Yb fibre laser, 1.064 µm wavelength, continuous wave), and a half-wave plate HWP1 aligns its polarisation with the polarisation axis of the Faraday optical isolator OI. A half-wave plate HWP2 together with a polarising beamsplitter cube PBS1 allow

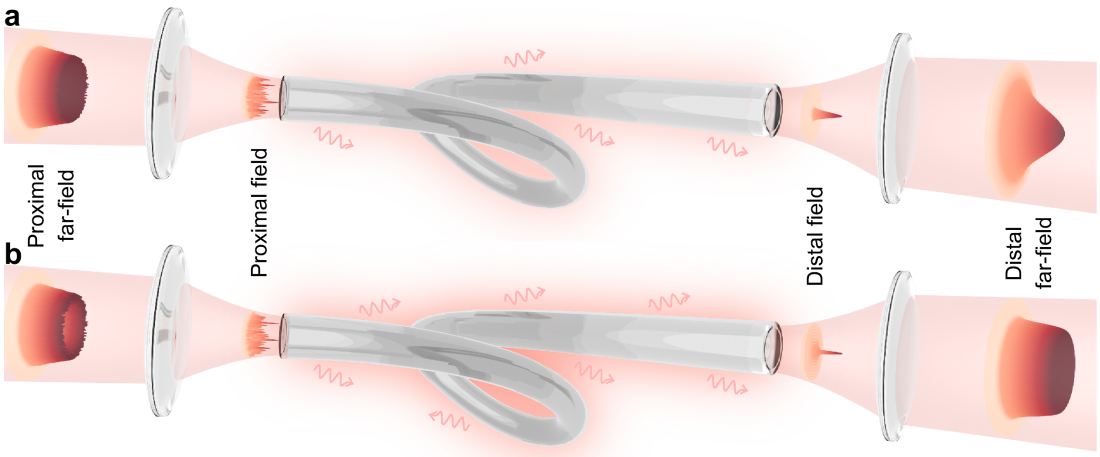

FIGURE 5.3: **Illustration of mode-dependent losses.** **a**. The presence of mode-dependent losses (MDL) in multimode fibres preferentially attenuates higher spatial frequencies, limiting the achievable output NA of the generated foci at the distal fibre facet. **b**. MDL can be pre-compensated in the proximal far-field, so to equalise the power spectrum in the distal far-field, later detailed in Sec. 5.4.1.

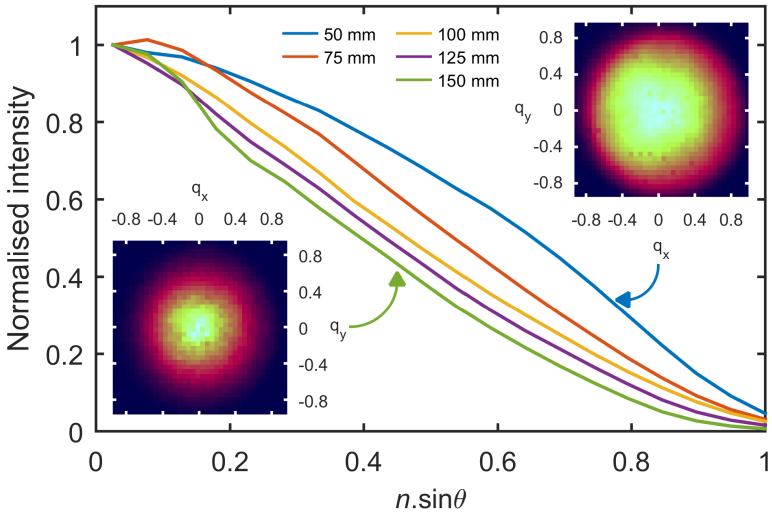

FIGURE 5.4: **Measurements of the mode dependent loss.** Azimuthally averaged measurements of the mode-dependent transmission for fibre segments of varying lengths, from 50 to 150 mm. The inset figures show normalised measurements of the spatial-frequency dependent intensity for a fibre with length 50 mm (top-right) and for another with length 150 mm (bottom-left).

controlling the total amount of power propagating in the optical system (the excess power is diverted towards a beam block BB), whereas a half-wave plate HWP3 and a polarising beamsplitter cube PBS2 allow adjusting the power ratio between the signal and reference beams, which are coupled into PMF1 and PMF2 via aspheric lenses L3 and L4, respectively.

The signal beam leaving PMF1 is collimated and expanded by lens L5 to overfill the spatial light modulator SLM under a small incidence angle. A half-wave plate HWP4 is used to align the polarisation of the signal signal beam with the polarisation axis of the SLM. An aperture APT1, placed in the far-field of the SLM, isolates the first diffraction order while blocking all others. Lenses L6 and L7 are placed in a $4f$ configuration and image the first diffraction order of the holograms generated at the SLM onto a dielectric mirror M1. Lens L8 and an oil-immersion microscope objective MO1 are also placed in a $4f$ configuration and further relay the holograms from M1 to the input facet of the multimode fibre MMF. The combination of L6, L7, L8, and MO1 chosen ensures the necessary demagnification ($370\times$) of the phase holograms such that their image size matches the dimensions of the MMF core. M1, being conveniently placed in a plane conjugate to the input fibre facet, serves as a steering mirror to finely adjust normal incidence onto MMF.

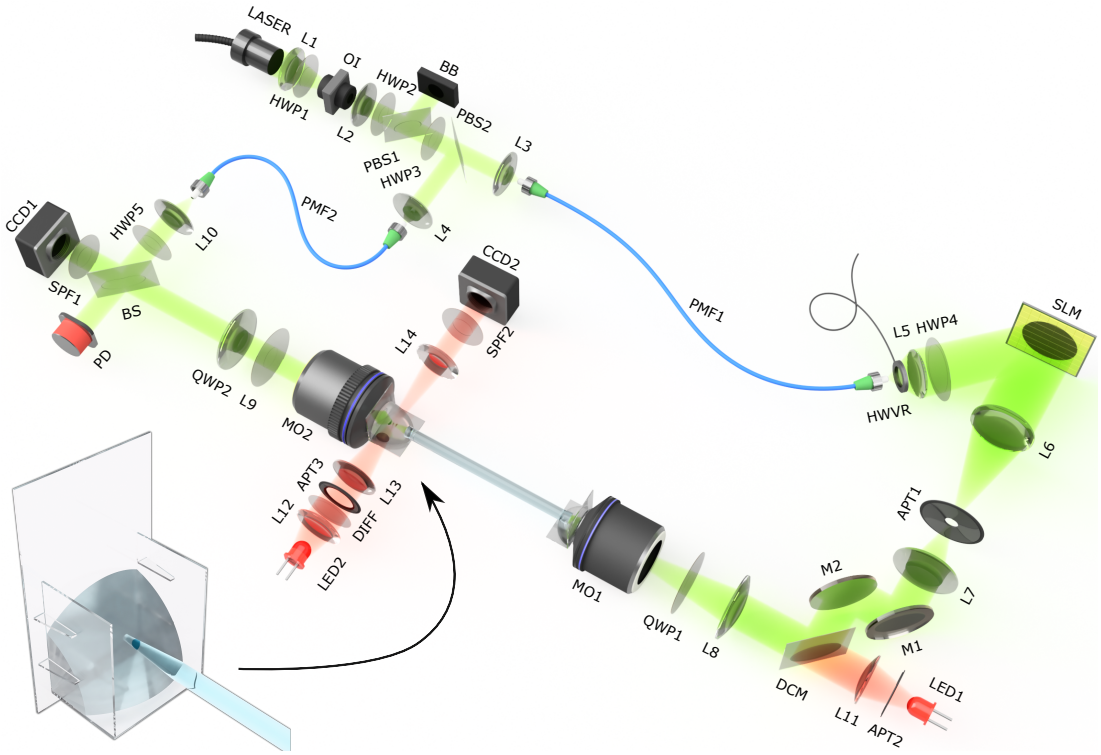

FIGURE 5.5: **Scheme of the setup for the trapping experiment. LASER**: Yb fibre laser, 1.064 µm CW (IPG Photonics YLR-10-1064-LP-SF); **SLM**: reflective liquid crystal on silicon (LCoS) spatial light modulator (BNS HSPDM512-800-1064); **MO1**: oil-immersion microscope objective (Olympus UPlanFL 100x/1.30 Oil); **MO2**: water-immersion microscope objective (Olympus UPlanSApo 60x/1.20 W) mounted on a piezo nanopositioner (Mad City Labs Nano-F100); **CCD1 and CCD2**: charge coupled device GigE camera (Basler pilot piA640-210gm); **PD**: thermal power detector (Thorlabs S302C); **HWVR**: half-wave liquid crystal variable retarder (Thorlabs LCC111-C); **LED1**: light-emitting diode 625 nm (Thorlabs M625L3); **LED2**: warm white light-emitting diode (Thorlabs MWWHL3); **OI**: Faraday optical isolator (LINOS FI-1060-8SI); **BB**: beam block (Thorlabs LB2); **PMF1 and PMF2**: polarisation maintaining fibre (Thorlabs PM980-XP); **PBS1 and PBS2**: polarising beamsplitter cube (Thorlabs PBS103); **BS**: 50:50 non-polarising beamsplitter cube (Thorlabs BS011); **HWP1 to HWP4**: half-wave plate (Thorlabs WPMH10M-1064); **QWP1 and QWP2**: quarter-wave plate (Thorlabs WPMQ10M-1064); **DCM**: shortpass dichroic mirror, 805 nm cut-off (Thorlabs DMSP805R); **SPF1 and SPF2**: shortpass filter, 800 nm cut-off (Thorlabs FES0800); **APT1 to APT3**: iris diaphragm (Thorlabs SM1D12D); **M1 and M2**: broadband dielectric mirror (Thorlabs BB1-E03); **L1, L8 and L9**: achromatic doublet, $f = 200$ mm (Thorlabs AC254-200-C); **L2**: achromatic doublet, $f = 100$ mm (Thorlabs AC254-100-C); **L3 and L4**: aspheric lens, $f = 8.07$ mm (Thorlabs C240TME-1064); **L5**: achromatic doublet, $f = 50$ mm (Thorlabs AC254-050-C); **L6**: achromatic doublet, $f = 250$ mm (Thorlabs AC254-250-C); **L7**: achromatic doublet, $f = 75$ mm (Thorlabs AC254-075-C); **L10**: aspheric lens, $f = 11.21$ mm (Thorlabs C220TME-1064); **L11**: achromatic doublet, $f = 100$ mm (Thorlabs AC254-100-A); **L12**: achromatic doublet, $f = 30$ mm (Thorlabs AC254-030-C); **L13**: achromatic doublet, $f = 25$ mm (Thorlabs AC127-025-A); **L14**: aspheric lens, $f = 8.00$ mm, NA = 0.50 (Thorlabs C240TME-A);

The distal end of the MMF is immersed in a water droplet held by a custom-made cuvette (inset of Fig. 5.5) which is in contact with a water-immersion microscope objective MO2 through a water-index-matching medium. MO2 in combination with tube lens L9, image the MMF output facet (or, in general, any desired calibration plane at a given distance from the endface) onto camera CCD1 with a magnification of 66×. MO2 is mounted on a piezo nanopositioner allowing a precise focussing adjustment, critical for the trap characterisation measurements as well as for the reconstruction of the 3D profile of the focal points.

Quarter-wave plates QWP1 and QWP2 are used to convert the polarisation state of the signal beam from linear-to-circular and circular-to-linear, respectively, as circularly-polarised modes are shown to be better preserved upon propagation in MMFs [33].

A non-polarising beamsplitter cube BS combines the signal and reference beams at CCD1 for the interferometric measurement of the transmission matrix, and diverts a portion of the signal beam towards the power detector PD, allowing to assess the output power from the MMF. Half-wave plate HWP5 is used to align the polarisations of the signal and reference beams to maximise the contrast in the interference patterns.

A dichroic mirror DCM placed in the optical path allows coupling incoherent light from LED1 into the fibre, to provide uniform illumination on the trapped objects for *en face* imaging by CCD1, and a short-pass filter SPF1 is placed to block the trapping beam. Lens L11 images an aperture APT2 onto the back-focal plane of MO1. LED2, lenses L12 and L13, a diffuser DIFF, and an aperture APT3 provide a pseudo-Köhler illumination for side-view imaging through lens L14 onto camera CCD2. A short-pass filter SPF2 is used to filter out scattered light from the trapping beam.

A variable retarder HWVR is used to control the amount of power in the trap site (in closed-loop with feedback from PD) during the characterisation of the optical tweezers, as it allows introducing, in the signal beam, a polarisation component orthogonal to the polarisation axis of the SLM with variable amplitude, whose power remains in the zero diffraction order and is thus filtered out by APT1.

5.4 Holographic methods

5.4.1 Principal changes to overcome MDL

The measurements of MDL, performed above (see Fig. 5.4), shows that individual mode groups experience different amounts of attenuation, those with smaller propagation constants (with higher transverse spatial frequencies) have higher loss (see Fig. 5.3 a). In order to tackle this limitation, it is therefore necessary to significantly intensify the higher-order mode-groups in order to achieve the uniform distal far-field distribution, as depicted in Fig. 5.3 b.

In the conventional plane wave based approach, utilised in Chapters 3 and 4, the spatial light modulator is relayed onto the back focal plane of the coupling objective, i.e. a plane conjugate to the proximal far-field. The only way to achieve the required power distribution in this arrangement is to discard the excessive power in the central zones, which would be associated with a significant power loss. A modified system utilised in this work, with an additional lens to project the SLM directly onto the input fibre facet, allows altering the spatial content of the holographic modulation. In this arrangement, the power could be redistributed between the central and the peripheral zones of the proximal far-field without incurring the prohibiting power loss.

Additionally, in order to harness the full NA of the novel fibres, the coupling of light into and out of the MMF is performed through an immersion layer and uses objectives lenses with NAs higher than that of the fibre – an oil immersion layer and a 1.4 NA microscope objective on the proximal fibre facet, and a water immersion (compatible with the trapping experiments) 1.2 NA microscope objective on the distal facet.

5.4.2 Calibration and foci generation

TM measurments

Despite the implemented changes in the setup (a fibre facet placed at the image plane of the SLM), the algorithm for TM measurements and foci generation remained almost the same. The phase holograms applied to a spatial light modulator are imaged onto the input fibre facet in the off-axis holography configuration, where the first diffraction order is isolated using a spatial filter. In order to measure the transmission matrix (TM) of the fibre, a calibration plane (at a given distance from the output fibre facet) is imaged onto a CCD detector, and an external phase reference is introduced in the optical pathway via a non-polarising beamsplitter. We have chosen a set of 38×38 orthogonal plane

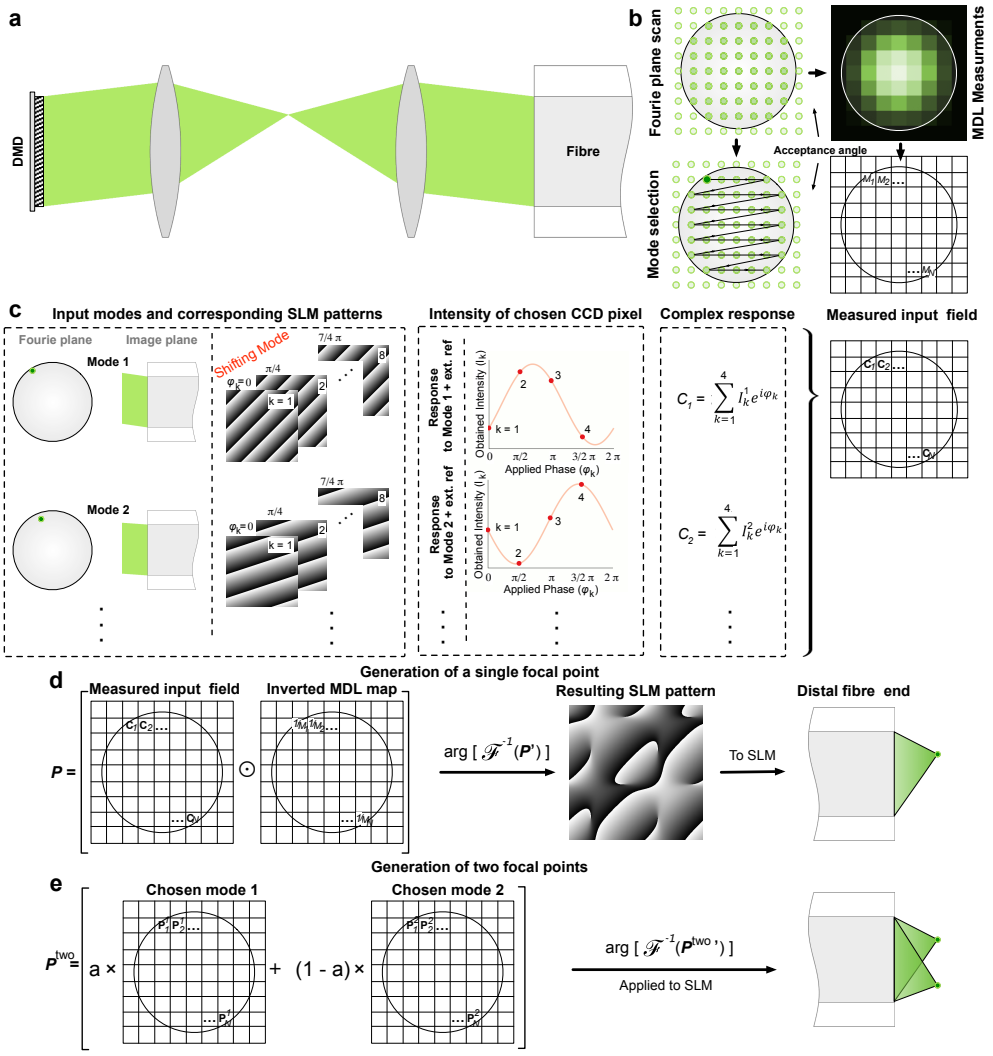

FIGURE 5.6: **Schematic illustration of the calibration procedure and foci generation.** Truncated plane waves in the image plane of the modulator, generated by gratings applied to the whole surface of the SLM, are used as the a basis of input modes for TM measurements (**a**). Projected to the fibre facet, such modes could be employed for preliminary scanning of the fibre facet for selecting only the modes, that fall within the acceptance angle of the fibre, as well as for evaluating the impact of the MDL (**b**). Following the same algorithm based procedure as explained in Sec. 3.5.2, the response for each of the selected modes could be obtained by analysing the signal from the selected pixel of CCD camera (**c**). Complex responses to each input mode multiplied by the inverted MDL map (redistributing power towards higher order modes) (**P**) are arranged in the Fourier domain around the first order (**P′**) according to the initial position of the used input modes in the Fourier plane. Fourier transform of the arranged array (its phase part) are applied to the SLM in order to generate a focal point (**d**) at the selected position (chosen pixel of CCD camera). **e**. Simultaneous generation of two optical traps (foci). The SLM phase pattern is compiled a superposition (in the Fourier domain) of the calculated complex fields, corresponding to the chosen output positions.

waves as the basis of input modes, whereas the output modes are heavily oversampled, consisting of a square grid of 100×100 points at the calibration plane which are conjugated to individual pixels in the CCD detector. Using the SLM to change the phase difference between a given input mode and the external phase reference, leads to a harmonic signal of the intensity in each position of the grid of output modes. Thus, the complex field (i.e. both amplitude and phase) at each position of the calibration plane can be retrieved by changing the phase difference steps, using the recorded intensity for each step. Important to note that, in this work, 8 steps of $\pi/4$ phase shift were used in order to suppress flicker-induced phase noise, as shown in Chapter 3. Acquiring the full TM corresponds to repeating this procedure for all chosen input modes.

Generation of foci

As shown in Fig. 5.6 d, in order to generate a diffraction-limited output mode at a particular position in the calibration plane, and taking into account the presence of the MDL, the obtained complex input field corresponding to this point (chosen row of the TM), is multiplied by the inverted map of the MDL (measured in Sec. 5.4.1), providing spectral amplitude modulation to redistribute power towards higher order modes.

One of the key advantages of holographic optical trapping is the capability to simultaneously manipulate with multiple optical traps. In order to simultaneously generate multiple diffraction-limited foci at the chosen output positions, the SLM phase pattern is compiled using phase information from the superposition of calculated complex fields, corresponding to the chosen output positions. Moreover, overall output power can be redistributed between the foci at will, by adjusting relative amplitude (a) of the two output modes, as shown in the Fig. 5.6 e.

Axial positioning of foci

Owing to the remarkable cylindrical symmetry of fibre-optic waveguides, the longitudinal component of the wave vector (i.e. the propagation constant) is very well conserved through the fibre (axial memory effect) [31]. Thus, a quadratic phase added to the spatial spectrum of the input modes is preserved and, therefore, found in the spatial spectrum of the output modes, resulting in a defocus and axial displacement of the diffraction-limited foci. When generating multiple output focal-point modes simultaneously, a defocus can be applied to each of them individually, using different quadratic phase masks

applied to the input complex modulation, corresponding to chosen output focal-point modes.

Fine lateral positioning of foci

Since the separation between the calibrated sites of the grid of output modes is much smaller than the spatial extent (spot-size) of each one of them, the fine positioning of a distal focal-point (FP) mode between such calibrated locations can be achieved by constructive interference of two neighbouring modes simultaneously. This results in a distribution of the optical field corresponding to a single FP, whose central position can be finely tuned by the relative amplitude of the two output modes.

When the FP separation approaches their size, the generated focus broadens, translating into a decreasing NA and stiffness of the holographic optical tweezers (HOT). To verify the limits of this approach, we have simulated the focus relocation for the FP separations, ranging from 0.1 µm to 0.8 µm using a TM calculated for a fibre having the same parameters of those used in our experiments. The resulting intensity distribution is fitted to an Airy disk distribution deformed elliptically, allowing us to retrieve the actual position of the focus as well as its effective NA (in the direction of the major axis, i.e. parallel to the line segment connecting the two FPs) as it is relocated.

The results of the simulations for the FP separations of 0.2 µm and 0.3 µm are shown in Fig. 5.7 a,b. We have complemented these simulations with experimental measurements, where the spacing between consecutive FPs is $\approx$0.23 µm. At each position, the intensity distribution of the relocated focus was reconstructed from three images taken at three distinct exposure times, and fitted to an elliptical Airy disk as in the simulations.

Figure 5.7 c shows the experimental data averaged over five measurements. For the 0.23 µm FP separation used in this work, we see that the effective NA is kept almost constant during the HOT fine positioning, and the total deviation from the expected trajectory is smaller than 5 nm. Moreover, the precision of each step along the trajectory is 1.8 nm for the step size used (23 nm). It is worth noting that the presence of MDL in the 65 mm-long fibre used in the measurements, not taken into account in the simulations, is responsible for a visibly smaller effective NA in the measurements when compared with the simulated data.

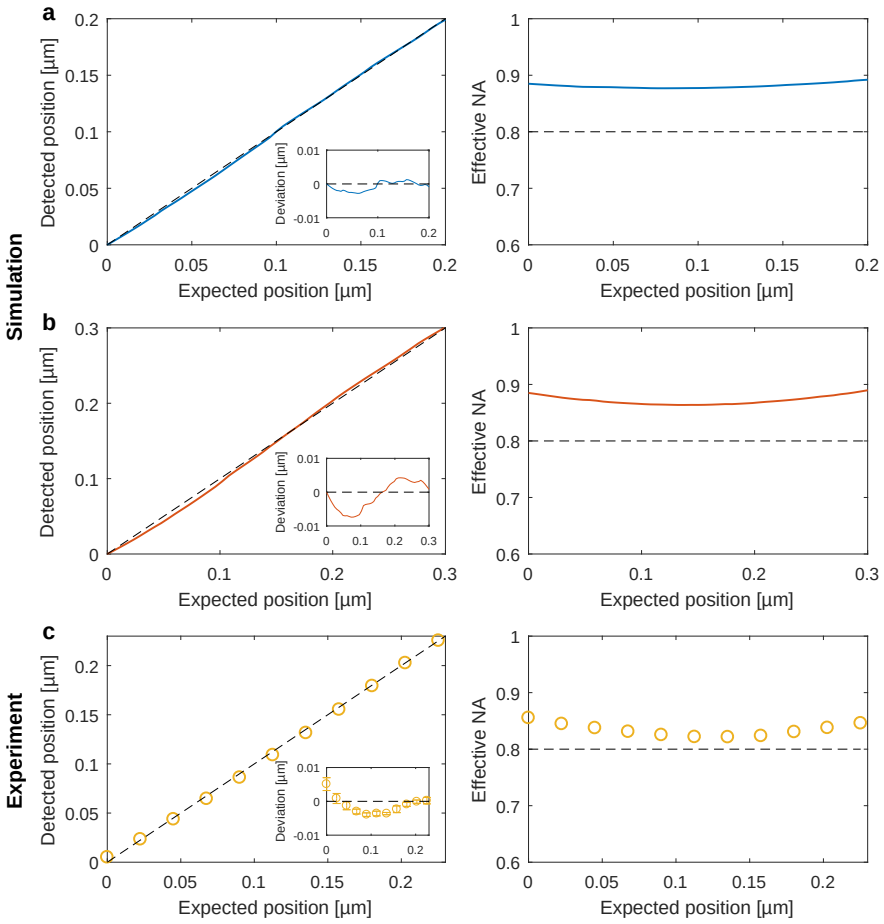

FIGURE 5.7: **Simulation and experimental data on fine lateral positioning of foci.** Detected central position and effective NA of the focus created by coherent superposition of two neighbouring FP output modes as a function of its expected central position. **a,b.** Simulated data using a FP separation of **(a)** 0.2 µm and **(b)** 0.3 µm. **c.** Experimental data with consecutive FP modes spaced by 0.23 µm. The error bars in **(c)** are smaller than the data markers. The horizontal dashed line indicates the NA value of 0.8 required for stable optical confinement and the inset figures show the deviation between the detected and expected positions of the focus as it is relocated between the two FPs.

5.4.3 Trapping procedure

A water-filled custom-made cuvette composed of 170 µm thick coverslips (inset of Fig. 5.5) is mounted in the system to immerse the distal end of the fibre into the liquid. A water-immersion microscope objective lens is translated towards the cuvette from the opposite side, with a water-index-matching medium applied in the cuvette-objective interface. The optical signal leaving the objective back-aperture is further imaged on a CCD using a tube lens. With this configuration, we proceed with the calibration procedure (measure the MDL and TM), which allows for further foci generation and manipulation. A

suspension of silica microspheres (Duke Standards^{TM}with 1.57 µm$\pm$0.02 µm in diameter) is pipetted into the cuvette and let diffuse within the water medium. For the following procedures, we block the trapping wavelength using a dielectric short-pass filter and provide incoherent illumination of the sample by using an LED at visible wavelength. For the face view, the illumination signal is delivered through the high-NA fibre, whereas for the side-view a standalone Köhler illumination pathway is provided. In all cases when the side-view imaging pathway is used, the water illumination objective is displaced away from the cuvette in order to allow sufficient space for the side-view imaging lens. A single optical trap, or an assembly of traps, is generated via computer-controlled SLM modulation which, based on the face view or side-view camera-feedback, is permanently adjusted manually from a LabVIEW based interface in order to confine the corresponding amount of particles diffusing into the vicinity of the distal end of the high-NA fibre. Records of the confined particles are then used for demonstrations of the instrument's versatility.

5.5 High-resolution focussing

The generation of high NA, diffraction-limited foci is of great importance in this work, as it is the enabling principle for HOT providing 3D optical confinement, but also forms the basis for other high NA techniques, including imaging. To assess the achievable NA of the system, as well as the impact of the MDL compensation, we have carried out a study where 91 focal-point modes are sequentially generated across the distal fibre facet. The procedure was repeated for several TM measurements and for varying length of the same fibre segment, which was successively re-cleaved to reduce its size in increments of 25 mm.

Since the intensity distribution of each FP mode spans over the 8-bit dynamic range of the CCD camera, three images are taken for each FP mode with exposure times of 0.1 ms, 1 ms, and 10 ms, in order to reconstruct its intensity distribution $I(x, y)$, where x and y denote the cartesian coordinates of the image in pixel units. One of such intensity distributions is shown in Fig. 5.8 a,b, prior and after MDL compensation. The FP mode shown was generated at a radial distance of 2.25 µm (from the fibre axis) and at a distance of 2.0 µm from the fibre facet, through a 50 mm long fibre. Each intensity distribution $I(x, y)$

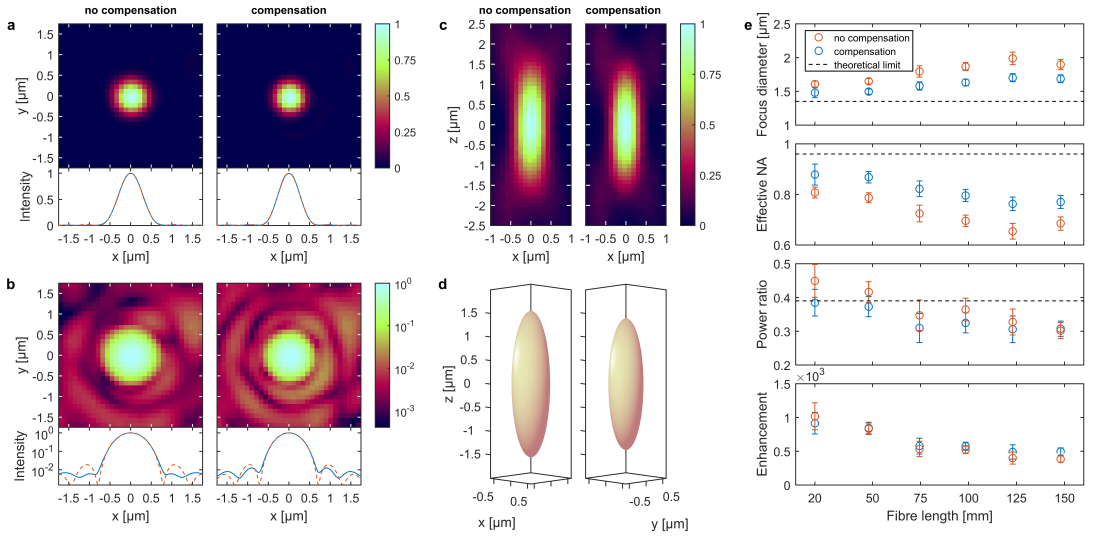

FIGURE 5.8: **High-resolution focussing through MMFs. a,b.** Transverse intensity profile of a focal-point (FP) mode, with and without MDL compensation, and comparison of the azimuthally-averaged intensity profile with the fitted Airy disk intensity distribution. The NA of the FP mode is enhanced from 0.82 ± 0.01 (prior to MDL compensation) up to 0.91 ± 0.01 (after MDL compensation). **c.** Longitudinal profile of the intensity distribution of the same FP mode. **d.** Ellipsoid fitted to the level surface with intensity corresponding to $1/e$ of the maximum value. The fibre used in **(a-d)** was 50 mm long. **e.** Influence of the MDL compensation on the Airy disk diameter, effective NA, power ratio, and enhancement for varying length of the MMF.

is fitted to a 2D Airy disk distribution:

$$f(x,y) = a\left(\frac{2J_1(\rho)}{\rho}\right)^2 + b, \tag{5.2}$$

where J_1 is the Bessel function of the first kind of order one, and

$$\rho = \frac{\sqrt{(x-c)^2 + (y-d)^2}}{e}, \tag{5.3}$$

with a, b, c, d, and e being free parameters (a measures the amplitude, b the average speckled background, c and d the Cartesian coordinates of the centre of the distribution, and e its width). In Fig. 5.8 a,b, the fitted distribution $f(x,y)$ is compared with the azimuthally averaged $I(x,y)$. With the knowledge of the pixel size in the CCD (7.4 µm) and the calibrated magnification of the *en face* imaging pathway (66×), the diameter of the Airy disk, taken as first-zero-ring in Eq. 5.2, can be estimated as $d_{\text{Airy}} = 2 \cdot 3.8317 \cdot 7.4\,\mu\text{m} \cdot e/66$. The corresponding effective NA can then be retrieved as $\text{NA} = \frac{1.22\lambda}{d_{\text{Airy}}}$, where λ is the wavelength in free space (1064 nm).

By scanning the imaging objective axially in steps of 100 nm, we were able

to reconstruct the 3D intensity profile of the FP mode shown in Fig. 5.8 a,b. Figure 5.8 c shows the longitudinal profile of the FP mode, where the spot size in the axial direction is approximately 3.8 times larger than its lateral dimension, both with and without MDL compensation. Figure 5.8 d shows the 3D structure of this FP mode as an ellipsoid fitted to the level surface corresponding to $\frac{1}{e}$ of the maximum intensity.

In addition to the achievable NA, which determines the volumetric confinement of light, other parameters quantifying the uncontrolled background are also important in view of proposed applications. The *power ratio* is the fraction of total output power at the distal fibre facet which is contained in the FP mode, and can be estimated as $\gamma^2 = \sum_{x,y}[f(x,y) - b] / \sum_{x,y} I(x,y)$. The *enhancement* is defined as the ratio between the maximum intensity of the generated FP mode and the average speckled background, which can be calculated as $\eta = \frac{a+b}{b} \simeq \frac{a}{b}$. Figure 5.8 e summarises the results of this study, showing the focus diameter (defined as the first zero-ring in the Airy disk), effective NA, power ratio, and enhancement for each fibre length tested. Our MDL compensation increases the NA in average by 0.09. However, the ability to generate FP modes with higher NA decreases with increasing fibre lengths. As the optical loss grows exponentially with the fibre length, the transmitted power by the higher-order group modes becomes comparable to the noise level in case of the longer fibres. This translates into increasingly larger errors in the measurement of the MDL, thus limiting the efficiency of the compensation for the higher spatial frequencies, leading to a decreasing available NA with increasing fibre length. The power ratio across all fibre lengths is around $(33 \pm 4)\%$ with and $(37 \pm 5\%)$ without MDL compensation. This means that, in the HOT characterisation experiments, about 67% of the measured power is distributed as background outwith the trap site. We note that the theoretical limit for the power ratio in the case of phase-only modulation is shown to be $\frac{\pi}{4} \simeq 78.5\%$ [29]. However, in the presence of complete polarisation mixing, and if only one polarisation state is controlled (as in this work) this value is further reduced by half, being $\frac{\pi}{8} \simeq 39.3\%$ – a value in agreement with the experiments.

5.6 Three-dimensional trapping and manipulation

As explained in Sec. 5.4.3, once the calibration is done, a suspension of silica microspheres was pipetted into the water-filled cavity (image of the cavity inserted in Fig. 5.3). Particles for further demonstrations were initially trapped,

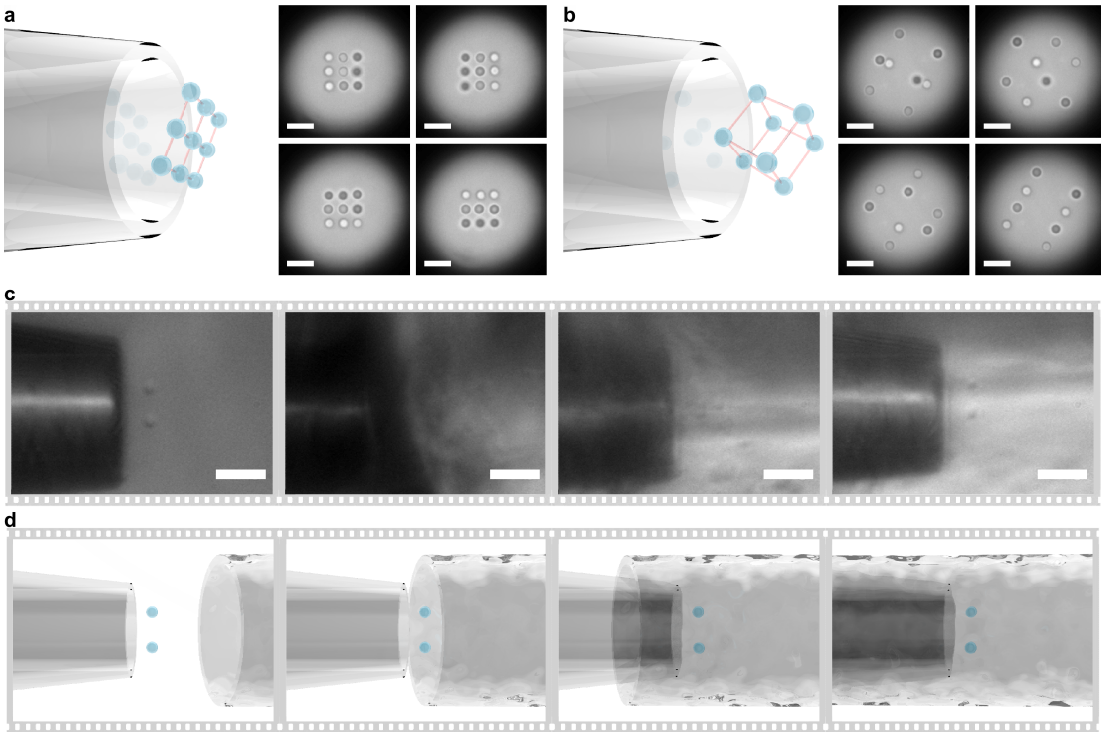

FIGURE 5.9: **Multiple holographic tweezers delivered through a lensless multimode fibre. a,b.** Multiple holographic tweezers trapping of **(a)** nine particles in a square-grid arrangement, and **(b)** eight particles forming a rotating three-dimensional cube. The different brightness of the particles arises from their varying axial positions relative to the focal plane of the imaging microscope objective (the particles appearing 'brighter' are at a greater distance from the fibre endface). Incoherent light for illumination is also delivered through the fibre core, which is visible as a blurred disk in the background. The scale-bars correspond to 5 µm. **c,d.** Optical manipulation of two particles inside a turbid cavity comprising a complex, hard-to-access environment. The scale-bars correspond to 10 µm. In **(a-d)**, all the particles are 1.5 µm-diameter silica microspheres in a water suspension, the fibre length is 65 mm, and the trapping wavelength is 1064 nm in vacuum.

using a LabVIEW based interface, designed for manual trapping manipulation, and allowing to relocate the trap by pointing (mouse click) a desired position on the image of the chosen focal plane, imaged in real-time by the en face-view camera.

Being inherently holographic, the technique allows for the simultaneous generation of multiple trap sites, and controlling their position in all three dimensions independently. Figure 5.9 a shows the top view of nine silica particles with 1.5 µm in diameter being trapped in a square-grid arrangement at a distance of 5 µm from the fibre facet. Incoherent light for illumination is delivered to the scene also by the fibre core, and is visible as a blurred bright disk in the background of the top-view images. The tilt and skew control of the geometrical arrangement, and consequent change in axial distance from the

fibre facet, manifests itself as the change in brightness of the trapped particles, which are being moved with respect to the focal plane of an imaging objective. In Fig. 5.9 b, the three-dimensional dynamic control of the optical tweezers is demonstrated by trapping eight particles simultaneously in a rotating cube arrangement. The top view images show snapshots of a video recording of the rotating structure.

Having such small footprint, the fibre based HOT could now have access to the inside of optically inaccessible cavities. To verify this, we used a small semi-opaque tube comprised of roughly polished PMMA with an opening as small as $\sim$125 µm. The simultaneous optical tweezing of two particles while the fibre is being inserted in the tube is shown in Fig. 5.9 c-d, comprised of roughly polished PMMA taken from the polymer coating of a commercial optical fibre.

An advantage of the beam-shaping approach based on the transmission matrix (TM) measurement is that the holograms for generating all output modes in the field of view can be readily calculated, therefore allowing to create them on demand and in real time. In our particular case, the basis of output modes corresponds to individual pixels in the CCD camera, so each column of the transmission matrix contains the input hologram to generate a diffraction-limited focus at a different site of a square grid, at the distal facet of the fibre. The lateral motion of a trapped particle is thus achieved by sequentially generating consecutive/adjacent output modes, which are spaced by approximately 0.23 µm. Axial motion is achieved by applying a defocus on the output modes, by adding a positive or negative quadratic curvature to the wavefronts.

In aqueous media, confined particles are subject to Brownian motion, so that recording their 3D trajectories can be used to analyse the strength (stiffness) of the optical trap. Since fibre based HOT is incompatible with the standard approach of back-focal-plane interferometry [137], we developed an algorithm to extract the particle positions from high-speed video recordings.

Figure 5.10 summarises our study of the trap stiffness along each coordinate for varying fibre lengths. We used the same segment throughout the study, re-cleaving it several times to shorten its length in increments of 25 mm. To verify that the axial confinement is indeed due to optical forces, the fibre was oriented horizontally so as to eliminate the gravitational effects in the axial direction. The trapped objects were silica microspheres of 1.5 µm in diameter and the wavelength was 1064 nm. Increasing the fibre length clearly degrades the trap stiffness, particularly in the axial direction. At the same time,

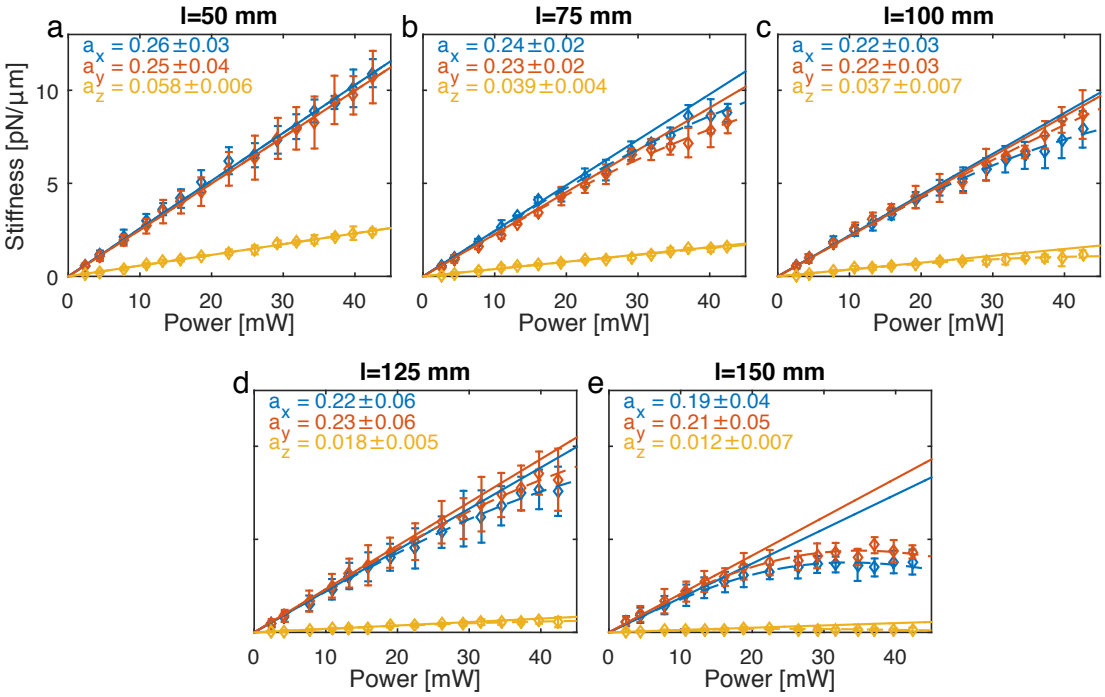

FIGURE 5.10: **Performance of multimode fibre based holographic tweezers. a-e.** Trap stiffness for each coordinate as a function of the total optical power leaving the distal fibre end, for various fibre lengths. Since the dependence visibly deviates from linearity, the data-set has been fitted to $\kappa = aP\exp(-\frac{P^2}{b^2})$ (dashed lines), where κ is the stiffness, P is the output optical power, and a and b are two fitting parameters. The parameter a reveals the initial linear trend (solid lines), and its values (in units of pN/µm/mW) are included in the top-left corner of each plot.

we see that the power dependence also visibly departs from linearity, especially for longer fibres. Both these effects are connected to MDL. Even with MDL compensation, the available NA is reduced (as shown in 5.8 e). Moreover, for longer fibres, the MDL compensation intensifies the power of the lossy mode groups, which leads to temperature increase due to optical absorption. This causes changes to the TM and consequently reduces quality of the optical traps.

Comparing these results with the state-of-art HOT systems based on high-NA microscope objectives, our traps are roughly one order of magnitude weaker. This is in good agreement with our expectations – the optical traps only carry about 33% of the output optical power (see 5.8 e) and, although sufficient for 3D confinement, the available NA is $\approx 20-30\%$ lower.

Next to sufficiently strong confinement, practical applications of HOT also require fine positioning with nanometric precision. In order to demonstrate this, we have implemented above-detailed principles to relocate an optical trap in a step-wise manner, both axially (see methods in Sec. 5.4.2) and laterally(see

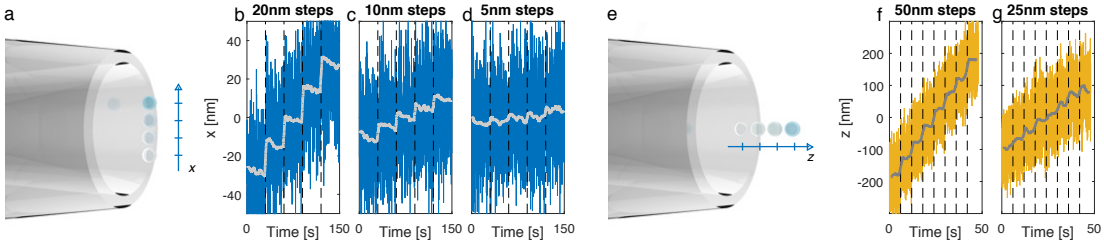

FIGURE 5.11: **Nanometre-scale positioning. a-d.** Sequential relocation of the trap site along the lateral direction, in increments of (**b**) 20 nm, (**c**) 10 nm, and (**d**) 5 nm . **e-g.** Sequential relocation of the trap site along the axial direction, in increments of (**f**) 50 nm and (**g**) 25 nm.

methods inSec. 5.4.2), while recording the particle position. Figure 5.11 a-d reveals that even 5 nm lateral steps ($\approx 50\times$ smaller than the separation of the output modes in the TM measurements (23 nm)) can still be resolved. Due to weaker localisation in the z-direction, the smallest resolvable axial steps are five times larger (Fig. 5.11 f,g).

Both these studies clearly confirm that the trapping performance is indeed sufficient, even for advanced applications in biomedical research [137, 138].

5.7 Applicability examination

5.7.1 Resilience to fibre bending

In practical applications of HOT introduced in vivo by a MMF, a certain degree of bending may be unavoidable, for instance due to mechanical stress induced by the surrounding tissue or to the dynamic nature of living specimens (e.g. due to breathing, heart beating, etc.). To demonstrate the HOT's resilience to bending of the fibre, we have conducted an experiment in which a 65 mm long fibre is subject to bending while trapping a silica microsphere. The bending occurs in the unheld distal segment of the fibre ($\approx$15 mm long) by means of a controlled pressure applied near the fibre endface by a motorised stage moving upwards, as depicted in Fig. 5.12. Notably, the particle remained confined by the HOT even when the fibre endface was translated by 2 mm, the maximum allowed by the conditions of the experiment, thus introducing a radius of curvature of 5 cm. The demonstrated resilience to fibre inclination from the straight position is promising for fibre imaging applications in-vivo, especially, taking into account that modern techniques in imaging of head-fixed rodents allow to limit the maximal displacements of the brain to 1-1.5 micrometers even in motile scenarios [139].

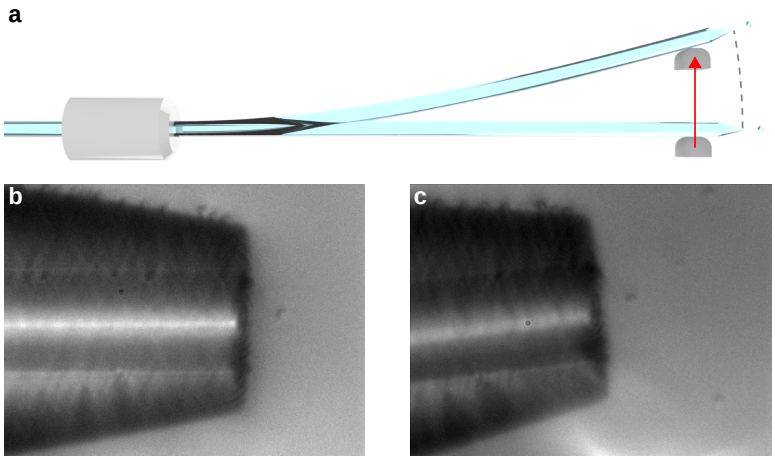

FIGURE 5.12: **Resilience of HOT to fibre bending. a.** A static HOT confining a silica microsphere (1.5 µm diameter) is delivered through a fibre with length 65 mm. The unheld distal portion of the fibre (15 mm long) is initially straight and is then progressively bent due to the force applied by a motorised stage moving upwards. **b.** Side-view image of the trapped particle in the initial, straight conformation of the fibre. **c.** Side-view image of the trapped particle in the final, bent conformation of the fibre corresponding to a vertical displacement of 2 mm and a radius of curvature of 5 cm.

5.7.2 Effect of temperature

Power absorption in the MMF leads to an increase in its temperature, which modifies the measured TM. This was seen in the characterisation of the optical tweezers, where the increasing optical power causes the trap site to displace axially by a few micrometers (Fig. 5.13 c). Remarkably, in the first instance, the quality of the trap is seen to be well preserved as the trap stiffness increases linearly with the optical power, especially in the case of fibres with a length smaller than 100 mm (main text Fig. 5.10). This lead to the hypothesis that, in the first instance, the optical absorption gives rise to a defocus of the focal point (FP) modes, and further increasing power leads to the degradation of the TM.

To test this, we measured the TM of a $\approx$ 170 mm long fibre under varying temperature. With respect to the system shown in Fig. 5.5, the setup was modified into an upright configuration with the fibre bent 180° between the two microscope objectives at the bottom. This allowed immersing $\approx$ 100 mm of the fibre in a thermal bath, whose temperature was controlled in closed-loop and could be kept constant with precision down to 0.01 °C.

Comparing the several TM measurements at different temperatures with

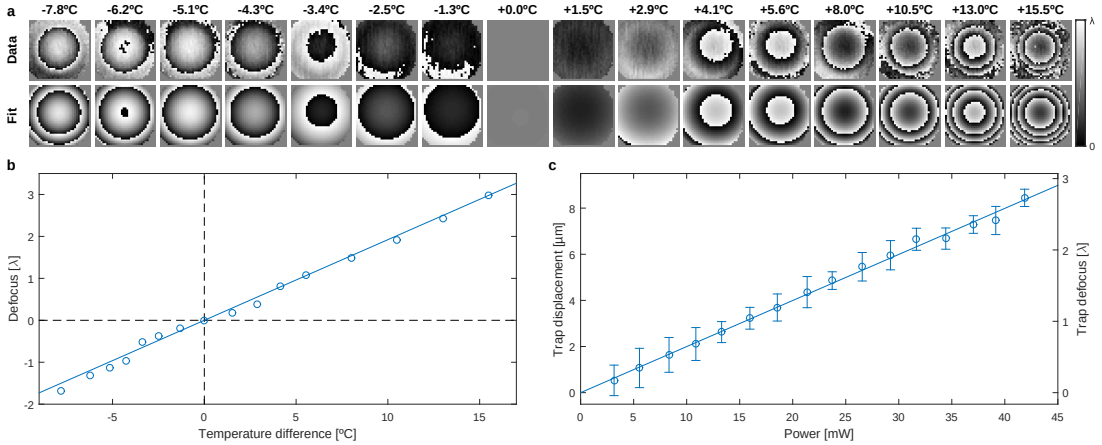

FIGURE 5.13: **Effect of temperature on the transmission matrix. a.** Phase difference in the proximal far-field with respect to the TM measurement at room temperature, and fit to a quadratic phase. **b.** Corresponding defocus (in units of wavelength) as a function of the temperature difference. **c.** Axial displacement of the trap site and corresponding defocus during the optical tweezers characterisation for a fibre with length 150 mm.

the one obtained at room temperature ($T = 21.84\,^{\circ}\mathrm{C}$) we found that, to generate the same distal FP modes, the proximal far-field is modified by a quadratic phase – a defocus – with magnitude proportional to the temperature difference. Figure 5.13 a shows this phase difference, averaged for all distal FPs in each measurement of the TM, and compares it with a fitted quadratic phase. Figure 5.13 b shows that the dependence of averaged defocus with temperature is very linear, having a slope of $\approx 0.19\lambda/^{\circ}\mathrm{C}$ for the fibre length used. A temperature increase can therefore be compensated to some extent by applying a defocus on the proximal field, without the need for re-measuring the TM. Conversely, if we retain the same TM measurement without modifying the proximal field, such defocus will manifest itself in the distal field as an axial displacement of the FP modes generated.

In order to link the defocus due to power absorption with the temperature increase, a study of the axial displacement of a confined particle as a function of the optical power was conducted using a fibre of similar length (150 mm). This dependence, shown in Fig. 5.13 c, is also very linear with a slope of $\approx 0.065\lambda/\mathrm{mW}$. Although the temperature is not distributed uniformly along the fibre, these two studies gave us a coarse estimate that the fibre temperature increases by $\approx 0.3\,^{\circ}\mathrm{C}$ per mW, for the fibre length used.

5.8 Conclusions

The presented in this chapter work is the first demonstration of three – dimensional holographic optical manipulation of micro-objects via a single-core optical fibre. Developed by our collaborators from Max Planck Institute for the Science of Light a new class of all-solid step-index multimode fibres has been introduced, which feature a previously unattainable level of NA, exceeding the value of 0.8, necessary for stable optical confinement of silica particles. Novel high-NA fibres required adapted holographic algorithms that, by taking the mode-dependent loss into account, enable harnessing the available NA almost completely. Moreover, these application-customised approaches enable positioning of multiple foci independently of one another, with nanometric precision in all three dimensions. The combination of novel fibres and the empowered algorithms therefore significantly enhanced our ability to deliver tightly focussed laser beams into difficult-to-access locations.

The versatility of the new instrument is demonstrated by simultaneous and dynamic 3D manipulation of large assemblies of dielectric microparticles. The instrument's footprint can be as small as 35 µm in diameter, allowing us to demonstrate the manipulation of micro-objects within a turbid cavity, inaccessible to bulk optics. Quantitative analyses reveal that the performance of the fibre based trapping system is not significantly lower than standard geometries of optical tweezers relying on bulk objective lenses. Particle confinement strength and fine positioning control are both well maintained, which suggest that the system is applicable without severe compromises. Other possible concerns might relate to the influence of fibre bending on the quality of resulting optical traps. A phenomenological demonstration of this effect, shown in Sec. 5.7.1, suggests that the resilience of the fibres is sufficient for a wide spectrum of practical applications, including in vivo experiments. Furthermore, it has been recently demonstrated that such deformations can be corrected for with the use of numerical modelling of light propagation through multimode fibres [33]. This same study also suggests that highly precise numerical modelling can substitute the process of TM acquisition, which can significantly simplify the currently complex experimental methods.

The work opens up new perspectives for the first applications of HOT inside complex environments, excitingly including in vivo studies, which so far has only been applied in optically transparent or easily accessible tissues [131–133]. Manipulating optical traps in three dimensions is a vitally important attribute in such applications, because alternative means of mutually positioning

the optical traps with respect to the sample (e.g. by the piezo-actuated stages commonly used in vitro) is no longer feasible.

Finally, the work is broadly relevant beyond the applications of HOT. In the scope of techniques demonstrated in Sec. 1-4, it opens a direct route to implementation of high resolution in vivo imaging deep inside living tissues.

Chapter 6

Conclusions

This manuscript guides the reader through the main technical and methodological aspects of the high-speed implementation of holographic endoscopy through a single multimode fibre probe. Building up on the previous activity of the group, it addresses emerging challenges of the research community, including high-speed beam shaping, in-vivo validation of multimode fibre-based endoscopy as well as high-resolution imaging through the fibres.

When considering imaging applications, and particularly those relying on the raster scanning of a laser focus inside or behind a complex medium, the refresh rate of spatial light modulator becomes a vitally important attribute. Almost all techniques in complex photonics have been initially demonstrated using liquid crystal based modulators, as convenient device allowing for direct phase modulation. However, having low refresh rates, acquisition of a single frame containing a few kilopixels of data typically takes several minutes, it can therefore not keep up with emerging needs of imaging applications. This reason explains the recent interest in digital micromirror devices with high light modulation rates, which are several orders of magnitude higher than those of liquid crystal based modulators.

Although the enhanced modulation rate comes at the expense of optical efficiency, which is significantly lower than for LC-SLMs, it could be easily compensated with higher laser power. The collaboration with Kevin Mitchell, Miles Padget, and David Phillips from Glasgow University, who already for many years have been utilising DMDs in single-pixel cameras, significantly accelerated adopting the main principles of controlling these devices and in the period of one year perform two different studies. First of all, we have demonstrated the dynamic spatial control of light fields, utilising a DMD for generation of vector beams with spatially controllable intensity, phase and polarisation and their rapid switching at the maximum refresh rate of the DMD. This fact combined with the relatively low price makes DMDs promising candidates for implementation of multimode fibre based imaging as well as for a

number of the other biophotonic applications, including microscopy and optical micro-manipulation. Moreover, ustilising DMD in the scheme of polarisation control, which was for the time demonstrated by Martin Plöschner, Tomáš Tyc and Tomáš Čižmár on a liquid-crystal-based modulator, for predition of transformation matrix, this can provide technical means for achiving flexible operation of MMF-based endoscopes.

Another study aimed to extend high-speed modulation towards the complex environment and carefully compare its performance with a liquid crystal device. Surprisingly, the obtained results reveal that light-modulation fidelity achieved by a MEMS-based device is not compromised by its inherent limitation of binary amplitude modulation regime if applied in an off-axis regime. Moreover, additional features such as scattering- and flicker-free operation are shown to provide quality enhancement of wavefront shaping, showing the significantly higher contrast of generated foci. This makes DMDs even more appealing for the imaging applications.

Working closely together with the Tristan Altwegg-Boussac, Janelle Pakan and Nathalie Rochefort from the University of Edinburgh, recognised experts in the discipline of in-vivo imaging, we optimised the experimental designs under the requirements of the particular activity of our mutual interest: observation of neuronal cells in deep regions of visual cortex and hippocampus within a living animal model. We have, wrapped the previously tested high-fidelity wavefront-shaping approach in a compact design, in order to achieve, so far, the best performance in fibre imaging available in vivo. As a result, the system allowed imaging neuronal somata as well as processes deep inside the brain of living animal model using a bare optical fibre having a footprint as small as 60 μm in diameter, which is an order of magnitude smaller when compared to currently used approaches based on GRIN lenses or fibre bundles.

This experiment is the quintessence of the entire work of the candidate and a certain checkpoint in the development of the technology. For the first time, holographic microendoscopy fulfilled a number of its main promises (claimed advantages) simultaneously in one experiment, demonstrating such qualities as the resolution limited only by the numerical aperture of the fiber, pureness of the focal points reaching theoretically possible values for phase-only holography, the scanning speed at the maximum of the fastest available spatial light modulator and finally the minimal invasiveness in in-vivo applications. Although achieved via the most primitive imaging modality, these results thus

demonstrate the readiness of holographic endoscopy to be used in highly specialised studies of neuronal cells and the connectivity of neuronal circuits.

Certainly, such specialised studies will require equally specialised fibre probes, with optimised numerical aperture and core size, which simply do not exist at the moment. Future advances on the applicational side depend heavily on the development of specialty fibres that will meet not only the requirements of applications but also take into account existing technical limitations. For example, pushed to the limit of the DMD, the trade-off between the size of the field of view and the scanning rates is still far from the speed of traditional scanning microscopic techniques.

As for the further evolution of the technology, there is a clear trend in the minimally-invasive introduction of more complicated biophotonic techniques through the fibre or fibre assemblies. The focusing power of commercially available MMFs has however never been sufficient to support some of the most advanced imaging and biomedical approaches, which rely on extremely tight focusing of light.

The idea of increasing the numerical aperture of fibres is neither novel nor limited to applications in holographic endoscopy. This may sound paradoxical, but the simplest and most effective way to obtain very high numerical apertures is a microstructured fibre, where the light-guiding core is surrounded by an air cladding, which significantly increases the refractive index contrast. However, the contact of such fibres with tissues instantly leads to the filling of holes and a decrease in the effective refractive index.

Teaming-up with the world-known leaders in fibre development - the group of Philip St. J. Russell from the Max Planck Institute for the Science of Light, allowed us to design, manufacture and utilise an ultra-high NA, but at the same time solid-core fibre, which was specifically tailored for advanced bio-photonics applications. The new fibre designs have brought eminent enhancement of the numerical aperture, approaching the focusing power of the best water-immersive physiology objectives.

Application of the novel fibres in holographic geometries came with new challenges. In structures with such a high refractive index contrast, higher spatial frequencies suffer from strong losses, in fact, they are effectively leaking out already at the distance of few centimetres. Introduction of adapted beam-shaping methods and experimental designs allowed to substantially compensate for this effect at the cost of optical power. In the future, the solution could be also found in the implementation of mode-mixers, which provide redistribution of the guided power between the fibre modes.

Utilising compensation algorithm allowed not only to demonstrate for the first time three-dimensional holographic optical manipulation of arrays of micro-particles, with active and precise control of their positions but to prove its applicability in optically complex environments. These results demonstrate significant broadening of the applicability of holographic endoscopy and pave the way to minimally-invasive implementation of optical manipulation.

It is also important to highlight the simple applicability tests conducted within this work, which mimic possible problems arising in real applications. Although the results were shown in the framework of the trapping experiments, they are equally relevant and indicative for the other application of holographic endoscopy. For example, the demonstrated resilience of the probe to a small displacement of the distal end opens the possibility of using hard fibre endoscopes not only for anaesthetised but also for immobilised animals, where motion artefacts are the most crucial technical hurdles in the way of such experiments, which prevent advanced behavioural studies. Moreover, heating of the probe, which is unavoidable in in-vivo applications, since the body temperature of animal models is usually higher than the surrounding environment, only leads to a change in the focal distance of endoscopic probe, which can be corrected for on the fly by holographic methods.

Overall, the work presented in the thesis opens new exciting perspectives for other advanced techniques of modern microscopy including multiphoton, super-resolution or volumetric techniques to be implemented in-vivo as well as for extending the possible application of holographic endoscopy beyond imaging purposes.

The seven-year history of the MMF based imaging development has brought a significant variety of demonstrated microscopic techniques and even the first successes in observations in vivo. The number of papers published in the last two years by groups new to the topic shows a growing popularity of this subject in the field of photonics.

However, the dream of turning this concept into a versatile imaging tool for modern biology, like any other interdisciplinary attempts, is impossible without interest and participation from the other side. The current level of technology is already sufficient for implementation in, even if only simple, but real biological studies. Such attempts will allow developing practical engineering solutions, which is usually conceived as the most lengthy and difficult step in technology translation. Moreover, real applications will also provide a feedback for adjusting the priorities for further development.

Considering neuroscience as one of the most promising application area for

ultra-minimally-invasive endoscopy, it is worth paying attention to the application of competitive solutions, already applied in the field. For example, the signal processing in the brain of awake head-restrained animals or developmental studies, where animals with implanted microendoscopes are observed periodically for a long time. The addressing of such problems is already possible with the use of fibres, but require the development of purely engineering solutions for automatic alignment of the position of the optical system with respect to the fibre, which can be done computationally on the side of the SLM, without any mechanical adjustments in the system.

The popularity of portable, head-fixed miniature microscopes with hundreds of applications in the real neuroscience experiments on imaging and optogenetics [140] as well as with the successful start-up company (Inscopix) focused on their production, show a particularly keen interest in studying the dynamics of neuronal networks in freely moving animals.

This is perhaps one of the most potentially interesting applications of fibre endoscopy in neuroscience, since it allows to overcome resolution limitations of the above-mentioned competitor and there is no need for any relatively heavy and bulky scanning and recording devices attached to the head of the animal, which will simplify the implementation and further minimise motion artefacts as well as the effect on the behaviour of the animal.

The approaches for active bending compensation and developing the probes with sufficient bending resilience, already mentioned in this manuscript recently demonstrated the capability of flexible operation of holographic microendoscopes. Further progress towards practical implementation of these ideas relies on the development of the fast algorithm for on-the-flight correction of the transformation matrix.

The footprint minimisation, at the same time, comes at a cost of a field of view, which in the demonstrated approach limited by the core size. Therefore, the developed concept might be especially promising for studies of structural and functional properties of individual cells and require high-resolution imaging. A good example of this kind of application are studies of long-term structural dynamics of submicron formations such as neuronal processes [141–144], which, for example, hold the key for the understanding of brain plasticity and revealing the cellular mechanisms of learning and memory. An additional direction in potential applications could be found in so-called functional imaging, which allows studying of signal processing and may greatly benefit from the high acquisition rates demonstrated in this work. The demonstrated

scanning speed of about 23 kHz and the ability of random access to any pre-calibrated focal points provides a means to study the dynamics of calcium ions in dendrites and synaptic buttons as well as excitatory synaptic transmission at single synapses [145–150].

Additionally, it is necessary to emphasise the research on implementation of volumetric imaging techniques in fibre modalities, which would extend an applicability of the concept to studies of dynamics in neural circuits. Moreover, such studies not only require access to branched in three-dimensional space cell structures but also necessitate a sufficiently high speed of image interrogation, which could not be achieved through the fibre in a traditional way of optical sectioning, due to the limited speed of available light modulators.

Bibliography

1. Čižmár, T. Exploiting multimode waveguides for in vivo imaging. *SPIE Newsroom,* Published online DOI: 10.1117/2.1201509.006106 (2015).
2. Bolin, F. P., Preuss, L. E., Taylor, R. C. & Ference, R. J. Refractive index of some mammalian tissues using a fiber optic cladding method. *Applied optics* **28,** 2297–2303 (1989).
3. Tearney, G. *et al.* Determination of the refractive index of highly scattering human tissue by optical coherence tomography. *Optics letters* **20,** 2258–2260 (1995).
4. Helmchen, F. & Denk, W. Deep tissue two-photon microscopy. *Nature methods* **2,** 932 (2005).
5. Ntziachristos, V. *Going deeper than microscopy: the optical imaging frontier in biology* 2010.
6. Favre-Bulle, I. A. *et al.* Scattering of sculpted light in intact brain tissue, with implications for optogenetics. *Scientific reports* **5,** 11501 (2015).
7. Jacques, S. L. Optical properties of biological tissues: a review. *Physics in Medicine & Biology* **58,** R37 (2013).
8. Horton, N. G. *et al.* In vivo three-photon microscopy of subcortical structures within an intact mouse brain. *Nature photonics* **7,** 205 (2013).
9. Mosk, A. P., Lagendijk, A., Lerosey, G. & Fink, M. Controlling waves in space and time for imaging and focusing in complex media. *Nature photonics* **6,** 283 (2012).
10. Vellekoop, I. M. & Mosk, A. Focusing coherent light through opaque strongly scattering media. *Optics letters* **32,** 2309–2311 (2007).
11. Vellekoop, I. M. & Mosk, A. Universal optimal transmission of light through disordered materials. *Physical review letters* **101,** 120601 (2008).
12. Conkey, D. B., Brown, A. N., Caravaca-Aguirre, A. M. & Piestun, R. Genetic algorithm optimization for focusing through turbid media in noisy environments. *Optics express* **20,** 4840–4849 (2012).

13. Cui, M. & Yang, C. Implementation of a digital optical phase conjugation system and its application to study the robustness of turbidity suppression by phase conjugation. *Optics express* **18,** 3444–3455 (2010).

14. Papadopoulos, I. N., Farahi, S., Moser, C. & Psaltis, D. Focusing and scanning light through a multimode optical fiber using digital phase conjugation. *Optics express* **20,** 10583–10590 (2012).

15. Drémeau, A. *et al.* Reference-less measurement of the transmission matrix of a highly scattering material using a DMD and phase retrieval techniques. *Optics express* **23,** 11898–11911 (2015).

16. Popoff, S., Lerosey, G., Fink, M., Boccara, A. C. & Gigan, S. Image transmission through an opaque material. *Nature communications* **1,** 81 (2010).

17. Popoff, S. *et al.* Measuring the transmission matrix in optics: an approach to the study and control of light propagation in disordered media. *Physical review letters* **104,** 100601 (2010).

18. Čižmár, T., Mazilu, M. & Dholakia, K. In situ wavefront correction and its application to micromanipulation. *Nature Photonics* **4,** 388 (2010).

19. Bertolotti, J. *et al.* Non-invasive imaging through opaque scattering layers. *Nature* **491,** 232 (2012).

20. Katz, O., Small, E., Bromberg, Y. & Silberberg, Y. Focusing and compression of ultrashort pulses through scattering media. *Nature photonics* **5,** 372 (2011).

21. Xu, X., Liu, H. & Wang, L. V. Time-reversed ultrasonically encoded optical focusing into scattering media. *Nature photonics* **5,** 154 (2011).

22. Judkewitz, B., Wang, Y. M., Horstmeyer, R., Mathy, A. & Yang, C. Speckle-scale focusing in the diffusive regime with time reversal of variance-encoded light (TROVE). *Nature photonics* **7,** 300 (2013).

23. Di Leonardo, R. & Bianchi, S. Hologram transmission through multimode optical fibers. *Optics express* **19,** 247–254 (2011).

24. Bianchi, S. & Di Leonardo, R. A multi-mode fiber probe for holographic micromanipulation and microscopy. *Lab on a Chip* **12,** 635–639 (2012).

25. Čižmár, T. & Dholakia, K. Shaping the light transmission through a multimode optical fibre: complex transformation analysis and applications in biophotonics. *Optics Express* **19,** 18871–18884 (2011).

26. Čižmár, T. & Dholakia, K. Exploiting multimode waveguides for pure fibre-based imaging. *Nature communications* **3,** 1027 (2012).

27. Choi, Y. *et al.* Scanner-free and wide-field endoscopic imaging by using a single multimode optical fiber. *Physical review letters* **109,** 203901 (2012).

28. Papadopoulos, I. N., Farahi, S., Moser, C. & Psaltis, D. High-resolution, lensless endoscope based on digital scanning through a multimode optical fiber. *Biomedical optics express* **4,** 260–270 (2013).

29. Morales-Delgado, E. E., Psaltis, D. & Moser, C. Two-photon imaging through a multimode fiber. *Optics express* **23,** 32158–32170 (2015).

30. Mahalati, R. N., Gu, R. Y. & Kahn, J. M. Resolution limits for imaging through multi-mode fiber. *Optics express* **21,** 1656–1668 (2013).

31. Caravaca-Aguirre, A. M., Niv, E., Conkey, D. B. & Piestun, R. Real-time resilient focusing through a bending multimode fiber. *Optics express* **21,** 12881–12887 (2013).

32. Farahi, S., Ziegler, D., Papadopoulos, I. N., Psaltis, D. & Moser, C. *Optics express* **21,** 22504–22514 (2013).

33. Plöschner, M., Tyc, T. & Čižmár, T. Seeing through chaos in multimode fibres. *Nature Photonics* **9,** 529 (2015).

34. Plöschner, M, Straka, B, Dholakia, K & Čižmár, T. GPU accelerated toolbox for real-time beam-shaping in multimode fibres. *Optics express* **22,** 2933–2947 (2014).

35. Plöschner, M. & Čižmár, T. Compact multimode fiber beam-shaping system based on GPU accelerated digital holography. *Optics letters* **40,** 197–200 (2015).

36. Armitage, D., Underwood, I. & Wu, S.-T. *Introduction to microdisplays* (John Wiley & Sons, 2006).

37. Solgaard, O. *Photonic microsystems: Micro and nanotechnology applied to optical devices and systems* (Springer Science & Business Media, 2009).

38. Lueder, E. *Liquid crystal displays: addressing schemes and electro-optical effects* (John Wiley & Sons, 2010).

39. Maurer, C., Schwaighofer, A., Jesacher, A., Bernet, S. & Ritsch-Marte, M. Suppression of undesired diffraction orders of binary phase holograms. *Applied optics* **47,** 3994–3998 (2008).

40. Pezzaniti, J. & Chipman, R. Phase-only modulation of a twisted nematic liquid-crystal TV by use of the eigenpolarization states. *Optics letters* **18,** 1567–1569 (1993).

41. Davis, J. A., Moreno, I. & Tsai, P. Polarization eigenstates for twisted-nematic liquid-crystal displays. *Applied optics* **37,** 937–945 (1998).

42. Glückstad, J. *Measurement results on the PAL-SLM* in *Meeting at Hamamatsu Photonics* (2001).

43. Melcher, R. L. LCoS-Microdisplay technology and applications-LCoS is emerging as the most attractive technology choice for a wide variety of portable-and projection-display applications. *Information Display* **16,** 20–23 (2000).

44. Gad-el Hak, M & Seemann, W. *The MEMS handbook* (CRC press, 2001).

45. Amm, D. & Corrigan, R. *5.2: Grating light valve^{TM} technology: update and novel applications* in *SID Symposium Digest of Technical Papers* **29** (1998), 29–32.

46. Knipe, R. L. *Challenges of a digital micromirror device: modeling and design* in *Micro-optical Technologies for Measurement, Sensors, and Microsystems* **2783** (1996), 135–146.

47. Tyson, R. *Principles of adaptive optics* (CRC press, 2010).

48. Rai-Choudhury, P. *MEMS and MOEMS Technology and Applications* (Spie Press, 2000).

49. López, D *et al. Two-dimensional MEMS array for maskless lithography and wavefront modulation* in *Smart Sensors, Actuators, and MEMS III* **6589** (2007), 65890S.

50. Lapisa, M., Zimmer, F., Niklaus, F., Gehner, A. & Stemme, G. *CMOS-integrable piston-type micro-mirror array for adaptive optics made of monocrystalline silicon using 3-D integration* in *Micro Electro Mechanical Systems, 2009. MEMS 2009. IEEE 22nd International Conference on* (2009), 1007–1010.

51. Papadopoulos, I. N., Farahi, S., Moser, C. & Psaltis, D. High-resolution, lensless endoscope based on digital scanning through a multimode optical fiber. *Biomedical optics express* **4,** 260–270 (2013).

52. Brown, B. R. & Lohmann, A. W. Complex spatial filtering with binary masks. *Applied Optics* **5,** 967–969 (1966).

53. Chandrasekaran, S. N., Ligtenberg, H., Steenbergen, W. & Vellekoop, I. M. Using digital micromirror devices for focusing light through turbid media. **8979,** 897905 (2014).

54. Conkey, D. B., Caravaca-Aguirre, A. M. & Piestun, R. High-speed scattering medium characterization with application to focusing light through turbid media. *Optics express* **20,** 1733–1740 (2012).

55. Goorden, S. A., Bertolotti, J. & Mosk, A. P. Superpixel-based spatial amplitude and phase modulation using a digital micromirror device. *Optics express* **22,** 17999–18009 (2014).

56. Akbulut, D., Huisman, T. J., van Putten, E. G., Vos, W. L. & Mosk, A. P. Focusing light through random photonic media by binary amplitude modulation. *Optics express* **19,** 4017–4029 (2011).

57. Yaroslavsky, A. *et al.* Optical properties of selected native and coagulated human brain tissues in vitro in the visible and near infrared spectral range. *Physics in Medicine & Biology* **47,** 2059 (2002).

58. Kleinfeld, D., Mitra, P. P., Helmchen, F. & Denk, W. Fluctuations and stimulus-induced changes in blood flow observed in individual capillaries in layers 2 through 4 of rat neocortex. *Proceedings of the National Academy of Sciences* **95,** 15741–15746 (1998).

59. Oheim, M., Beaurepaire, E., Chaigneau, E., Mertz, J. & Charpak, S. Two-photon microscopy in brain tissue: parameters influencing the imaging depth. *Journal of neuroscience methods* **111,** 29–37 (2001).

60. Denk, W., Strickler, J. H. & Webb, W. W. Two-photon laser scanning fluorescence microscopy. *Science* **248,** 73–76 (1990).

61. Kerr, J. N. & Denk, W. Imaging in vivo: watching the brain in action. *Nature Reviews Neuroscience* **9,** 195 (2008).

62. Stosiek, C., Garaschuk, O., Holthoff, K. & Konnerth, A. In vivo two-photon calcium imaging of neuronal networks. *Proceedings of the National Academy of Sciences* **100,** 7319–7324 (2003).

63. Mascaro, A. A. *et al. Multiphoton microscopy in brain imaging* in *Multiphoton Microscopy in the Biomedical Sciences XV* **9329** (2015), 932903.

64. Albert, O, Sherman, L, Mourou, G, Norris, T. & Vdovin, G. Smart microscope: an adaptive optics learning system for aberration correction in multiphoton confocal microscopy. *Optics letters* **25,** 52–54 (2000).

65. Booth, M. J., Neil, M. A., Juškaitis, R. & Wilson, T. Adaptive aberration correction in a confocal microscope. *Proceedings of the National Academy of Sciences* **99,** 5788–5792 (2002).

66. Sherman, L, Ye, J., Albert, O & Norris, T. Adaptive correction of depth-induced aberrations in multiphoton scanning microscopy using a deformable mirror. *Journal of microscopy* **206,** 65–71 (2002).

67. Wright, A. *et al.* Adaptive optics for enhanced signal in CARS microscopy. *Optics express* **15,** 18209–18219 (2007).

68. Beaurepaire, E, Oheim, M & Mertz, J. Ultra-deep two-photon fluorescence excitation in turbid media. *Optics Communications* **188,** 25–29 (2001).

69. Theer, P., Hasan, M. T. & Denk, W. Two-photon imaging to a depth of 1000 μm in living brains by use of a Ti: Al 2 O 3 regenerative amplifier. *Optics letters* **28,** 1022–1024 (2003).

70. Chu, S.-W. *et al.* Multimodal nonlinear spectral microscopy based on a femtosecond Cr: forsterite laser. *Optics letters* **26,** 1909–1911 (2001).

71. Liu, T.-M. *et al.* Multiphoton confocal microscopy using a femtosecond Cr: forsterite laser. *Scanning* **23,** 249–254 (2001).

72. Squirrell, J. M., Wokosin, D. L., White, J. G. & Bavister, B. D. Long-term two-photon fluorescence imaging of mammalian embryos without compromising viability. *Nature biotechnology* **17,** 763 (1999).

73. Jung, J. C. & Schnitzer, M. J. Multiphoton endoscopy. *Optics letters* **28,** 902–904 (2003).

74. Jung, J. C., Mehta, A. D., Aksay, E., Stepnoski, R. & Schnitzer, M. J. In vivo mammalian brain imaging using one-and two-photon fluorescence microendoscopy. *Journal of neurophysiology* **92,** 3121–3133 (2004).

75. Levene, M. J., Dombeck, D. A., Kasischke, K. A., Molloy, R. P. & Webb, W. W. In vivo multiphoton microscopy of deep brain tissue. *Journal of neurophysiology* **91,** 1908–1912 (2004).

76. Deisseroth, K. *et al.* Next-Generation Optical Technologies for Illuminating Genetically Targeted Brain Circuits. *Journal of Neuroscience* **26,** 10380–10386 (2006).

77. Murayama, M., Pérez-Garci, E., Lüscher, H.-R. & Larkum, M. E. Fiberoptic system for recording dendritic calcium signals in layer 5 neocortical pyramidal cells in freely moving rats. *Journal of neurophysiology* **98,** 1791–1805 (2007).

78. Murayama, M. *et al.* Dendritic encoding of sensory stimuli controlled by deep cortical interneurons. *Nature* **457,** 1137 (2009).

79. Llewellyn, M. E., Barretto, R. P., Delp, S. L. & Schnitzer, M. J. Minimally invasive high-speed imaging of sarcomere contractile dynamics in mice and humans. *Nature* **454,** 784 (2008).

80. Flusberg, B. A. *et al.* High-speed, miniaturized fluorescence microscopy in freely moving mice. *Nature methods* **5,** 935 (2008).

81. Knittel, J., Schnieder, L., Buess, G., Messerschmidt, B & Possner, T. Endoscope-compatible confocal microscope using a gradient index-lens system. *Optics Communications* **188,** 267–273 (2001).

82. Fu, L. & Gu, M. Fibre-optic nonlinear optical microscopy and endoscopy. *Journal of microscopy* **226,** 195–206 (2007).

83. Engelbrecht, C. J., Johnston, R. S., Seibel, E. J. & Helmchen, F. Ultra-compact fiber-optic two-photon microscope for functional fluorescence imaging in vivo. *Optics express* **16,** 5556–5564 (2008).

84. Wilt, B. A. *et al.* Advances in light microscopy for neuroscience. *Annual review of neuroscience* **32,** 435–506 (2009).

85. Flusberg, B. A., Jung, J. C., Cocker, E. D., Anderson, E. P. & Schnitzer, M. J. In vivo brain imaging using a portable 3.9 gram two-photon fluorescence microendoscope. *Optics letters* **30,** 2272–2274 (2005).

86. Göbel, W., Kerr, J. N., Nimmerjahn, A. & Helmchen, F. Miniaturized two-photon microscope based on a flexible coherent fiber bundle and a gradient-index lens objective. *Optics letters* **29,** 2521–2523 (2004).

87. Hoy, C. L. *et al.* Miniaturized probe for femtosecond laser microsurgery and two-photon imaging. *Optics express* **16,** 9996–10005 (2008).

88. Jung, W. *et al.* Miniaturized probe based on a microelectromechanical system mirror for multiphoton microscopy. *Optics letters* **33,** 1324–1326 (2008).

89. Le Harzic, R, Weinigel, M, Riemann, I, König, K & Messerschmidt, B. Nonlinear optical endoscope based on a compact two axes piezo scanner and a miniature objective lens. *Optics express* **16,** 20588–20596 (2008).

90. Rector, D. & Harper, R. Imaging of hippocampal neural activity in freely behaving animals. *Behavioural brain research* **42,** 143–149 (1991).

91. Rector, D., Poe, G. & Harper, R. Imaging of hippocampal and neocortical neural activity following intravenous cocaine administration in freely behaving cats. *Neuroscience* **54,** 633–641 (1993).

92. Ozbay, B. N. *et al.* Miniaturized fiber-coupled confocal fluorescence microscope with an electrowetting variable focus lens using no moving parts. *Optics letters* **40,** 2553–2556 (2015).

93. Szabo, V., Ventalon, C., De Sars, V., Bradley, J. & Emiliani, V. Spatially selective holographic photoactivation and functional fluorescence imaging in freely behaving mice with a fiberscope. *Neuron* **84,** 1157–1169 (2014).

94. Engelbrecht, C. J., Voigt, F. & Helmchen, F. Miniaturized selective plane illumination microscopy for high-contrast in vivo fluorescence imaging. *Optics letters* **35,** 1413–1415 (2010).

95. Katz, O., Heidmann, P., Fink, M. & Gigan, S. Non-invasive single-shot imaging through scattering layers and around corners via speckle correlations. *Nature photonics* **8,** 784 (2014).

96. Gissibl, T., Thiele, S., Herkommer, A. & Giessen, H. Two-photon direct laser writing of ultracompact multi-lens objectives. *Nature Photonics* **10,** 554 (2016).

97. Vasquez-Lopez, S. A. *et al.* Minimally invasive deep-brain imaging through a 50 μm-core multimode fibre. *bioRxiv,* 289793 (2018).

98. Ghanavati, S., Lisa, X. Y., Lerch, J. P. & Sled, J. G. A perfusion procedure for imaging of the mouse cerebral vasculature by X-ray micro-CT. *Journal of neuroscience methods* **221,** 70–77 (2014).

99. Claverol-Tinture, E. & Nadasdy, Z. Intersection of microwire electrodes with proximal CA1 stratum-pyramidale neurons at insertion for multiunit recordings predicted by a 3-D computer model. *IEEE transactions on biomedical engineering* **51,** 2211–2216 (2004).

100. Loterie, D. *et al.* Digital confocal microscopy through a multimode fiber. *Optics express* **23,** 23845–23858 (2015).

101. Plöschner, M. *et al.* Multimode fibre: Light-sheet microscopy at the tip of a needle. *Scientific reports* **5,** 18050 (2015).

102. Flaes, D. E. B. *et al.* Robustness of Light-Transport Processes to Bending Deformations in Graded-Index Multimode Waveguides. *Physical Review Letters* **120,** 233901 (2018).

103. Lee, W.-H. Binary computer-generated holograms. *Applied Optics* **18,** 3661–3669 (1979).

104. Maurer, C., Jesacher, A., Fürhapter, S., Bernet, S. & Ritsch-Marte, M. Tailoring of arbitrary optical vector beams. *New Journal of Physics* **9,** 78 (2007).

105. Dorn, R., Quabis, S & Leuchs, G. Sharper focus for a radially polarized light beam. *Physical review letters* **91,** 233901 (2003).

106. Allen, L., Beijersbergen, M. W., Spreeuw, R. & Woerdman, J. Orbital angular momentum of light and the transformation of Laguerre-Gaussian laser modes. *Physical Review A* **45,** 8185 (1992).

107. Marrucci, L., Manzo, C & Paparo, D. Optical spin-to-orbital angular momentum conversion in inhomogeneous anisotropic media. *Physical review letters* **96,** 163905 (2006).

108. Galvez, E. *et al.* Geometric phase associated with mode transformations of optical beams bearing orbital angular momentum. *Physical review letters* **90,** 203901 (2003).

109. Dyment, J. Hermite-Gaussian Mode Patterns in GaAs Junction Lasers. *Applied Physics Letters* **10,** 84–86 (1967).

110. Radwell, N, Hawley, R., Götte, J. & Franke-Arnold, S. Achromatic vector vortex beams from a glass cone. *Nature communications* **7,** 10564 (2016).

111. Courtial, J. Self-imaging beams and the Guoy effect. *Optics communications* **151,** 1–4 (1998).

112. García-Márquez, J., López, V., González-Vega, A. & Noé, E. Flicker minimization in an LCoS spatial light modulator. *Optics express* **20,** 8431–8441 (2012).

113. Mitchell, K. J., Turtaev, S., Padgett, M. J., Čižmár, T. & Phillips, D. B. High-speed spatial control of the intensity, phase and polarisation of vector beams using a digital micro-mirror device. *Optics express* **24,** 29269–29282 (2016).

114. Vellekoop, I. M., Lagendijk, A. & Mosk, A. Exploiting disorder for perfect focusing. *Nature photonics* **4,** 320 (2010).

115. Sharp, A. A., Ortega, A. M., Restrepo, D., Curran-Everett, D. & Gall, K. In vivo penetration mechanics and mechanical properties of mouse brain tissue at micrometer scales. *IEEE Transactions on Biomedical Engineering* **56,** 45–53 (2009).

116. Kozai, T. D., Jaquins-Gerstl, A. S., Vazquez, A. L., Michael, A. C. & Cui, X. T. Brain tissue responses to neural implants impact signal sensitivity and intervention strategies. *ACS chemical neuroscience* **6,** 48–67 (2015).

117. Kozai, T. *et al.* Reduction of neurovascular damage resulting from microelectrode insertion into the cerebral cortex using in vivo two-photon mapping. *Journal of neural engineering* **7,** 046011 (2010).

118. Seymour, J. P. & Kipke, D. R. Neural probe design for reduced tissue encapsulation in CNS. *Biomaterials* **28,** 3594–3607 (2007).

119. Buzsáki, G. *et al.* Tools for probing local circuits: high-density silicon probes combined with optogenetics. *Neuron* **86,** 92–105 (2015).

120. Attardo, A., Fitzgerald, J. E. & Schnitzer, M. J. Impermanence of dendritic spines in live adult CA1 hippocampus. *Nature* **523,** 592 (2015).

121. Sato, M., Kawano, M., Yanagawa, Y. & Hayashi, Y. In vivo two-photon imaging of striatal neuronal circuits in mice. *Neurobiology of learning and memory* **135,** 146–151 (2016).

122. Tsai, P. S. *et al.* Correlations of neuronal and microvascular densities in murine cortex revealed by direct counting and colocalization of nuclei and vessels. *Journal of Neuroscience* **29,** 14553–14570 (2009).

123. Johnson, M. D., Langhals, N. B. & Kipke, D. R. *Neural interface dynamics following insertion of hydrous iridium oxide microelectrode arrays* in *Engineering in Medicine and Biology Society, 2006. EMBS'06. 28th Annual International Conference of the IEEE* (2006), 3178–3181.

124. Szarowski, D. *et al.* Brain responses to micro-machined silicon devices. *Brain research* **983,** 23–35 (2003).

125. Turner, J. *et al.* Cerebral astrocyte response to micromachined silicon implants. *Experimental neurology* **156,** 33–49 (1999).

126. Grill, W. M., Norman, S. E. & Bellamkonda, R. V. Implanted neural interfaces: biochallenges and engineered solutions. *Annual review of biomedical engineering* **11,** 1–24 (2009).

127. Zhang, S., Boyd, J., Delaney, K. & Murphy, T. H. Rapid reversible changes in dendritic spine structure in vivo gated by the degree of ischemia. *Journal of Neuroscience* **25,** 5333–5338 (2005).

128. House, P. A., MacDonald, J. D., Tresco, P. A. & Normann, R. A. Acute microelectrode array implantation into human neocortex: preliminary technique and histological considerations. *Neurosurgical focus* **20,** 1–4 (2006).

129. Johnson, M. D., Kao, O. E. & Kipke, D. R. Spatiotemporal pH dynamics following insertion of neural microelectrode arrays. *Journal of neuroscience methods* **160,** 276–287 (2007).

130. Bjornsson, C. *et al.* Effects of insertion conditions on tissue strain and vascular damage during neuroprosthetic device insertion. *Journal of neural engineering* **3,** 196 (2006).

131. Zhong, M.-C., Wei, X.-B., Zhou, J.-H., Wang, Z.-Q. & Li, Y.-M. Trapping red blood cells in living animals using optical tweezers. *Nature communications* **4,** 1768 (2013).

132. Johansen, P. L., Fenaroli, F., Evensen, L., Griffiths, G. & Koster, G. Optical micromanipulation of nanoparticles and cells inside living zebrafish. *Nature communications* **7,** 10974 (2016).

133. Bambardekar, K., Clément, R., Blanc, O., Chardès, C. & Lenne, P.-F. Direct laser manipulation reveals the mechanics of cell contacts in vivo. *Proceedings of the National Academy of Sciences* **112,** 1416–1421 (2015).

134. Amitonova, L. V. *et al.* High-resolution wavefront shaping with a photonic crystal fiber for multimode fiber imaging. *Optics letters* **41,** 497–500 (2016).

135. Issa, N. A. High numerical aperture in multimode microstructured optical fibers. *Applied Optics* **43,** 6191–6197 (2004).

136. Ho, K.-P. & Kahn, J. M. Mode-dependent loss and gain: statistics and effect on mode-division multiplexing. *Optics express* **19,** 16612–16635 (2011).

137. Neuman, K. C. & Block, S. M. Optical trapping. *Review of scientific instruments* **75,** 2787–2809 (2004).

138. Dholakia, K. & Reece, P. Optical micromanipulation takes hold. *Nano today* **1,** 18–27 (2006).

139. Kislin, M. *et al.* Flat-floored air-lifted platform: a new method for combining behavior with microscopy or electrophysiology on awake freely moving rodents. *Journal of visualized experiments: JoVE* (2014).

140. Fenno, L., Yizhar, O. & Deisseroth, K. The development and application of optogenetics. *Annual review of neuroscience* **34** (2011).

141. Lendvai, B., Stern, E. A., Chen, B. & Svoboda, K. Experience-dependent plasticity of dendritic spines in the developing rat barrel cortex in vivo. *Nature* **404,** 876 (2000).

142. De Paola, V. *et al.* Cell type-specific structural plasticity of axonal branches and boutons in the adult neocortex. *Neuron* **49,** 861–875 (2006).

143. Zito, K., Knott, G., Shepherd, G. M., Shenolikar, S. & Svoboda, K. Induction of spine growth and synapse formation by regulation of the spine actin cytoskeleton. *Neuron* **44,** 321–334 (2004).

144. Mizrahi, A. & Katz, L. C. Dendritic stability in the adult olfactory bulb. *Nature neuroscience* **6,** 1201 (2003).

145. Egger, V., Svoboda, K. & Mainen, Z. F. Dendrodendritic synaptic signals in olfactory bulb granule cells: local spine boost and global low-threshold spike. *Journal of Neuroscience* **25,** 3521–3530 (2005).

146. Nevian, T. & Sakmann, B. Single spine Ca2+ signals evoked by coincident EPSPs and backpropagating action potentials in spiny stellate cells of layer 4 in the juvenile rat somatosensory barrel cortex. *Journal of Neuroscience* **24,** 1689–1699 (2004).

147. Rozsa, B., Zelles, T., Vizi, E. S. & Lendvai, B. Distance-dependent scaling of calcium transients evoked by backpropagating spikes and synaptic activity in dendrites of hippocampal interneurons. *Journal of Neuroscience* **24,** 661–670 (2004).

148. Rusakov, D. A., Wuerz, A. & Kullmann, D. M. Heterogeneity and specificity of presynaptic Ca2+ current modulation by mGluRs at individual hippocampal synapses. *Cerebral Cortex* **14,** 748–758 (2004).

149. Yuste, R. & Denk, W. Dendritic spines as basic functional units of neuronal integration. *Nature* **375,** 682 (1995).

150. Chen, C.-C., Lu, J. & Zuo, Y. Spatiotemporal dynamics of dendritic spines in the living brain. *Frontiers in neuroanatomy* **8,** 28 (2014).